

1

<sup>2</sup>A SEARCH FOR LONG-LIVED, CHARGED, SUPERSYMMETRIC PARTICLES  
<sup>3</sup>USING IONIZATION WITH THE ATLAS DETECTOR

4

BRADLEY AXEN

5

September 2016 – Version 0.48

6



<sup>8</sup> Bradley Axen: *A Search for Long-Lived, Charged, Supersymmetric Particles using*  
<sup>9</sup> *Ionization with the ATLAS Detector*, Subtitle, © September 2016

<sup>10</sup>

Usually a quotation.

<sup>11</sup>

Dedicated to.



<sub>12</sub> ABSTRACT

---

<sub>13</sub> How to write a good abstract:

<sub>14</sub> <https://plg.uwaterloo.ca/~migod/research/beck00PSLA.html>



<sub>15</sub> PUBLICATIONS

---

<sub>16</sub> Some ideas and figures have appeared previously in the following publications:

<sub>17</sub>

<sub>18</sub> Put your publications from the thesis here. The packages `multibib` or `bibtopic`  
<sub>19</sub> etc. can be used to handle multiple different bibliographies in your document.



---

<sup>21</sup> ACKNOWLEDGEMENTS

<sup>22</sup> Put your acknowledgements here.

<sup>23</sup>

<sup>24</sup> And potentially a second round.

<sup>25</sup>



26 CONTENTS

---

27	I	INTRODUCTION	1
28	1	INTRODUCTION	3
29	II	THEORETICAL CONTEXT	5
30	2	STANDARD MODEL	7
31	2.1	Action and the Lagrangian . . . . .	7
32	2.2	Gauge Invariance and Forces . . . . .	8
33	2.2.1	$SU(2) \times U(1)$ and the Electroweak Force . . . . .	9
34	2.2.2	$SU(3)$ and the Strong Force . . . . .	10
35	2.3	Noether's Theorem, Charges, and Matter . . . . .	10
36	2.3.1	Quarks . . . . .	11
37	2.3.2	Leptons . . . . .	12
38	2.3.3	Chirality . . . . .	12
39	2.4	Higgs Mechanism and Mass . . . . .	12
40	2.5	Phenomenology . . . . .	12
41	3	SUPERSYMMETRY	13
42	3.1	Motivation . . . . .	13
43	3.2	Structure . . . . .	13
44	3.3	Phenomenology . . . . .	13
45	4	LONG-LIVED PARTICLES	15
46	4.1	Mechanisms . . . . .	15
47	4.1.1	Examples in Supersymmetry . . . . .	15
48	4.2	Phenomenology . . . . .	15
49	4.2.1	Disimilarities to Prompt Decays . . . . .	15
50	4.2.2	Characteristic Signatures . . . . .	15
51	III	EXPERIMENTAL STRUCTURE AND RECONSTRUCTION	17
52	5	THE LARGE HADRON COLLIDER	19
53	5.1	Injection Chain . . . . .	20
54	5.2	Design . . . . .	21
55	5.2.1	Layout . . . . .	21
56	5.2.2	Magnets . . . . .	22
57	5.2.3	RF Cavities . . . . .	23
58	5.2.4	Beam . . . . .	25
59	5.3	Luminosity Parameters . . . . .	25
60	5.4	Delivered Luminosity . . . . .	27
61	6	THE ATLAS DETECTOR	29
62	6.1	Coordinate System . . . . .	31
63	6.2	Magnetic Field . . . . .	32
64	6.3	Inner Detector . . . . .	34
65	6.3.1	Pixel Detector . . . . .	37

66	6.3.2	Semiconductor Tracker . . . . .	39
67	6.3.3	Transition Radiation Tracker . . . . .	41
68	6.4	Calorimetry . . . . .	42
69	6.4.1	Electromagnetic Calorimeter . . . . .	44
70	6.4.2	Hadronic Calorimeters . . . . .	45
71	6.5	Muon Spectrometer . . . . .	47
72	6.5.1	Monitored Drift Tube . . . . .	49
73	6.5.2	Resistive Plate Chamber . . . . .	50
74	6.5.3	Cathode Strip Chamber . . . . .	50
75	6.5.4	Thin Gap Chamber . . . . .	50
76	6.6	Trigger . . . . .	52
77	7	EVENT RECONSTRUCTION . . . . .	55
78	7.1	Tracks and Vertices . . . . .	55
79	7.1.1	Pixel Neural Network . . . . .	57
80	7.1.2	Pixel dE/dx . . . . .	58
81	7.1.3	Vertex Reconstruction . . . . .	58
82	7.2	Electrons and Photons . . . . .	59
83	7.2.1	Photon Identification . . . . .	60
84	7.2.2	Electron Identification . . . . .	60
85	7.3	Muons . . . . .	60
86	7.3.1	Muon Identification . . . . .	61
87	7.4	Jets . . . . .	61
88	7.4.1	Topological Clustering . . . . .	62
89	7.4.2	Jet Algorithms . . . . .	63
90	7.4.3	Jet Energy Scale . . . . .	64
91	7.5	Missing Transverse Energy . . . . .	64
92	IV	CALORIMETER RESPONSE . . . . .	67
93	8	RESPONSE MEASUREMENT WITH SINGLE HADRONS . . . . .	69
94	8.1	Dataset and Simulation . . . . .	70
95	8.1.1	Data Samples . . . . .	70
96	8.1.2	Simulated Samples . . . . .	70
97	8.1.3	Event Selection . . . . .	70
98	8.2	Inclusive Hadron Response . . . . .	71
99	8.2.1	E/p Distribution . . . . .	71
100	8.2.2	Zero Fraction . . . . .	72
101	8.2.3	Neutral Background Subtraction . . . . .	73
102	8.2.4	Corrected Response . . . . .	75
103	8.2.5	Additional Studies . . . . .	77
104	8.3	Identified Particle Response . . . . .	80
105	8.3.1	Decay Reconstruction . . . . .	80
106	8.3.2	Identified Response . . . . .	81
107	8.3.3	Additional Species in Simulation . . . . .	83
108	8.4	Summary . . . . .	84
109	9	JET ENERGY RESPONSE AND UNCERTAINTY . . . . .	87
110	9.1	Motivation . . . . .	87

111	9.2	Uncertainty Estimate . . . . .	87
112	9.3	Summary . . . . .	90
113	V	SEARCH FOR LONG-LIVED PARTICLES	93
114	10	LONG-LIVED PARTICLES IN ATLAS	95
115	10.1	Event Topology . . . . .	95
116	10.1.1	Detector Interactions . . . . .	96
117	10.1.2	Lifetime Dependence . . . . .	97
118	10.2	Simulation . . . . .	100
119	11	EVENT SELECTION	103
120	11.1	Trigger . . . . .	104
121	11.2	Kinematics and Isolation . . . . .	105
122	11.3	Particle Species Rejection . . . . .	109
123	11.4	Ionization . . . . .	112
124	11.4.1	Mass Estimation . . . . .	113
125	11.5	Efficiency . . . . .	114
126	12	BACKGROUND ESTIMATION	117
127	12.1	Background Sources . . . . .	117
128	12.2	Prediction Method . . . . .	118
129	12.3	Validation . . . . .	119
130	12.3.1	Closure in Simulation . . . . .	119
131	12.3.2	Validation Region in Data . . . . .	120
132	13	SYSTEMATIC UNCERTAINTIES AND RESULTS	123
133	13.1	Systematic Uncertainties . . . . .	123
134	13.1.1	Background Estimate . . . . .	123
135	13.1.2	Signal Yield . . . . .	124
136	13.2	Final Yields . . . . .	130
137	13.3	Cross Sectional Limits . . . . .	131
138	13.4	Mass Limits . . . . .	133
139	13.5	Context for Long-Lived Searches . . . . .	135
140	VI	CONCLUSIONS	139
141	14	SUMMARY AND OUTLOOK	141
142	14.1	Summary . . . . .	141
143	14.2	Outlook . . . . .	141
144	VII	APPENDIX	143
145	A	INELASTIC CROSS SECTION	145
146	B	EXPANDED R-HADRON YIELDS AND LIMITS	147
147		BIBLIOGRAPHY	153

148 LIST OF FIGURES

---

149	Figure 1	A Feynman diagram representing the interaction of the $A$ field with a generic fermion, $f$ . . . . .	9
150			
151	Figure 2	The interactions of the electroweak gauge bosons with generic fermions. . . . .	10
152			
153	Figure 3	The interaction of the strong gauge bosons, the gluons, with generic fermions. . . . .	10
154			
155	Figure 4	The particle content of the Standard Model ( <a href="#">SM</a> ). . . . .	11
156	Figure 5		
157			
158			
159			
160	Figure 6	The four collision points and corresponding experiments of the Large Hadron Collider ( <a href="#">LHC</a> ). The image includes the location of the nearby city of Geneva as well as the border of France and Switzerland. . . . .	20
161			
162			
163			
164			
165	Figure 7	The cumulative luminosity over time delivered to the A Toroidal LHC ApparatuS ( <a href="#">ATLAS</a> ) experiment from high energy proton-proton collisions since 2011. The energies of the collisions are listed for each of the data-taking periods. . . . .	21
166			
167			
168			
169	Figure 8	The accelerator complex that builds up to the full design energies at the <a href="#">LHC</a> . The protons are passed in order to Linac 2, the <a href="#">PSB</a> , the <a href="#">PS</a> , the <a href="#">SPS</a> and then the <a href="#">LHC</a> . . . . .	22
170			
171			
172			
173	Figure 9	A schematic of the layout of the <a href="#">LHC</a> , not to scale. The arched and straight sections are illustrated at the bottom of the schematic, and all four crossing sites are indicated with their respective experiments. . . . .	23
174			
175			
176			
177			
178			
179	Figure 10	A cross section of the the cryodipole magnets which bend the flight path of protons around the circumference of the <a href="#">LHC</a> . The diagram includes both the superconducting coils which produce the magnetic field and the structural elements which keep the magnets precisely aligned. . . . .	24
180			
181	Figure 11	The arrangement of four radiofrequency ( <a href="#">RF</a> ) cavities within a cryomodule. . . . .	24
182			
183			
184			
185	Figure 12	The cumulative luminosity versus time delivered to ATLAS (green), recorded by ATLAS (yellow), and certified to be good quality data (blue) during stable beams for pp collisions at 13 TeV in 2015. . . . .	27
186			
187			
188	Figure 13	The luminosity-weighted distribution of the mean number of interactions per crossing for the 2015 pp collision data at 13 TeV. . . . .	28
189			
		A cut-away schematic of the layout of the <a href="#">ATLAS</a> detector. Each of the major subsystems is indicated. . . .	30

190	<b>Figure 14</b>	A cross-sectional slice of the <b>ATLAS</b> experiment which illustrates how the various <b>SM</b> particles interact with the detector systems. . . . .	30
191			
192			
193	<b>Figure 15</b>	The layout of the four superconducting magnets in the <b>ATLAS</b> detector. . . . .	33
194			
195	<b>Figure 16</b>	The arrangement of the subdetectors of the <b>ATLAS</b> inner detector. Each of the subdetectors is labeled in the cut-away view of the system. . . . .	35
196			
197			
198	<b>Figure 17</b>	A quarter section of the <b>ATLAS</b> inner detector which shows the layout of each of the subdetectors in detail. The lower panel shows an enlarged view of the pixel detector. Example trajectories for a particle with $\eta = 1.0, 1.5, 2.0, 2.5$ are shown. The Insertible B-Layer ( <b>IBL</b> ), which was added after the original detector commissioning, is not shown. . . . .	35
199			
200			
201			
202			
203			
204			
205	<b>Figure 18</b>	A computer generated three-dimensional view of the inner detector along the line of the beam axis. The subdetectors and their positions are labeled. . . . .	36
206			
207			
208	<b>Figure 19</b>	An alternative computer generated three-dimensional view of the inner detector transverse to the beam axis. The subdetectors and their positions are labeled. . . . .	36
209			
210			
211	<b>Figure 20</b>	The integrated radiation lengths traversed by a straight track at the exit of the ID envelope, including the services and thermal enclosures. The distribution is shown as a function of $ \eta $ and averaged over $\phi$ . The breakdown indicates the contributions of individual subdetectors, including services in their active volume. . . . .	37
212			
213			
214			
215			
216			
217	<b>Figure 21</b>	· · · · · . . . . .	40
218	<b>Figure 22</b>	An image of the insertion of the <b>IBL</b> into the current pixel detector. . . . .	40
219			
220	<b>Figure 23</b>	A three-dimensional computer-generated image of the geometry of the <b>IBL</b> with a view (a) mostly transverse to the beam pipe (b) mostly parallel to the beam pipe. . . . .	41
221			
222			
223	<b>Figure 24</b>	An exploded view of the geometry of the silicon microstrip ( <b>SCT</b> ) double layers in the barrel region. . . . .	42
224			
225	<b>Figure 25</b>	· · · · · . . . . .	43
226	<b>Figure 26</b>	The depth of (a) the electromagnetic barrel calorimeter in radiation lengths and (b) all calorimeters in interaction lengths as a function of pseudorapidity. . . . .	44
227			
228			
229	<b>Figure 27</b>	A schematic of the Liquid Argon ( <b>LAr</b> ) calorimeter in the barrel region, highlighting the accordion structure. . . . .	44
230			
231	<b>Figure 28</b>	A schematic of a hadronic tile module which shows the alternating layers of steel and plastic scintillator. . . . .	46
232			
233	<b>Figure 29</b>	The segmentation in depth and $\eta$ of the tile-calorimeter modules in the central (left) and extended (right) barrels. . . . .	46
234			
235	<b>Figure 30</b>	A cut-away diagram of the muon systems on <b>ATLAS</b> . . . . .	47

236	Figure 31	A quarter view of the muon spectrometer which highlights the layout of each of the detecting elements. The BOL, BML, BIL, EOL, EML, and EIL are all Monitored Drift Tube ( <a href="#">MDT</a> ) elements, where the acronyms encode their positions. . . . .	48
237			
238			
239			
240			
241	Figure 32	A schematic of the cross-section of the muon spectrometer in the barrel region. . . . .	48
242			
243	Figure 33	A schematic of a single <a href="#">MDT</a> chamber, which shows the multilayers of drift tubes as well as the alignment system. . . . .	49
244			
245			
246	Figure 34	A schematic of the Cathode Strip Chamber ( <a href="#">CSC</a> ) endcap, showing the overlapping arrangement of the eight large and eight small chambers. . . . .	51
247			
248			
249	Figure 35	A schematic of the Thin Gap Chamber ( <a href="#">TGC</a> ) doublet and triplet layers. . . . .	51
250			
251	Figure 36	The L1 Trigger rate broken down into the types of triggers as a function of the luminosity block for the 2015 data collection period. . . . .	53
252			
253			
254	Figure 37	The HLT Trigger rate broken down into the types of triggers as a function of the luminosity block for the 2015 data collection period. . . . .	54
255			
256			
257	Figure 38	The $x$ and $y$ locations of the hits generated in a simulated $t\bar{t}$ event in the inner detector. The hits which belong to tracks formed using the inside-out algorithm are highlighted in red, while the hits which belong to tracks formed using the outside-in algorithm are circled in black. . . . .	56
258			
259			
260			
261			
262			
263	Figure 39	Examples of the clusters formed in a single layer of the pixel detector for (a) a single isolated particle, (b) two nearly-overlapping particles, and (c) a particle which emits a $\delta$ -ray [12]. . . . .	57
264			
265			
266			
267	Figure 40	The total, fractional jet energy scale ( <a href="#">JES</a> ) uncertainties estimated for 2015 data as a function of jet $p_T$ . . . . .	65
268			
269	Figure 41	An illustration (a) of the $E/p$ variable used throughout this paper. The red energy deposits come from the charged particle targeted for measurement, while the blue energy deposits are from nearby neutral particles and must be subtracted. The same diagram (b) for the neutral-background selection, described in Section 8.2.3. . . . .	72
270			
271			
272			
273			
274			
275	Figure 42	The $E/p$ distribution and ratio of simulation to data for isolated tracks with (a) $ \eta  < 0.6$ and $1.2 < p/\text{GeV} < 1.8$ and (b) $ \eta  < 0.6$ and $2.2 < p/\text{GeV} < 2.8$ . . . . .	72
276			
277			
278	Figure 43	The fraction of tracks as a function (a, b) of momentum, (c, d) of interaction lengths with $E \leq 0$ for tracks with positive (on the left) and negative (on the right) charge. . . . .	74
279			
280			
281			

282	Figure 44	$\langle E/p \rangle_{\text{BG}}$ as a function of the track momentum for tracks with (a) $ \eta  < 0.6$ , (b) $0.6 <  \eta  < 1.1$ , and as a function of the track pseudorapidity for tracks with (c) $1.2 < p/\text{GeV} < 1.8$ , (d) $1.8 < p/\text{GeV} < 2.2$ . . . . .	75
283			
284			
285			
286	Figure 45	$\langle E/p \rangle_{\text{COR}}$ as a function of track momentum, for tracks with (a) $ \eta  < 0.6$ , (b) $0.6 <  \eta  < 1.1$ , (c) $1.8 <  \eta  < 1.9$ , and (d) $1.9 <  \eta  < 2.3$ . . . . .	76
287			
288			
289	Figure 46	$\langle E/p \rangle_{\text{COR}}$ calculated using LCW-calibrated topological clusters as a function of track momentum for tracks with (a) zero or more associated topological clusters or (b) one or more associated topological clusters. . . . .	77
290			
291			
292			
293	Figure 47	Comparison of the $\langle E/p \rangle_{\text{COR}}$ for tracks with (a) less than and (b) greater than 20 hits in the TRT. . . . .	78
294			
295	Figure 48	Comparison of the $\langle E/p \rangle_{\text{COR}}$ for (a) positive and (b) negative tracks as a function of track momentum for tracks with $ \eta  < 0.6$ . . . . .	78
296			
297			
298	Figure 49	Comparison of the $E/p$ distributions for (a) positive and (b) negative tracks with $0.8 < p/\text{GeV} < 1.2$ and $ \eta  < 0.6$ , in simulation with the FTFP_BERT and QGSP_BERT physics lists. . . . .	79
299			
300			
301			
302	Figure 50	Comparison of the response of the hadronic calorimeter as a function of track momentum (a) at the EM-scale and (b) after the LCW calibration. . . . .	79
303			
304			
305	Figure 51	Comparison of the response of the EM calorimeter as a function of track momentum (a) at the EM-scale and (b) with the LCW calibration. . . . .	80
306			
307			
308	Figure 52	The reconstructed mass peaks of (a) $K_S^0$ , (b) $\Lambda$ , and (c) $\bar{\Lambda}$ candidates. . . . .	81
309			
310	Figure 53	The $E/p$ distribution for isolated (a) $\pi^+$ , (b) $\pi^-$ , (c) proton, and (d) anti-proton tracks. . . . .	82
311			
312	Figure 54	The fraction of tracks with $E \leq 0$ for identified (a) $\pi^+$ and $\pi^-$ , and (b) proton and anti-proton tracks . . . . .	82
313			
314	Figure 55	The difference in $\langle E/p \rangle$ between (a) $\pi^+$ and $\pi^-$ (b) $p$ and $\pi^+$ , and (c) $\bar{p}$ and $\pi^-$ . . . . .	83
315			
316	Figure 56	$\langle E/p \rangle_{\text{COR}}$ as a function of track momentum for (a) $\pi^+$ tracks and (b) $\pi^-$ tracks. . . . .	84
317			
318	Figure 57	The ratio of the calorimeter response to single particles of various species to the calorimeter response to $\pi^+$ with the physics list FTFP_BERT. . . . .	84
319			
320			
321	Figure 58	The spectra of true particles inside anti- $k_t$ , $R = 0.4$ jets with (a) $90 < p_T/\text{GeV} < 100$ , (b) $400 < p_T/\text{GeV} < 500$ , and (c) $1800 < p_T/\text{GeV} < 2300$ . . . . .	88
322			
323			
324	Figure 59	The JES uncertainty contributions, as well as the total JES uncertainty, as a function of jet $p_T$ for (a) $ \eta  < 0.6$ and (b) $0.6 <  \eta  < 1.1$ . . . . .	90
325			
326			

327	Figure 60	The JES correlations as a function of jet $p_T$ and $ \eta $ for jets in the central region of the detector. . . . .	91
328			
329	Figure 61	A schematic diagram of an R-Hadron event with a lifetime around 0.01 ns. The diagram includes one charged R-Hadron (solid blue), one neutral R-Hadron (dashed blue), Lightest Supersymmetric Particles ( <b>LSPs</b> ) (dashed green) and charged hadrons (solid orange). The pixel detector, calorimeters, and muon system are illustrated but not to scale. . . . .	97
330			
331			
332			
333			
334			
335			
336	Figure 62	A schematic diagram of an R-Hadron event with a lifetime around 4 ns. The diagram includes one charged R-Hadron (solid blue), one neutral R-Hadron (dashed blue), <b>LSPs</b> (dashed green) and a charged hadron (solid orange). The pixel detector, calorimeters, and muon system are illustrated but not to scale. . . . .	98
337			
338			
339			
340			
341			
342	Figure 63	A schematic diagram of an R-Hadron event with a lifetime around 5 ns. The diagram includes one charged R-Hadron (solid blue), one neutral R-Hadron (dashed blue), <b>LSPs</b> (dashed green) and charged hadrons (solid orange). The pixel detector, calorimeters, and muon system are illustrated but not to scale. . . . .	99
343			
344			
345			
346			
347			
348	Figure 64	A schematic diagram of an R-Hadron event with a lifetime around 20 ns. The diagram includes one charged R-Hadron (solid blue), one neutral R-Hadron (dashed blue), <b>LSPs</b> (dashed green) and charged hadrons (solid orange). The pixel detector, calorimeters, and muon system are illustrated but not to scale. . . . .	99
349			
350			
351			
352			
353			
354	Figure 65	A schematic diagram of an R-Hadron event with a lifetime around 20 ns. The diagram includes one charged R-Hadron (solid blue) and one neutral R-Hadron (dashed blue). The pixel detector, calorimeters, and muon system are illustrated but not to scale. . . . .	100
355			
356			
357			
358			
359	Figure 66	The distribution of (a) $E_T^{\text{miss}}$ and (b) Calorimeter $E_T^{\text{miss}}$ for simulated signal events before the trigger requirement. . . . .	104
360			
361			
362	Figure 67	The distribution of $E_T^{\text{miss}}$ for data and simulated signal events, after the trigger requirement. . . . .	106
363			
364	Figure 68	The trigger efficiency for the HLT_xe70 trigger requirement as a function of (a) $E_T^{\text{miss}}$ and (b) Calorimeter $E_T^{\text{miss}}$ for simulated signal events. . . . .	107
365			
366			
367	Figure 69	The dependence of $dE/dx$ on $N_{\text{split}}$ in data after basic track hit requirements have been applied. . . . .	108
368			
369	Figure 70	The distribution of $dE/dx$ with various selections applied in data and simulated signal events. . . . .	108
370			

371	Figure 71	The distribution of track momentum for data and simulated signal events, after previous selection requirements have been applied. . . . .	109
372			
373			
374	Figure 72	The distribution of $M_T$ for data and simulated signal events, after previous selection requirements have been applied. . . . .	110
375			
376			
377	Figure 73	The distribution of summed tracked momentum within a cone of $\Delta R < 0.25$ around the candidate track for data and simulated signal events, after previous selection requirements have been applied. . . . .	111
378			
379			
380			
381	Figure 74	The normalized, two-dimensional distribution of $E/p$ and $f_{EM}$ for simulated (a) $Z \rightarrow ee$ , (b) $Z \rightarrow \tau\tau$ , (c) 1200 GeV Stable R-Hadron events, and (d) 1200 GeV, 10 ns R-Hadron events. . . . .	112
382			
383			
384			
385	Figure 75	Two-dimensional distribution of $dE/dx$ versus charge signed momentum ( $qp$ ) for minimum-bias tracks. The fitted distributions of the most probable values for pions, kaons and protons are superimposed. . . . .	113
386			
387			
388			
389	Figure 76	The distribution of mass estimated using $dE/dx$ for simulated stable R-Hadrons with masses between 1000 and 1600 GeV. . . . .	114
390			
391			
392	Figure 77	The acceptance $\times$ efficiency as a function of R-Hadron (a) mass and (b) lifetime. (a) shows all of the combinations of mass and lifetime considered in this search, and (b) highlights the lifetime dependence for 1000 GeV and 1600 GeV R-Hadrons. . . . .	116
393			
394			
395			
396			
397	Figure 78	The distribution of (a) $dE/dx$ and (b) momentum for tracks in data and simulated signal after requiring the event level selection and the track selection on $p_T$ , hits, and $N_{\text{split}}$ . Each sub-figure shows the normalized distributions for tracks classified as hadrons, electrons, and muons in data and R-Hadrons in the simulated signal. . . . .	118
398			
399			
400			
401			
402			
403			
404	Figure 79	The distribution of $M_{dE/dx}$ (a) before and (b) after the ionization requirement for tracks in simulated W boson decays and for the randomly generated background estimate. . . . .	120
405			
406			
407			
408	Figure 80	The distribution of $M_{dE/dx}$ (a) before and (b) after the ionization requirement for tracks in the validation region and for the randomly generated background estimate. . . . .	121
409			
410			
411			
412	Figure 81	The trigger efficiency for the HLT_xe70 trigger requirement as a function of Calorimeter $E_T^{\text{miss}}$ for simulated data events with a W boson selection. Simulated signal events and simulated W boson events are also included. . . . .	126
413			
414			
415			
416			

417	Figure 82	The efficiency of the muon veto for $R$ -hadrons of two different masses, as a function of $\frac{1}{\beta}$ for simulated R-Hadron tracks. . . . .	128
418			
419			
420	Figure 83	The average reconstructed MDT $\beta$ distribution for $Z \rightarrow \mu\mu$ events in which one of the muons is reconstructed as a slow muon, for both data and simulation. A gaussian fit is superimposed. . . . .	129
421			
422			
423			
424	Figure 84	The observed mass distribution of events in data and the generated background distribution in (a) the stable and (b) the metastable signal region. A few example simulated signal distributions are superimposed. . . . .	130
425			
426			
427			
428	Figure 85	The observed and expected cross section limits as a function of mass for the stable simulated signal. The predicted cross section values for the corresponding signals are included. . . . .	133
429			
430			
431			
432	Figure 86	The observed and expected cross section limits as a function of mass for each generated lifetime. The predicted cross section values for the corresponding signals are included. . . . .	134
433			
434			
435			
436	Figure 87	The excluded range of masses as a function of gluino lifetime. The expected lower limit (LL), with its experimental $\pm 1\sigma$ band, is given with respect to the nominal theoretical cross-section. The observed 95% LL obtained at $\sqrt{s} = 8$ TeV [68] is also shown for comparison.	136
437			
438			
439			
440			
441	Figure 88	The constraints on the gluino mass as a function of lifetime for a split-supersymmetry model with the gluino R-Hadrons decaying into a gluon or light quarks and a neutralino with mass of 100 GeV. The solid lines indicate the observed limits, while the dashed lines indicate the expected limits. The area below the curves is excluded. The dots represent results for which the particle is assumed to be prompt or stable. . . . .	137
442			
443			
444			
445			
446			
447			
448			

449 LIST OF TABLES

---

450 <b>Table 1</b>	The design parameters of the <a href="#">LHC</a> beam that determines the energy of collisions and the luminosity, for both the injection of protons and at the nominal circulation. . . . .	26
451		
452		
453		
454 <b>Table 2</b>	The performance goals for each of the subsystems of the <a href="#">ATLAS</a> detector. The $ \eta $ coverage specifies the range where the subsystem needs to be able to provide measurements with the specified resolution. The resolutions include a $p_T$ or E dependence that is added in quadrature with a $p_T/E$ independent piece. . . . .	31
455		
456		
457		
458		
459		
460 <b>Table 3</b>	A summary of the parameters of each of the three magnet systems on <a href="#">ATLAS</a> . . . . .	33
461		
462 <b>Table 4</b>	A summary of the parameters of the inner detector and each of the subdetectors [3]. . . . .	38
463		
464 <b>Table 5</b>	A summary of the expected performance of the combined inner detector [8]. Included are the reconstruction efficiencies for multiple particle types as well as the momentum and impact parameter ( <a href="#">IP</a> ) resolution for various momenta. . . . .	39
465		
466		
467		
468		
469 <b>Table 6</b>	The trigger menu for the 2015 data collection with $L = 5 \times 10^{33} \text{ cm}^{-2} \text{ s}^{-1}$ . Both the L1 and high level trigger ( <a href="#">HLT</a> ) selection requirements and their trigger rates are shown measured at the specified luminosity are shown. The typical offline selections represent a typical set of offline requirements imposed after the trigger in an analysis. . . . .	53
470		
471		
472		
473		
474		
475		
476 <b>Table 7</b>	The dominant sources of corrections and systematic uncertainties in the <a href="#">JES</a> estimation technique, including typical values for the correcting shift ( $\Delta$ ) and the associated uncertainty ( $\sigma$ ). . . . .	89
477		
478		
479		
480 <b>Table 8</b>	The expected number of events at each level of the selection for metastable 1600 GeV, 10 ns R-Hadrons, along with the number of events observed in data, for $3.2 \text{ fb}^{-1}$ . The simulated yields are shown with statistical uncertainties only. The total efficiency $\times$ acceptance is also shown for the signal. . . . .	115
481		
482		
483		
484		
485		
486 <b>Table 9</b>	A summary of the sources of systematic uncertainty for the data-driven background in the signal region. If the uncertainty depends on the mass, the maximum values are reported. . . . .	123
487		
488		
489		

490	Table 10	A summary of the sources of systematic uncertainty for the simulated signal yield. The uncertainty depends on the mass and lifetime, and the maximum negative and positive values are reported in the table. . . . .	125
491			
492			
493			
494	Table 11	Example of the contributing systematic variations to the total systematic for the $E_T^{\text{miss}}$ Scale, as measured in a 1200 GeV, Stable R-Hadron signal sample. . . . .	127
495			
496			
497	Table 12	The estimated number of background events and the number of observed events in data for the specified selection regions prior to the requirement on mass. The background estimates show statistical and systematic uncertainties. . . . .	130
498			
499			
500			
501			
502	Table 13	The left and right extremum of the mass window for each generated mass point with a 10 ns lifetime. . . . .	131
503			
504	Table 14	The left and right extremum of the mass window used for each generated stable mass point. . . . .	131
505			
506	Table 15	The expected number of signal events, the expected number of background events, and the observed number of events in data with their respective statistical errors within the respective mass window for each generated stable mass point. . . . .	132
507			
508			
509			
510			
511	Table 16	The expected number of signal events, the expected number of background events, and the observed number of events in data with their respective statistical errors within the respective mass window for each generated mass point with a lifetime of 10 ns. . . . .	132
512			
513			
514			
515			
516	Table 17	The observed and expected 95% CL lower limit on mass for gluino R-Hadrons for each considered lifetime. . . . .	135
517			
518	Table 18	The left and right extremum of the mass window for each generated mass point with a 50 ns lifetime. . . . .	147
519			
520	Table 19	The left and right extremum of the mass window for each generated mass point with a 30 ns lifetime. . . . .	147
521			
522	Table 20	The left and right extremum of the mass window for each generated mass point with a 10 ns lifetime. . . . .	148
523			
524	Table 21	The left and right extremum of the mass window used for each generated mass point with a lifetime of 3 ns. . . . .	148
525			
526	Table 22	The left and right extremum of the mass window used for each mass point with a lifetime of 1 ns. . . . .	148
527			
528	Table 23	The left and right extremum of the mass window for each generated mass point with a lifetime of 0.4 ns. . . . .	149
529			
530	Table 24	The left and right extremum of the mass window used for each generated stable mass point. . . . .	149
531			

532	Table 25	The expected number of signal events, the expected number of background events, and the observed number of events in data with their respective statistical errors within the respective mass window for each generated mass point with a lifetime of 50 ns. . . . .	149
533			
534			
535			
536			
537	Table 26	The expected number of signal events, the expected number of background events, and the observed number of events in data with their respective statistical errors within the respective mass window for each generated mass point with a lifetime of 30 ns. . . . .	150
538			
539			
540			
541			
542	Table 27	The expected number of signal events, the expected number of background events, and the observed number of events in data with their respective statistical errors within the respective mass window for each generated mass point with a lifetime of 10 ns. . . . .	150
543			
544			
545			
546			
547	Table 28	The expected number of signal events, the expected number of background events, and the observed number of events in data with their respective statistical errors within the respective mass window for each generated mass point with a lifetime of 3 ns. . . . .	151
548			
549			
550			
551			
552	Table 29	The expected number of signal events, the expected number of background events, and the observed number of events in data with their respective statistical errors within the respective mass window for each generated mass point with a lifetime of 1 ns. . . . .	151
553			
554			
555			
556			
557	Table 30	The expected number of signal events, the expected number of background events, and the observed number of events in data with their respective statistical errors within the respective mass window for each generated mass point with a lifetime of p4 ns. . . . .	152
558			
559			
560			
561			
562	Table 31	The expected number of signal events, the expected number of background events, and the observed number of events in data with their respective statistical errors within the respective mass window for each generated stable mass point . . . . .	152
563			
564			
565			
566			

567 LISTINGS

---

568 ACRONYMS

---

- 569 SM Standard Model  
570 CERN European Organization for Nuclear Research  
571 SUSY Supersymmetry  
572 LSP Lightest Supersymmetric Particle  
573 LHC Large Hadron Collider  
574 ATLAS A Toroidal LHC ApparatuS  
575 CMS Compact Muon Solenoid  
576 ALICE A Large Ion Collider Experiment  
577 LHCb Large Hadron Collider beauty experiment  
578 LEP the Large Electron Positron collider  
579 PS Proton Synchrotron  
580 PSB Proton Synchrotron Booster  
581 SPS Super Proton Synchrotron  
582 SCT silicon microstrip  
583 TRT transition radiation tracker  
584 LAr Liquid Argon  
585 EM electromagnetic  
586 RPC Resistive Plate Chamber  
587 TGC Thin Gap Chamber  
588 MDT Monitored Drift Tube  
589 CSC Cathode Strip Chamber  
590 ToT time over threshold  
591 RoI Region of Interest  
592 LCW local cluster weighted  
593 MIP minimally ionizing particle  
594 IP impact parameter

- 595 EPJC European Physical Journal C  
596 JES jet energy scale  
597 LLP Long-Lived Particle  
598 CR Control Region  
599 NLO next-to-leading order  
600 NLL next-to-leading logarithmic  
601 PDF parton distribution function  
602 ISR initial state radiation  
603 RMS root mean square  
604 IBL Insertible B-Layer  
605 CP Combined Performance  
606 MDT Monitored Drift Tube  
607 RF radiofrequency  
608 HLT high level trigger  
609 QCD quantum chromodynamics

610

## PART I

611

### INTRODUCTION

612

You can put some informational part preamble text here.



# 1

613

## 614 INTRODUCTION

---



615

## PART II

616

### THEORETICAL CONTEXT

617

You can put some informational part preamble text here.



# 2

618

619 STANDARD MODEL

---

620 21 ACTION AND THE LAGRANGIAN

Originally, both action and the Lagrangian were constructed for an integral reformulation of the laws of classical mechanics, which is a purely mathematical step: any differential equation can be re-expressed in terms of an integral equation. The Lagrangian,  $\mathcal{L}$ , is classically given by the difference of kinetic energy and potential energy. The Lagrangian is defined this way so that the action,  $\mathcal{S}$ , given by

$$\mathcal{S}[\mathbf{q}(t)] = \int_{t_1}^{t_2} \mathcal{L}(\mathbf{q}, \dot{\mathbf{q}}, t) dt \quad (1)$$

621 returns the classical equations of motion when one requires it to be stationary  
622 in the path,  $\mathbf{q}(t)$ . This formulation of classical mechanics is extremely useful in  
623 calculations, and generalizes beautifully to cover all types of physics.

624 In particular, with the development of quantum mechanics in the twentieth  
625 century, the concepts of action and the Lagrangian were found to generalize to  
626 more complicated physics for which the classical laws do not hold. Quantum  
627 mechanics and quantum field theory can be constructed from the action, using  
628 the path integral formulation, by assuming that a particle undergoes all possible  
629 paths  $\mathbf{q}(t)$  with an imaginary phase given by  $e^{i\mathcal{S}[\mathbf{q}(t)]/\hbar}$ . This reduces to classical  
630 mechanics in the limit as  $\hbar$  goes to zero, as all paths for which the action is not  
631 stationary interfere with each other so as to cancel their contributions. Because  
632 the wavefunction of a particle can be completely determined through the action  
633 and the action depends only on the Lagrangian, the Lagrangian itself is sufficient  
634 to describe the physics governing the particle.

635 So, in both classical and quantum mechanics, the Lagrangian of a system con-  
636 tains everything there is to know about the system, apart from initial conditions.  
637 Thus, the most natural way to express that a system has a certain symmetry is to  
638 require that the Lagrangian is invariant under a corresponding symmetry trans-  
639 formation. This makes the Lagrangian the central piece of the discussion of  
640 gauge invariance; the mathematical representation of gauge invariance is that a  
641 gauge transformation on the appropriate components of the Lagrangian returns  
642 an identical Lagrangian. That is,

$$\mathcal{L}(\psi, D^\mu) = \mathcal{L}(U\psi, D'^\mu) \quad (2)$$

643 where  $\psi$  is the wavefunction and  $D^\mu$  is the covariant derivative, both of which  
644 transform under a symmetry operation. There are a number of immediate and  
645 surprisingly powerful consequences of requiring that the Lagrangian is invariant  
646 under a symmetry operation.

## 647 2.2 GAUGE INVARIANCE AND FORCES

648 The simplest possible Lagrangian is the free Dirac Lagrangian, which describes  
 649 a relativistic fermion in a vacuum.

$$\mathcal{L} = i\bar{\psi}\not{d}\psi - m\bar{\psi}\psi \quad (3)$$

650 A fermion denotes a particle with spin-1/2, and the kinematic term in the La-  
 651 grangian correctly describes the free propagation of a fermionic particle with  
 652 mass  $m$ . This equation is clearly invariant under a global  $U(1)$  transformation,  
 653 that is changing  $\psi$  by a complex phase has no effect. The derivative operator  
 654 commutes with a constant phase factor, and wherever  $\psi$  appears it's complex  
 655 conjugate also appears so as to cancel out the change of phase. However, the La-  
 656 grangian as written is not invariant under the local  $U(1)$  symmetry postulated  
 657 for the [SM](#), which can be written as  $U = e^{i\alpha(x)}$ . The piece of the Lagrangian  
 658 involving a derivative will return an extra term that will break the invariance of  
 659 the Lagrangian under this transformation:

$$\begin{aligned} \mathcal{L}' &= i(\bar{\psi}U^\dagger)\not{d}(U\psi) - m(\psi U^\dagger)(U\psi) \\ &= i(\bar{\psi}U^\dagger)U(\not{d} - \gamma^\mu \partial_\mu \alpha(x))\psi - m(\psi U^\dagger)(U\psi) \\ &= i\bar{\psi}\not{d}\psi - m\bar{\psi}\psi - i\gamma^\mu \partial_\mu \alpha(x)\bar{\psi}\psi \\ &= \mathcal{L} - i\gamma^\mu \partial_\mu \alpha(x)\bar{\psi}\psi \\ &\neq \mathcal{L} \end{aligned}$$

660 So, in order to enforce the required symmetry, the typical approach is to con-  
 661 struct a covariant derivative, that is to add a term to the derivative operator so  
 662 that the unwanted term in  $\mathcal{L}'$  is exactly cancelled. A generic form for such a  
 663 derivative is given by

$$D^\mu = \partial^\mu - iqA^\mu$$

664 where at this point  $A^\mu$  is an arbitrary field that transforms under the  $U(1)$  op-  
 665 erator and  $q$  is a scaling factor. Adding this component to the above Lagrangian  
 666 gives

$$\mathcal{L}' = i(\bar{\psi}U^\dagger)U(\not{d} - \gamma^\mu \partial_\mu \alpha(x) - iq\gamma^\mu A'_\mu)\psi - m(\psi U^\dagger)(U\psi) \quad (4)$$

$$\mathcal{L}' = \mathcal{L} + \gamma^\mu (-i\partial_\mu \alpha(x) - iqA'_\mu + iqA_\mu)\bar{\psi}\psi \quad (5)$$

667 and because the transformation of  $A^\mu$  is unspecified, we will have that  $\mathcal{L} = \mathcal{L}'$   
 668 whenever

$$A'_\mu = A_\mu - \frac{1}{q}\partial_\mu \alpha(x)$$

Figure 1: A Feynman diagraming representing the interaction of the  $A$  field with a generic fermion,  $f$ .

669 The above procedure demonstrated that beginning with the Lagrangian for  
 670 a free fermion and imposing a local  $U(1)$  symmetry required the existence of  
 671 a vector field  $A^\mu$ , and specified it's transformation under the  $U(1)$  gauge group.  
 672 The additional term in the derivative can expanded to form a completely separate  
 673 term in the Lagrangian,

$$\mathcal{L} = i\bar{\psi}\not{d}\psi - m\bar{\psi}\psi - (q\bar{\psi}\gamma^\mu\psi)A^\mu \quad (6)$$

674 and in this form it is clear that the  $A^\mu$  term has the exact form of the electromagnetic  
 675 interaction. That is, this is the Lagrangian which reproduces the relativistic  
 676 form of Maxwell's equations for a particle interacting with an electromagnetic  
 677 field. It is natural to also introduce a term to the Lagrangian at this point to  
 678 describe the free propagation of the vector  $A$  field, where the propagation of a  
 679 vector field has the form of

$$-\frac{1}{16\pi}F^{\mu\nu}F_{\mu\nu} \quad \text{with} \quad F_{\mu\nu} = \partial_\mu A_\nu - \partial_\nu A_\mu \quad (7)$$

680 which then also describes the electromagnetic interactions in a vacuum and the  
 681 propagation of a photon. The photon is an example of a gauge boson, a spin-0  
 682 particle required to exist by a gauge symmetry of the Lagrangian and one that  
 683 corresponds to a force. In summary, requiring the  $U(1)$  symmetry was enough  
 684 to recover all of electromagnetism and to predict the existence of a photon in the  
 685 **SM**.

686 The interaction term that was placed into the Lagrangian by this procedure  
 687 can be conveniently summarized with Feynman diagrams, which diagramatically  
 688 represent a transition from an initial state to a final state. All diagrams  
 689 that start with the same initial state and end with the same final state must be  
 690 considered, but more complicated diagrams can be built by linking together the  
 691 simplest versions. A diagram that corresponds to the above term,  $(q\bar{\psi}\gamma^\mu\psi)A^\mu$ ,  
 692 is shown in Figure 1, for an interaction with a generic fermion.

### 693 2.2.1 $SU(2) \times U(1)$ AND THE ELECTROWEAK FORCE

694 The full picture of the electroweak section of the **SM** is more complicated than the  
 695 simplified explanation of the electromagnetic piece described above. In practice,  
 696 it is necessary to consider the entire  $SU(2) \times U(1)$  symmetry together, but the  
 697 procedure is the same. Enforcing the symmetry on the Lagrangian requires the  
 698 introduction of a covariant derivative, this time with four total distinct terms,  
 699 one for each of the generators of  $SU(2) \times U(1)$ . The result is a series of terms  
 700 in the Lagrangian which describe the interaction of a fermion with four vector  
 701 fields, the  $W_1$ ,  $W_2$ ,  $W_3$ , and  $B$  fields. These fields can mix in the quantum sense,

Figure 2: The interactions of the electroweak gauge bosons with generic fermions.

Figure 3: The interaction of the strong gauge bosons, the gluons, with generic fermions.

702 and linear combinations form the  $W^+$ ,  $W^-$ ,  $Z$ , and  $A$  fields that are considered  
 703 actual particles in the [SM](#)<sup>1</sup>. The interactions between these fields and fermions  
 704 are summarized in Figure 2.

705 2.2.2  $SU(3)$  AND THE STRONG FORCE

706 The same procedure can be applied starting with the  $SU(3)$  symmetry require-  
 707 ment, where eight additional fields must be introduced, one for each of the gen-  
 708 erators of  $SU(3)$ . The resulting Lagrangian describes quantum chromodynam-  
 709 ics ([QCD](#)) and predicts the existence of eight gauge bosons known collectively as  
 710 gluons. The interactions between these fields and fermions are summarized in  
 711 Figure 3.

712 23 NOETHER'S THEOREM, CHARGES, AND MATTER

713 Another direct consequence of the symmetries stipulated in the [SM](#) are a series  
 714 of conserved quantities, Noether charges, named after the mathematician and  
 715 physicist Emmy Noether. The charges arise as a direct consequence of Noether's  
 716 theorem, which can be informally stated as

717       *For every symmetry of the Lagrangian, there exists a corresponding phys-  
 718       ical quantity whose value is conserved in time.*

719 Or, stated another way, symmetries of the Lagrangian mathematically require  
 720 the conservation of specific quantities taken from the Lagrangian. This rela-  
 721 tionship can also be thought of as operating in the other direction, the exis-  
 722 tence of a conserved charge can be shown to generate the symmetry in the La-  
 723 grangian. This theorem is actually quite striking in a somewhat unexpected re-  
 724 lation between simple geometric symmetries and physically observable conser-  
 725 vation laws. For example, the theorem connects the translation invariance of  
 726 the Lagrangian in space to the conservation of momentum and the translation  
 727 invariance in time to the conservation of energy.

728       **Quick derivation of conservation of charge here.**

729 In the context of the [SM](#), the required symmetries of  $U(1) \times SU(2) \times SU(3)$   
 730 correspond to the charges that are considered properties of all elementary par-  
 731 ticles. The most familiar of these properties is the electric charge,  $Q$ , which is  
 732 one of the conserved quantities of  $SU(2) \times U(1)$ . The remaining pieces of  
 733  $SU(2) \times U(1)$  correspond to weak isospin,  $T$  and  $T_3$ , where  $T$  has only non-  
 734 negative values and  $T_3$  can be positive and negative. The  $SU(3)$  symmetry is

---

1 These states are the actual particles because they are mass eigenstates, but the full explanation of this will have to wait for the discussion of the Higgs mechanism.

generated by the three colors of QCD, red, green, and blue, each with a corresponding opposite color, anti-red, anti-green, and anti-blue.

The matter in the observable universe consists of a collection of particles which carry these charges, in addition to spin and mass. The particles typically thought of as matter are all fermions: particles with spin-1/2. All of the fermions belong to one of two groups, quarks and leptons, and one of three generations. Each of the generations have similar properties but significantly different masses; the particles in consecutive generations have increasing mass. Quarks are distinguished from leptons in that they carry color charge, in addition to electric charge and weak isospin. The particles in the SM are summarized in Figure 4, and the matter particles are the twelve types of fermions displayed on the left side of the graphic.

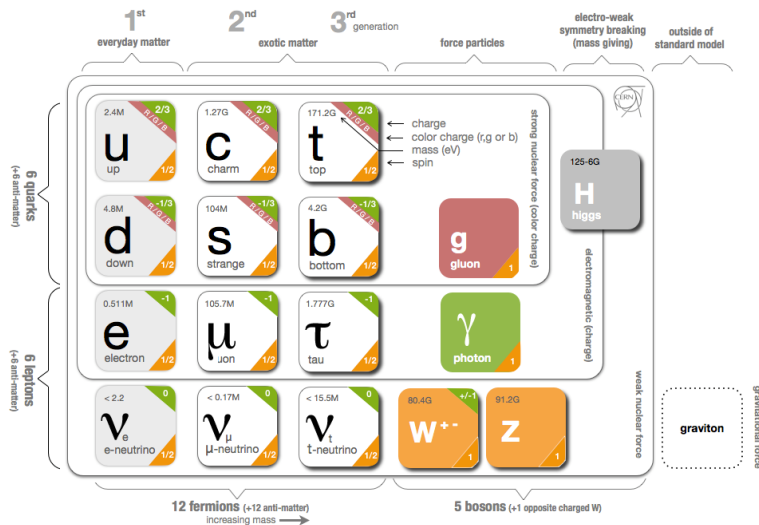


Figure 4: The particle content of the SM.

### 2.3.1 QUARKS

The three generations of quarks each have a particle with electric charge +2/3 and one with charge -1/3. They are referred to as up and down, charm and strange, and top and bottom respectively, and these are referred to as the quark flavors. Although Figure 4 only shows these six flavors, there is a unique particle for each combination of the three colors and flavor. And each quark has an anti-particle with the opposite electric and color charge values.

However, individual quarks are never observed in nature, but instead form color-neutral bound states. One way to form a color neutral combination is a bound state of three quarks with three different color charges, called a baryon. Baryons are the most common type of quark configuration in conventional matter, and include protons and neutrons. The other common configuration is a bound state of a quark and an anti-quark, called a meson, where the two quarks

760 have the same type but opposite colors. The conservation of the various charges  
 761 carried by quarks, along with the requirement that quarks appear in color-neutral  
 762 states, result in the observed conservation of baryon number,  $B$ , where baryons  
 763 have  $B = 1$  and mesons have  $B = 0$ .

764 2.3.2 LEPTONS

765 The remaining fermions, the leptons, do not carry color charge. Each generation  
 766 contains an electrically charged lepton, the electron, muon, and tau, and an elec-  
 767 trically neutral lepton called a neutrino. For the charged leptons, the flavors are  
 768 mass eigenstates, with the masses listed in Figure 4. The flavors of the neutrinos,  
 769 on the other hand, are not mass eigenstates: they propagate in mass eigenstates  
 770 and so can oscillate between different flavors. The absolute masses of the neu-  
 771 trinos are not currently known, but the phenomenon of oscillations shows that  
 772 they have three different mass values. Although there is no direct conservation  
 773 law resulting from the symmetries of the SM Lagrangian, no interactions have  
 774 been observe which alter lepton number,  $L$ , the difference in the number of lep-  
 775 tons and anti-leptons.

776 2.3.3 CHIRALITY

777 All of the fermions described above have two possible values of the magnitude  
 778 of weak isospin,  $T$ , either 0 or  $1/2$ . The fermions with  $T = 0$  are called right-  
 779 handed, while those with  $T = 1/2$  are called left-handed. For left-handed fermions,  
 780 each of the quark and lepton generations have one particle with  $T_3 = -1/2$  and  
 781 one with  $T_3 = +1/2$ . The neutrinos have  $T_3 = +1/2$ , while the charged leptons  
 782 have  $T_3 = -1/2$ . Similarly, the positively charged quarks have  $T_3 = +1/2$  and the  
 783 negatively charged quarks have  $T_3 = -1/2$ . Because the right-handed neutrinos  
 784 would have no charge of any type, it is not clear if they exist at all.

785 2.4 HIGGS MECHANISM AND MASS

786 2.5 PHENOMENOLOGY

# 3

787

788 SUPERSYMMETRY

---

789 3.1 MOTIVATION

790 3.2 STRUCTURE

791 3.3 PHENOMENOLOGY



# 4

792

793 LONG-LIVED PARTICLES

---

794 4.1 MECHANISMS

795 4.1.1 EXAMPLES IN SUPERSYMMETRY

796 4.2 PHENOMENOLOGY

797 4.2.1 DISIMILARITIES TO PROMPT DECAYS

798 4.2.2 CHARACTERISTIC SIGNATURES



799

### PART III

800

## EXPERIMENTAL STRUCTURE AND RECONSTRUCTION

801

You can put some informational part preamble text here.



802

803 THE LARGE HADRON COLLIDER

---

804 The LHC, a two-ring superconducting hadron accelerator, provides high energy  
805 proton-proton collisions for several large experiments at European Organization  
806 for Nuclear Research (CERN) in Geneva, Switzerland [1, 2]. It is the largest,  
807 highest-luminosity, and highest-energy proton collider ever built, and was con-  
808 structed by a collaboration of more than 10,000 scientists from the more than  
809 100 countries that contribute to CERN. The original design of the LHC focused on  
810 providing collision energies of up to 14 TeV and generating enough collisions to  
811 reveal physics beyond the SM which is predicted to exist at higher energy scales.

812 The LHC was installed in an existing 27 km tunnel at CERN which was origi-  
813 nally designed to house the Large Electron Positron collider (LEP). This allows  
814 the collider to use existing accelerators at the same complex to provide the initial  
815 acceleration of protons up to 450 GeV before injecting into LHC. The injected  
816 hadrons are accelerated up to as much as 14 TeV while being focused into two  
817 beams traveling in opposite directions. During this process the protons circulate  
818 around the tunnel millions of times, while the beams are intermittently crossed  
819 at the four locations of the experiments to provide collisions. These collision  
820 points correspond to the four major LHC experiments: ATLAS, Compact Muon  
821 Solenoid (CMS), Large Hadron Collider beauty experiment (LHCb), and A Large  
822 Ion Collider Experiment (ALICE), and Figure 5 shows the layout of the exper-  
823 iments both on the surface and below. ATLAS and CMS are both general pur-  
824 pose, high-luminosity detectors which search for a wide range of new types of  
825 physics [3, 4]. LHCb studies the interactions of b-hadrons to explore the asymme-  
826 try between matter and antimatter [5]. ALICE focuses on the collisions of lead  
827 ions, which the LHC also provides, in order to study the properties of quark-  
828 gluon plasma [6].

829 During the first five years of operation, after the LHC turned on in 2010, the  
830 LHC has provided four major data collecting periods. In 2010 the LHC generated  
831 collisions at several energies, starting at 900 GeV. It increased the energy from  
832 900 GeV to 2.76 TeV and then subsequently to 7 TeV, with a peak luminos-  
833 ity of  $2 \times 10^{32} \text{ cm}^{-2}\text{s}^{-1}$ , and a total delivered luminosity of  $50 \text{ pb}^{-1}$ . The next  
834 run, during 2011, continued the operation at 7 TeV and provided an additional  $5$   
835  $\text{fb}^{-1}$  with a peak luminosity of  $4 \times 10^{33} \text{ cm}^{-2}\text{s}^{-1}$ . The energy was then increased  
836 to 8 TeV for the data collection during 2012, which provided  $23 \text{ fb}^{-1}$  with a peak  
837 luminosity of  $7.7 \times 10^{33} \text{ cm}^{-2}\text{s}^{-1}$ . After the first long shutdown for 2013 and  
838 2014, the LHC resumed operation and increased the energy to 13 TeV in 2015,  
839 where it delivered  $4.2 \text{ fb}^{-1}$  with a peak luminosity of  $5.5 \times 10^{33} \text{ cm}^{-2}\text{s}^{-1}$ . The  
840 LHC is currently providing additional 13 TeV collisions in 2016 with higher lu-  
841 minosities than during any previous data collection periods. These running peri-  
842 ods are summarized in Figure 6, which shows the total delivered luminosity over

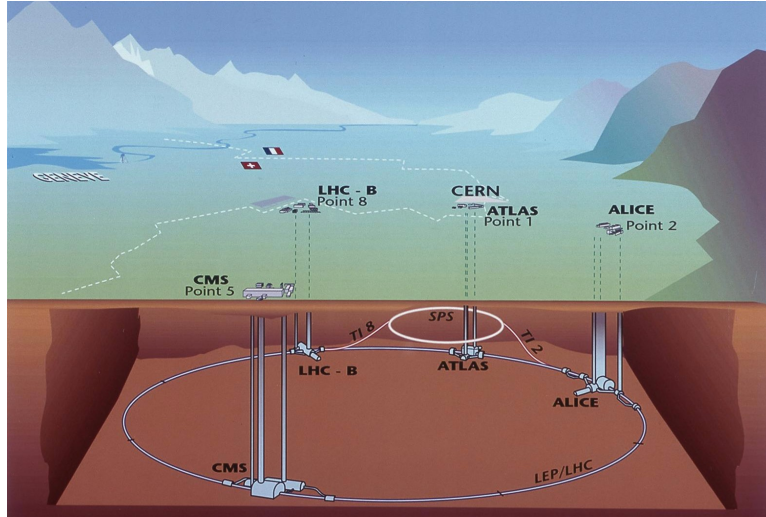


Figure 5: The four collision points and corresponding experiments of the [LHC](#). The image includes the location of the nearby city of Geneva as well as the border of France and Switzerland.

843 time for the [ATLAS](#) experiment during each of the four years of data collection  
 844 since 2011.

## 845 5.1 INJECTION CHAIN

846 The [LHC](#) takes advantage of the presence of previously built accelerators at [CERN](#)  
 847 to work up to the target energy in consecutive stages. The series of accelerators  
 848 that feed into the [LHC](#) are known collectively as the injection chain, and together  
 849 with the [LHC](#) form the accelerator complex. The full complex is illustrated in  
 850 Figure 7, which details the complex series required to reach collisions of 13 or  
 851 14 TeV.

852 Protons at the [LHC](#) begin as hydrogen atoms in the Linac 2, a linear accelerator  
 853 which replaced Linac 1 as the primary proton accelerator at CERN in 1978. In  
 854 Linac 2, the hydrogen atoms are stripped of their electrons by a strong magnetic  
 855 field, and the resulting protons are accelerated up to 50 MeV by cylindrical con-  
 856 ductors charged by radio frequency cavities. The protons are then transferred  
 857 to the Proton Synchrotron Booster ([PSB](#)), which uses a stack of four synchrotron  
 858 rings to accelerate the protons up to 1.4 GeV. Then the protons are injected  
 859 into the Proton Synchrotron ([PS](#)) which again uses synchrotron rings to bring  
 860 the energy up to 25 GeV. The intermediate step between Linac 2 and the [PS](#) is  
 861 not directly necessary, as the [PS](#) can accelerate protons starting from as low as  
 862 50 MeV. The inclusion of the [PSB](#) allows the [PS](#) to accept a higher intensity of  
 863 injection and so increases the deliverable luminosity in the [LHC](#). The penulti-  
 864 mate stage of acceleration is provided by the Super Proton Synchrotron ([SPS](#)), a  
 865 large synchrotron with a 7 km circumference that was commissioned at CERN  
 866 in 1976. During this step the protons increase in energy to 450 GeV, after which  
 867 they can be directly injected into the [LHC](#).

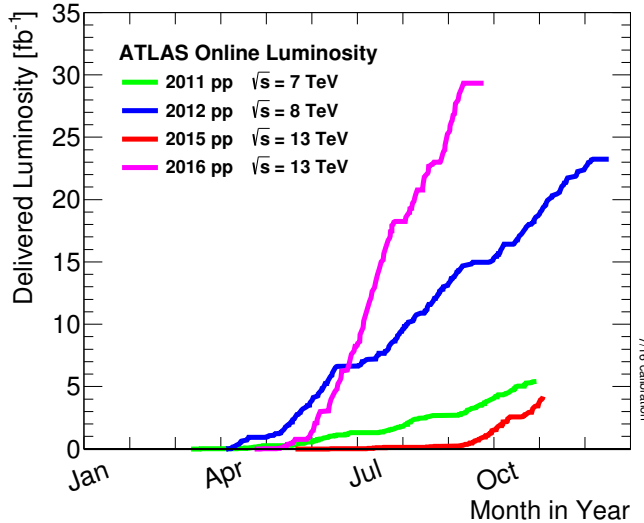


Figure 6: The cumulative luminosity over time delivered to the ATLAS experiment from high energy proton-proton collisions since 2011. The energies of the collisions are listed for each of the data-taking periods.

The final step is the LHC itself, which receives protons from the SPS into two separate beam pipes which circulate in opposite directions. The filling process at this steps takes approximately 4 minutes, and the subsequent acceleration to the final energy (6.5 TeV during 2015 and up to 7 TeV by design) takes approximately half an hour. At this point the protons circulate around the circumference tens of thousands of times a second and continue for up to two hours.

## 5.2 DESIGN

### 5.2.1 LAYOUT

Many of the aspects of the LHC design are driven by the use of the existing LEP tunnel. This tunnel slopes gradually, with a 1.4% decline, with 90% of its length built into molasse rock which is particularly well suited to the application. The circumference is composed of eight 2987 meter arcs and eight 528 meter straight sections which connect them; this configuration is illustrated in Figure 8. The tunnel diameter is 3.7 m throughout its length.

The design energy is directly limited by the size of this tunnel, with its radius of curvature of 2804 m. A significant magnetic field is required to curve the protons around that radius of curvature; the relationship is given by

$$p \simeq 0.3BR \quad (8)$$

where  $p$  is the momentum of the particle in GeV,  $B$  is the magnetic field in Tesla, and  $R$  is the radius of curvature in meters. From the target design energy of 14 TeV, or 7 TeV of momentum for protons in each beam, the required magnetic field is 8.33 Tesla. This is too large a field strength to be practical with

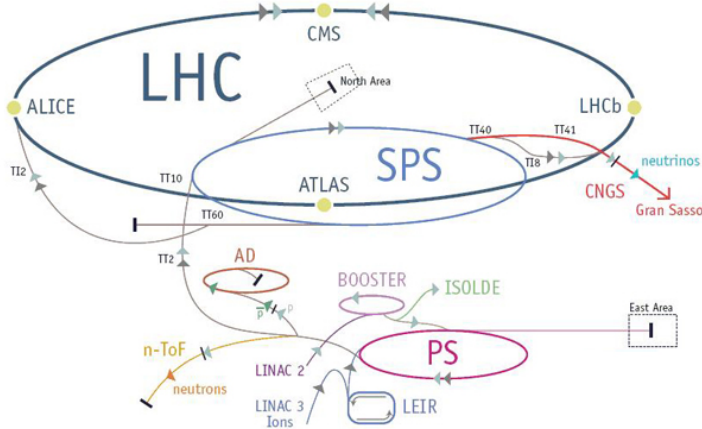


Figure 7: The accelerator complex that builds up to the full design energies at the LHC. The protons are passed in order to Linac 2, the PSB, the PS, the SPS and then the LHC.

iron electromagnets, because of the enormous power required and the resulting requirements for cooling. Because of these constraints, the LHC uses superconducting magnets which can maintain that field strength with significantly less power consumption.

### 5.2.2 MAGNETS

Specifically the magnets chosen were Niobium and Titanium (NbTi) which allow for field strengths as high as 10 Tesla when cooled down to 1.9 K. Reaching the target temperature of 1.9 K for all of the magnets requires superfluid helium and a large cryogenic system along the entire length of the tunnel. During normal operation, the LHC uses 120 tonnes of helium within the magnets, and the entire system is cooled by eight cryogenic helium refrigerators. The temperature increase that occurs during transit from the refrigerator along the beam necessitates that the refrigerators cool the helium down to 1.8 K. Any significant increase above this temperature range can remove the superconductive properties of the magnets, which in turn generates drastically larger heat losses from the current within the magnets and causes a rapid rise in temperature called a quench.

In all there are approximately 8000 superconducting magnets distributed around the LHC. The 1232 bending magnets, which keep the protons curving along the length of the beam, are twin bore cryodipoles, which allow both proton beams to be accommodated by one magnet and all of the associated cooling structure. Figure 9 shows the cross section of the design for these dipoles. The magnets are very large, 16.5 m long with a diameter of 0.57 meters and a total weight of 28 tonnes. They are slightly curved, with an angle of 5.1 mrad, in order to carefully match the beam path. The twin bore accommodates both magnets inside the two 5 cm diameter holes which are surrounded by the superconducting coils. The coils require 12 kA of current in order to produce the required magnetic

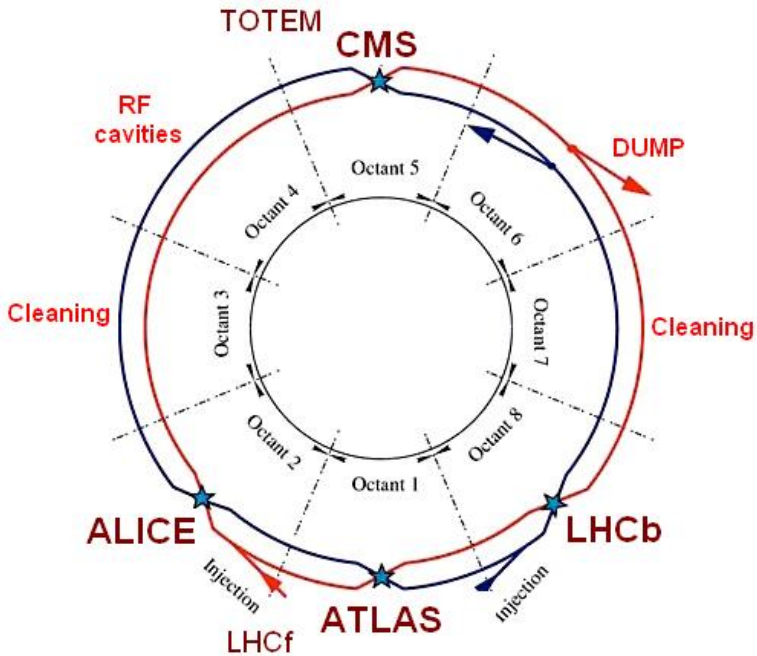


Figure 8: A schematic of the layout of the LHC, not to scale. The arched and straight sections are illustrated at the bottom of the schematic, and all four crossing sites are indicated with their respective experiments.

field. These coils are comprised of NbTi cable wound in two layers; the wire in the inner layer has a diameter of 1.065 mm while the wire in the outer layer has a diameter of 0.825 mm.

The large currents in the wires, along with the magnetic field produced, result in forces on the magnets which would tend to push them apart with over 10,000 Newtons per meter. Constraining the magnets requires a significant amount of structure including non-magnetic stainless steel collars. Both the presence of these electromagnetic forces and the varying thermal contraction coefficient of the pieces of the magnet produce significant forces on the cold mass structure. The cold mass is carefully engineered to so that these stresses do not significantly alter the magnetic field shape, which must be maintained between magnets to a precision of approximately  $10^{-4}$  for successful operation.

The remaining 6800 magnets are a variety of quadrupole, sextapole, octopole, and single bore dipole magnets. These are used to damp oscillations, correct beam trajectories, focus the beams during circulation, and to squeeze the beams before collisions.

### 5.2.3 RF CAVITIES

Sixteen RF cavities produce the actual acceleration of the proton beam up to the design energy. These RF cavities are tuned to operate at 400 MHz, and are powered by high-powered electron beams modulated at the same frequency, called klystrons. The resonance within the cavity with the oscillating electric field establishes a voltage differential of 2 MV per cavity. The sixteen cavities are

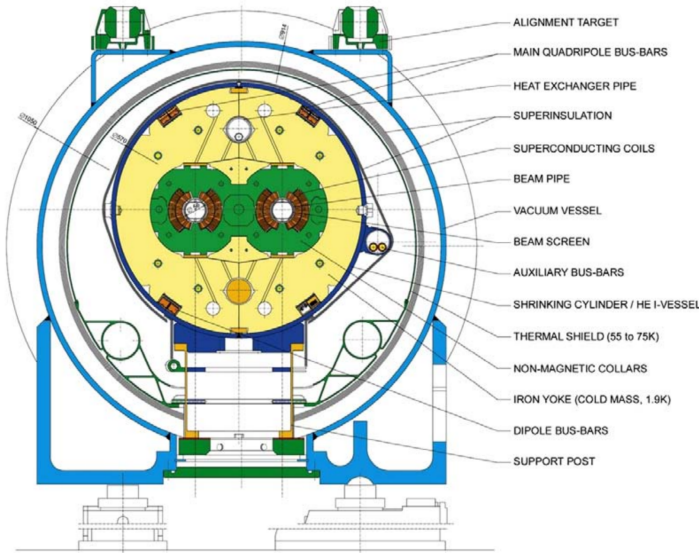


Figure 9: A cross section of the the cryodipole magnets which bend the flight path of protons around the circumference of the LHC. The diagram includes both the superconducting coils which produce the magnetic field and the structural elements which keep the magnets precisely aligned.

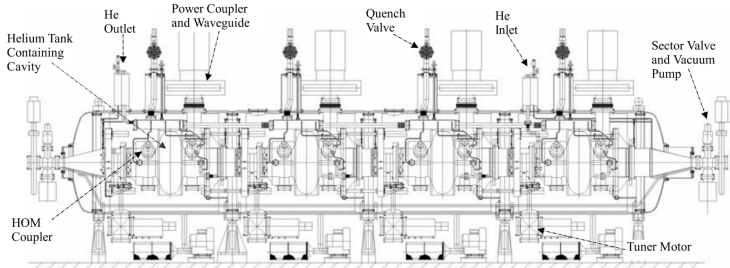


Figure 10: The arrangement of four RF cavities within a cryomodule.

938 split between the two beams, so combined the cavities provide 16 MV per beam,  
 939 which accelerate the protons on each consecutive pass through the cavity. This  
 940 acceleration is also necessary during circulation even after the target energy has  
 941 been reach in order to compensate for losses from synchrotron radiation.

942 The cavities are arranged in cryomodules which contain four cavities, with  
 943 two cryomodules per beam; this arrangement is illustrated in Figure 10. These  
 944 cryomodules are necessary to maintain the superconducting state of the cavities,  
 945 which are also constructed from niobium. The RF cavities use niobium along  
 946 with copper to allow for low power losses in the superconductors. The copper  
 947 provides a reduced susceptibility to quenching, as it rapidly conducts away heat  
 948 generated by imperfections in the niobium, as well as natural shielding from the  
 949 earth's magnetic field which can interfere with the RF system.

950 The nature of the radio frequency oscillations tends to group protons together  
 951 into buckets. A proton traveling exactly in phase with the RF oscillations will not  
 952 be displaced at all during a single circulation, and those slightly ahead or behind

953 of that phase will slightly decelerate or accelerate, respectively. This produces  
 954 separate clusters of protons which arrive in phase to the cavities every 2.5 ns,  
 955 corresponding to the 400 MHz frequency.

956 5.2.4 BEAM

957 The beams of protons circulate within 54 km of 5 cm diameter beam pipe. This  
 958 entire structure is kept under vacuum at 1.9 K to prevent interactions between  
 959 the beam pipe and the magnets as well as to prevent any interactions between the  
 960 circulating protons and gas in the pipe. The vacuum within the pipe establishes  
 961 a pressure as low as  $10^{-9}$  mbar before the protons are introduced.

962 Because of the very high energies of the circulating protons, synchrotron ra-  
 963 diation is not negligible in the bending regions. The protons are expected to  
 964 radiate 3.9 kW per beam at 14 TeV, with 0.22 W/m, which is enough power to  
 965 heat the liquid helium and cause a quench were it absorbed by the magnets. To  
 966 prevent this, a copper screen is placed within the vacuum tube that absorb the  
 967 emitted photons. This screen is kept between 5 and 20 K by the liquid helium  
 968 cooling system.

969 5.3 LUMINOSITY PARAMETERS

970 In addition to the high energy of the collisions, the rate of collisions is extremely  
 971 important to enabling the discovery of new physics. Many measurements and  
 972 searches require a large number of events in order to be able to make statistically  
 973 significant conclusions. The rate of collisions is measured using luminosity, the  
 974 number of collisions per unit time and unit cross section for the proton-proton  
 975 collisions. From the beam parameters, luminosity is given by

$$\mathcal{L} = \frac{N_b^2 n_b f_{rev} \gamma}{4\pi \epsilon_n \beta^*} F \quad (9)$$

976 where  $N_b$  is the number of protons per bunch,  $n_b$  is the number of bunches per  
 977 beam,  $f_{rev}$  is the frequency of revolution,  $\gamma$  is the Lorentz factor for the protons  
 978 at the circulating energy,  $\epsilon_n$  is the emittance,  $\beta^*$  is the amplitude function at the  
 979 collision point, and  $F$  is a geometric factor that accounts for the crossing angle of  
 980 the beams at the collision point. The emittance measures the average spread of  
 981 particles in both position and momentum space, while the amplitude function  
 982 is a beam parameter which measures how much the beam has been squeezed.  
 983 Together  $\epsilon_n$  and  $\beta^*$  give the size of the beam in the transverse direction,  $\sigma = \sqrt{\epsilon \beta^*}$ .  $\beta$   
 984 changes over the length of the beam as the accessory magnets shape the  
 985 distribution of protons, but only the value at the point of collisions,  $\beta^*$ , affects  
 986 the luminosity.

987 The luminosity is maximized to the extent possible by tuning the parameters  
 988 in Equation 9. A number of these are constrained by the design decisions. The  
 989 revolution frequency is determined entirely by the length of the tunnel, as the

Parameter	Unit	Injection	Nominal
Beam Energy	TeV	0.450	7
Peak Instantaneous Luminosity	$\text{cm}^{-2}\text{s}^{-1}$	-	$10^{34}$
Bunch Spacing	ns	25	25
Number of Filled Bunches	-	2808	2808
Normalized Transverse Emittance	$\mu\text{m}$	3.75	3.75
Frequency	MHz	400.789	400.790
RF Voltage/Beam	MV	8	16
Stored Energy	MJ	-	362
Magnetic Field	T	0.54	8.33
Operating Temperature	K	1.9	1.9

Table 1: The design parameters of the [LHC](#) beam that determines the energy of collisions and the luminosity, for both the injection of protons and at the nominal circulation.

990 protons travel at very close to the speed of light. The geometric factor  $F$  is de-  
 991 termined by the crossing angle of the beams at the collision points, again a com-  
 992 ponent of the tunnel design; this angle is already very small at  $285 \mu\text{rad}$ , which  
 993 helps to maximize the geometric factor.

994 The major pieces that can be adjusted are the number of protons per bunch,  
 995  $N_b$ , the number of bunches in the beam,  $n_b$ , and the amplitude function  $\beta$ . In-  
 996 creasing either  $N_b$  or  $n_b$  increases the amount of energy stored in the beam,  
 997 which presents a danger if control of the beam is lost. At design specifications,  
 998 the beam stores 362 MJ, which is enough energy to damage the detectors or ac-  
 999 celerator if the beam were to wander out of the beam pipe. So, the luminosity  
 1000 is primarily controlled at the [LHC](#) by adjusting  $\beta^*$ , where lowering  $\beta^*$  increases  
 1001 the luminosity.  $\beta^*$  is tuned to provide the various values of luminosity used at  
 1002 the [LHC](#) which can be raised to as much as  $10^{34}$ .

1003 The nominal bunch structure consists of 3654 bunches, each holding  $10^{11}$  pro-  
 1004 tons, which cross a collision point in 25 ns. These are further subdivided into the  
 1005 buckets mentioned in Section 5.2.3 by the clustering properties of the [RF](#) cavities.  
 1006 The bunches are further grouped into trains of 72 bunches which are separated  
 1007 by a gap which would otherwise hold 12 bunches. At nominal operation 2808  
 1008 of the bunches will actually be filled with protons, while the remainder are left  
 1009 empty to form an abort gap that can be used in case the beam needs to be dumped.

1010 The various beam parameters are summarized in Table 1 for the designed op-  
 1011 eration. In practice the beam has operated at lower energies and lower luminosi-  
 1012 ties than the design values, but the [LHC](#) is expected to operate at the full design  
 1013 values during Run 2.

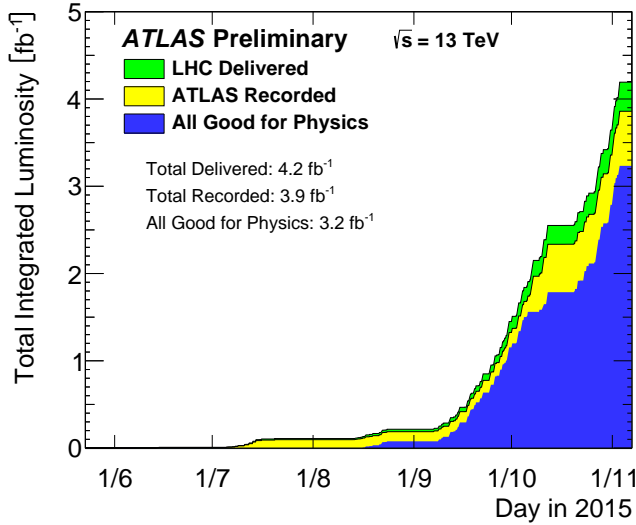


Figure 11: The cumulative luminosity versus time delivered to ATLAS (green), recorded by ATLAS (yellow), and certified to be good quality data (blue) during stable beams for pp collisions at 13 TeV in 2015.

## 5.4 DELIVERED LUMINOSITY

During the data collection of 2015, the LHC operated at luminosities as large as  $5 \times 10^{33}$ . It is convenient to refer to the integrated luminosity, the integral of the instantaneous luminosity, which corresponds directly to the number of delivered events for a given process.

$$N = \sigma \times \int \mathcal{L}(t) dt$$

where  $\sigma$  is the cross section for the process of interest. The integrated luminosity over time is shown in Figure 11. This includes the luminosity delivered by the LHC as well as the luminosity that was recorded by ATLAS. Some of the delivered luminosity is not recorded because ATLAS is placed in standby until the LHC reports that the beam conditions are stable, and only then does ATLAS begin recording. The figure also includes the amount of luminosity marked as good for physics, which includes additional requirements on the operation of the detector during data collection that are necessary for precise measurements.

In addition to the instantaneous luminosity, the beam conditions also influence the number of collisions that occur within a single bunch crossing. The multiple interactions at each crossing are referred to as pileup, often denoted  $\mu$ , and each of these interactions are present in a single measured event. Figure 12 shows the luminosity-weighted distribution of the mean number of interactions for events collected in 2015. The presence of as many as 20 events in a single collision provides a significant challenge in reconstructing events and isolating the targeted physical processes.

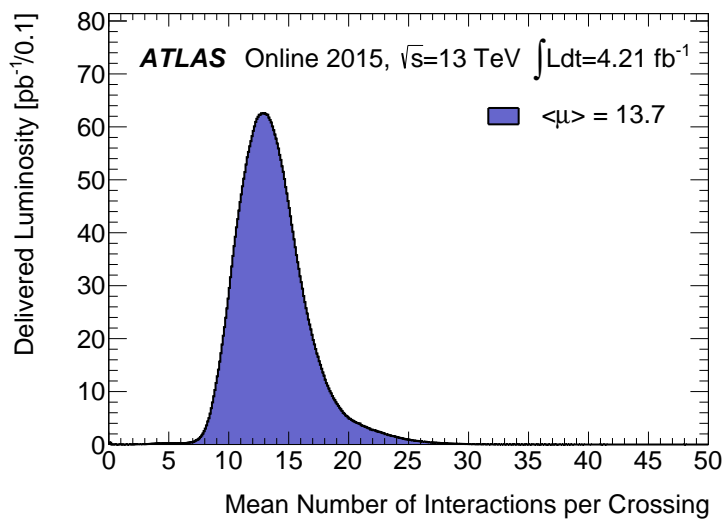


Figure 12: The luminosity-weighted distribution of the mean number of interactions per crossing for the 2015 pp collision data at 13 TeV.

1031

1032 THE ATLAS DETECTOR

---

1033 The four major LHC experiments at CERN seek to use the never before matched  
1034 energies and luminosities of the new collider to explore the boundaries of par-  
1035 ticle physics and to gain insight into the fundamental forces of nature. Two of  
1036 these experiments, ATLAS and CMS, are general purpose detectors that seek to  
1037 measure a variety of processes in the up to 14 TeV proton-proton collisions that  
1038 occur as much as 40 million times per second at the LHC at the design luminosity  
1039 of  $10^{34} \text{ cm}^{-2}\text{s}^{-1}$ . ATLAS employs a hermetic detector design, one which encloses  
1040 the particle collisions as completely as possible with detecting elements, that al-  
1041 lows it to study a wide range of physics from SM and Higgs measurements to  
1042 searches for new physics in models like Supersymmetry [3].

1043 Accommodating this wide variety of goals is a challenge for the design of  
1044 the detector. The wide range of energies involved requires high measurement  
1045 precision over several orders of magnitude and the ability to measure a vari-  
1046 ety of particle types. At the time of the construction of ATLAS, the Higgs bo-  
1047 son had yet to be discovered, but the diphoton decay mode was (correctly) ex-  
1048 pected to be important and necessitated a high resolution photon measurement.  
1049 The potential for decays of new heavy gauge bosons,  $W'$  and  $Z'$ , required a simi-  
1050 larly high momentum resolution for leptons with momentum up to several TeV.  
1051 Hadronic decay modes of several possible new high energy particles could re-  
1052 sult in very energetic jets, again up to several TeV, and reconstructing the decay  
1053 resonances would again require good energy resolution. Several models, such  
1054 as Supersymmetry (SUSY) or Extra Dimensions, predict the existence of particles  
1055 which would not interact with traditional detecting elements. However these  
1056 particles can still be observed in a hermetic detector by accurately measuring  
1057 the remaining event constituents to observe an imbalance in energy called miss-  
1058 ing energy or  $E_T^{\text{miss}}$ . Measuring  $E_T^{\text{miss}}$  implicitly requires a good resolution on all  
1059 SM particles that can be produced. And at the lower end of the energy spectrum,  
1060 precision SM measurements would require good resolution of a variety of parti-  
1061 cle types at energies as low as a few GeV, so the design needs to accommodate  
1062 roughly three orders of magnitude.

1063 This broad spectrum of measurements requires a variety of detector systems  
1064 working together to form a cohesive picture of each collision. Two large magnet  
1065 systems provide magnetic fields that provide a curvature to the propagation of  
1066 charged particles and allows for precision momentum measurements by other  
1067 systems. The inner detector uses a combination of tracking technologies to re-  
1068 construct particle trajectories and vertices for charged particles. A variety of  
1069 calorimeters measure the energies of hadrons, electrons, and photons over a  
1070 large solid angle. A large muon spectrometer identifies muons and uses the sec-  
1071 ond magnet system to provide an independent measurement of their momentum

1072 from the inner detector and improve the resolution. The layout of all of these  
 1073 systems is shown in Figure 13.

1074 The performance goals needed to achieve the various targeted measurements  
 1075 and searches discussed above can be summarized as resolution and coverage re-  
 1076 quirements on each of these systems. Those requirements are listed in Table 2.

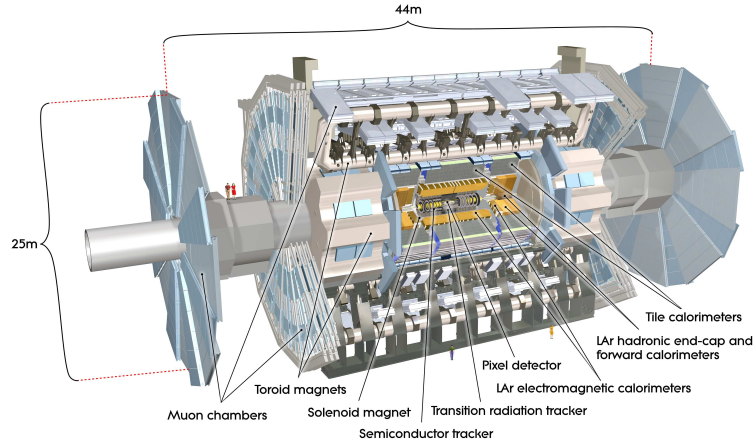


Figure 13: A cut-away schematic of the layout of the [ATLAS](#) detector. Each of the major subsystems is indicated.

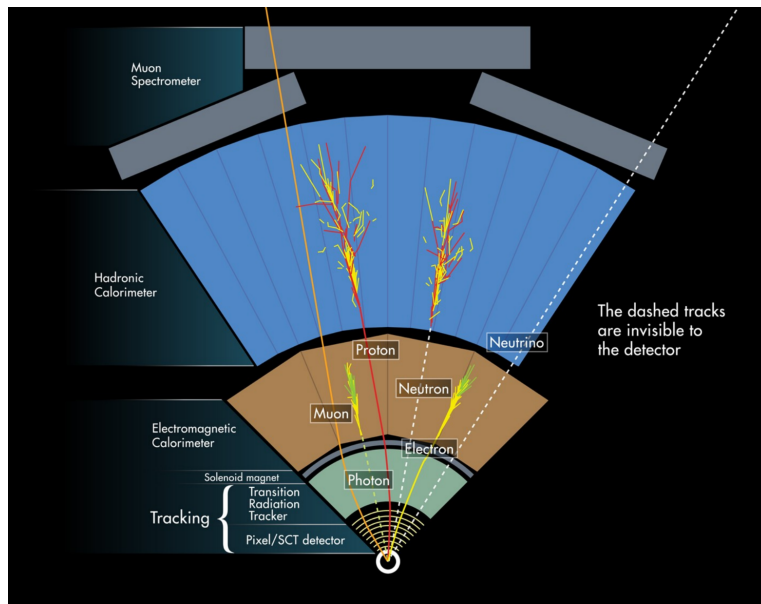


Figure 14: A cross-sectional slice of the [ATLAS](#) experiment which illustrates how the various SM particles interact with the detector systems.

1077 Incorporating these various pieces into a single detector is a significant tech-  
 1078 nical challenge. The resulting detector has a diameter of 22 m, is 46 m long,  
 1079 and weighs 7,000 tons; it is the largest volume particle detector ever constructed.  
 1080 The various detector elements need to be constructed and assembled with pre-  
 1081 cision as low as micrometers. These systems all need to function well even after  
 1082 exposure to the significant radiation dose from the collisions. Designing, con-

Detector Component	Required Resolution	$ \eta $ Coverage	
		Measurement	Trigger
Tracking	$\sigma_{p_T}/p_T = 0.05\% p_T + 1\%$	2.5	-
EM Calorimetry	$\sigma_E/E = 10\%/\sqrt{E} + 0.7\%$	3.2	2.5
Hadronic Calorimetry			
Barrel and Endcap	$\sigma_E/E = 50\%/\sqrt{E} + 3\%$	3.2	3.2
Forward	$\sigma_E/E = 100\%/\sqrt{E} + 10\%$	3.1 – 4.9	3.1 – 4.9
Muon Spectrometer	$\sigma_{p_T}/p_T = 10\% \text{ at } p_T = 1 \text{ TeV}$	2.7	2.4

Table 2: The performance goals for each of the subsystems of the [ATLAS](#) detector. The  $|\eta|$  coverage specifies the range where the subsystem needs to be able to provide measurements with the specified resolution. The resolutions include a  $p_T$  or E dependence that is added in quadrature with a  $p_T/E$  independent piece.

1083 structing, and installing the detector took the combined effort of more than 3000  
 1084 scientists from 38 countries over almost two decades.

## 1085 6.1 COORDINATE SYSTEM

1086 The coordinate system defined for the [ATLAS](#) detector is used throughout all of  
 1087 the sections of this thesis. The choice of coordinate system reflects the cylindri-  
 1088 cal symmetry of the [ATLAS](#) detector, and is oriented by the direction of the  
 1089 beamline which defines the  $z$ -direction. The positive  $z$  side of the detector is  
 1090 commonly referred to as the  $A$ -side, and the negative  $z$  side is referred to as  
 1091 the  $C$ -side. The  $x - y$  plane is then the plane transverse to the beam direction,  
 1092 with the  $x$  direction defined as pointing from the interaction point to the center  
 1093 of the [LHC](#) ring and the  $y$  direction defined as pointing upwards. The nominal  
 1094 interaction point is the origin of this system.

1095 It is more convenient in practice to use a cylindrical coordinate system. The  
 1096 angle from the  $z$ -axis is  $\theta$ . The azimuthal angle uses the usual definition, with  $\phi$   
 1097 running around the  $z$ -axis and  $\phi = 0$  corresponding to the  $x$ -axis. Many aspects  
 1098 of the detector are independent of the this coordinate to first order. The re-  
 1099 maining direction is typically specified using rapidity or pseudorapidity, where  
 1100 rapidity is defined as

$$y = \frac{1}{2} \ln \frac{E + p_z}{E - p_z} \quad (10)$$

1101 Rapidity is particularly useful to indicate the component along the  $z$  direction  
 1102 because differences in rapidity are invariant to boosts along the  $z$ -direction. A  
 1103 similar quantity which depends only the  $\theta$  is pseudorapidity,

$$\eta = -\ln \tan \frac{\theta}{2} \quad (11)$$

1104 which is the same as rapidity when the particle is massless and in the limit where  
 1105 the energy is much larger than the particle's mass. It is often useful to refer to  
 1106 differences in solid angle using the pseudorapidity and the azimuthal angle:

$$\Delta R = \sqrt{\Delta\phi^2 + \Delta\eta^2} \quad (12)$$

1107 The pseudorapidity is also invariant to boosts along the  $z$ -axis for high mo-  
 1108 mentum particles, and is preferable to rapidity because it does not depend on  
 1109 the specific choice of particle. Pseudorapidity is also preferable to  $\theta$  because  
 1110 of the aforementioned boost-invariance and also because particle production is  
 1111 roughly uniform in equal-width intervals of  $\eta$  up to about  $\eta = 5.0$ . A particle  
 1112 traveling along the beampipe has  $\eta = \text{inf}$  and a particle traveling perpendicular  
 1113 to the beampipe has  $\eta = 0$ . The extent of the tracker,  $|\eta| < 2.5$ , corresponds  
 1114 to approximately  $0.05\pi < \theta[\text{rad}] < 0.95\pi$  and the extent of the calorimeters,  
 1115  $|\eta| < 4.9$  corresponds to approximately  $0.005\pi < \theta[\text{rad}] < 0.995\pi$ . Many de-  
 1116 tector components are broken into multiple subsystems to provide coverage at  
 1117 greater  $|\eta|$ . The lower  $|\eta|$  region is referred to as the barrel, typically with  $|\eta| \lesssim 2$ ,  
 1118 and the greater  $|\eta|$  region is often referred to as the endcap.

1119 The initial energy and momentum of a proton-proton collision along the  $z$  di-  
 1120 rection is unknown in hadron colliders because different energies and momenta  
 1121 can be carried by the partons. Along the transverse plane, however, the vector  
 1122 sum of momentum will be zero. For this reason, many physical quantities are  
 1123 quantified in terms of their projection onto the transverse plan, such as  $p_T$  or  
 1124  $E_T$ . In addition,  $p_T$  alone determines the amount of curvature in the magnetic  
 1125 field, and can be measured independently by measuring the curvature of a parti-  
 1126 cle's propagation.

## 1127 6.2 MAGNETIC FIELD

1128 The magnet system used in [ATLAS](#) is designed to provide a substantial magnetic  
 1129 field in the two regions where the trajectory of particles is measured, the inner  
 1130 detector and the muon spectrometer. The magnetic field provides a curvature  
 1131 to the trajectory of charged particles and allows the precision tracking measure-  
 1132 ments to make high resolutions measurements of  $p_T$ . To provide a magnetic field  
 1133 in these regions, [ATLAS](#) uses a hybrid system with four separate, superconduct-  
 1134 ing magnets. A single solenoid provides a 2 T axial magnetic field for the inner  
 1135 detector, while a barrel toroid and two endcap toroids produce a magnetic field  
 1136 of 0.5 and 1 T, respectively, for the muon detectors. This geometry is illustrated  
 1137 in Figure 15, and the parameters of the three magnet systems are summarized in  
 1138 Table 3.

1139 The central solenoid uses a single-layer coil with a current of 7.730 kA to gen-  
 1140 erate the 2 T axial field at the center of the magnet. The single-layer coil design  
 1141 enables a minimal amount of material to be used in the solenoid's construction,  
 1142 which is important because the solenoid is placed between the inner detector  
 1143 and the calorimeters. At normal incidence the magnet has only 0.66 radiation  
 1144 lengths worth of material, where one radiation length is the mean distance over

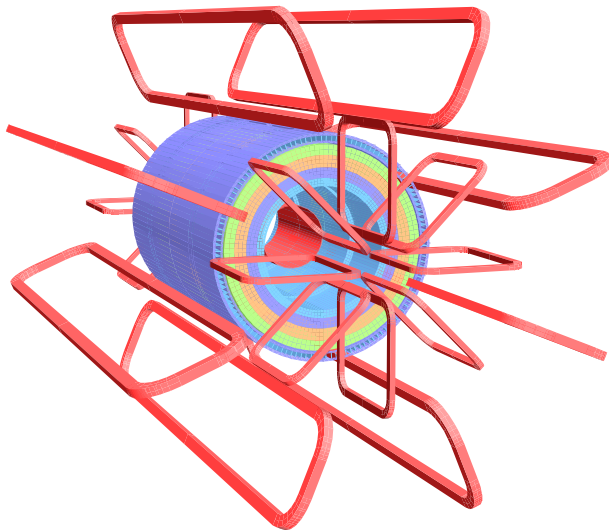


Figure 15: The layout of the four superconducting magnets in the [ATLAS](#) detector.

Parameter	Unit	Solenoid	Barrel Toroid	Endcap Toroids
Inner Diameter	m	2.4	9.4	1.7
Outer Diameter	m	2.6	20.1	10.7
Axial Length	m	5.3	25.3	5.0
Weight	tons	5.7	830	239
Conductor Size	mm <sup>2</sup>	30×4.25	57×12	41×4.25
Peak Field	T	2.6	3.9	4.1
Heat Load	W	130	990	330
Current	kA	7.7	20.5	20.0
Stored Energy	MJ	38	1080	206

Table 3: A summary of the parameters of each of the three magnet systems on [ATLAS](#).

1145 which a high-energy electron loses all but  $1/e$  of its energy through material in-  
 1146 teractions [7]. The coil is made of a high-strength aluminum stabilized NbTi  
 1147 superconductor which was optimized to achieve a high field with minimal thick-  
 1148 ness. The axial magnetic field produced by the solenoid bends charged particles  
 1149 in the  $\phi$  direction.

1150 The barrel toroid consists of eight coils which generate a 0.5 T magnetic field  
 1151 in the cylindrical region around the calorimeters with an approximately 20 kA  
 1152 current. The coils are separated only by air to reduce the scattering of muons as  
 1153 they propagate through the region. The coils are made of an aluminum stabilized  
 1154 NbTiCu superconductor and each is separately housed in a vacuum and cold  
 1155 chamber. This magnetic configuration produces a field in the  $\phi$  and so curves  
 1156 muons traversing the volume primarily in the  $\eta$  direction.

1157 The endcap toroids follow a similar design to the barrel toroid, with eight  
 1158 separate NbTiCu coils, but in this case all eight are housed within a single cold  
 1159 mass. This extra structure is necessary to withstand the Lorentz forces exerted  
 1160 by the magnets. These magnets are rotated 22.5% relative to the barrel toroid to  
 1161 provide a uniform field in the transition between the two systems. The endcap  
 1162 toroids also produce a field in the  $\phi$  direction and curve muons primarily in the  
 1163  $\eta$  direction.

### 1164 6.3 INNER DETECTOR

1165 The [ATLAS](#) inner detector provides excellent momentum resolution as well as  
 1166 accurate primary and secondary vertex measurements through robust pattern  
 1167 recognition that identifies tracks left by charged particles. These tracks fulfill  
 1168 a number of important roles in the [ATLAS](#) measurement system: they measure  
 1169 the momentum of charged particles including electrons and muons, they can  
 1170 identify electrons or photon conversions, they assign various particles and jets  
 1171 to different vertices, and they provide a correction to  $E_T^{\text{miss}}$  measurements from  
 1172 low energy particles. The system has to be accurate enough to separate tracks  
 1173 from dozens of vertices and to resolve each vertex individually, as well as accu-  
 1174 rate enough to measure the  $p_T$  of very high momentum tracks which curve very  
 1175 little even in the large magnetic field. This is accomplished by several indepen-  
 1176 dent layers of tracking systems. Closest to the interaction point is the very high  
 1177 granularity Pixel detector, which is followed by the [SCT](#) layers. These subdetec-  
 1178 tors both use discrete space-points to reconstruct track patterns. The final layer,  
 1179 the transition radiation tracker ([TRT](#)), uses many layers of straw tube elements  
 1180 interleaved with transition radiation material to provide continuous tracking.  
 1181 The arrangement of these subdetectors is shown in Figure 16. To provide the  
 1182 desired hermetic coverage, the subdetectors are divided into barrel and endcap  
 1183 geometries. Figure 17 shows the layout of the subdetectors in more detail, and  
 1184 illustrates how tracks at various pseudorapidities can traverse the subdetectors;  
 1185 tracks with  $\eta > 1.1$  begin to traverse the endcap subdetectors rather than those  
 1186 in the barrel, and tracks with  $\eta > 1.7$  use primarily endcap elements. The [IBL](#)  
 1187 was not present during the original commissioning of the inner detector and is  
 1188 not shown in this figure.

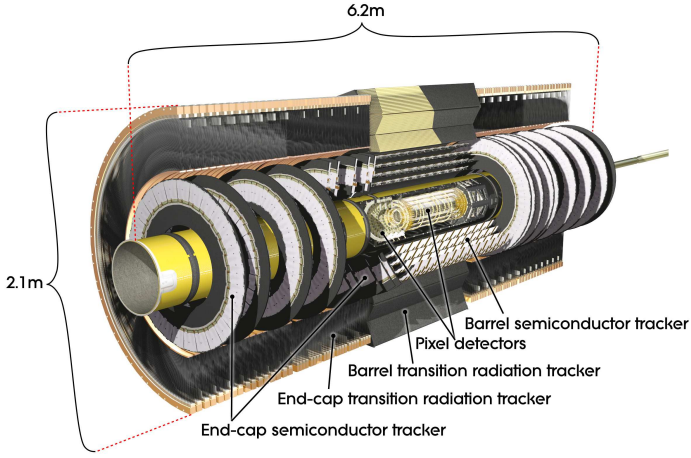


Figure 16: The arrangement of the subdetectors of the ATLAS inner detector. Each of the subdetectors is labeled in the cut-away view of the system.

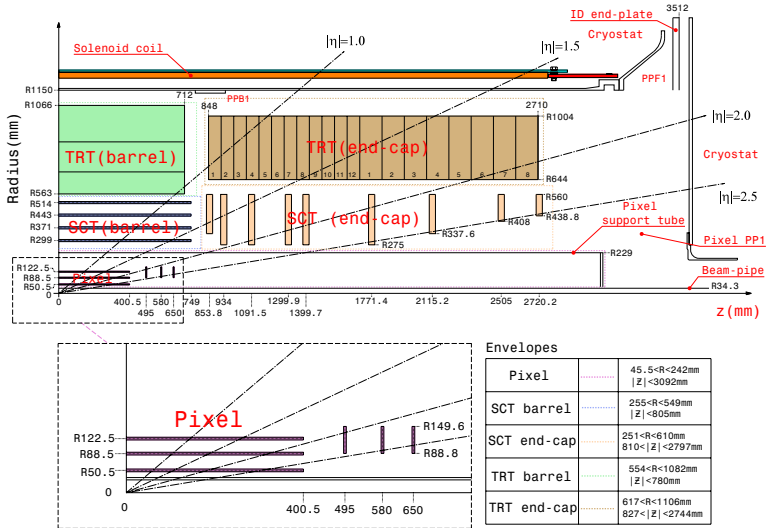


Figure 17: A quarter section of the ATLAS inner detector which shows the layout of each of the subdetectors in detail. The lower panel shows an enlarged view of the pixel detector. Example trajectories for a particle with  $\eta = 1.0, 1.5, 2.0, 2.5$  are shown. The IBL, which was added after the original detector commissioning, is not shown.

1189      Figure 18 shows a computer generated three-dimensional view of the inner  
 1190      detector along the beam axis, which emphasizes the straw tube structure of the  
 1191      **TRT** as well as the overlapping geometry of the **SCT**. This figure also includes  
 1192      the **IBL**, which was added during the long shutdown and provides an additional  
 1193      measurement layer in the Pixel detector as of the beginning of Run 2. Figure 19  
 1194      shows an alternative computer generated three-dimensional view transverse to  
 1195      the beam axis which emphasizes the endcap structures of the **SCT** and **TRT**.

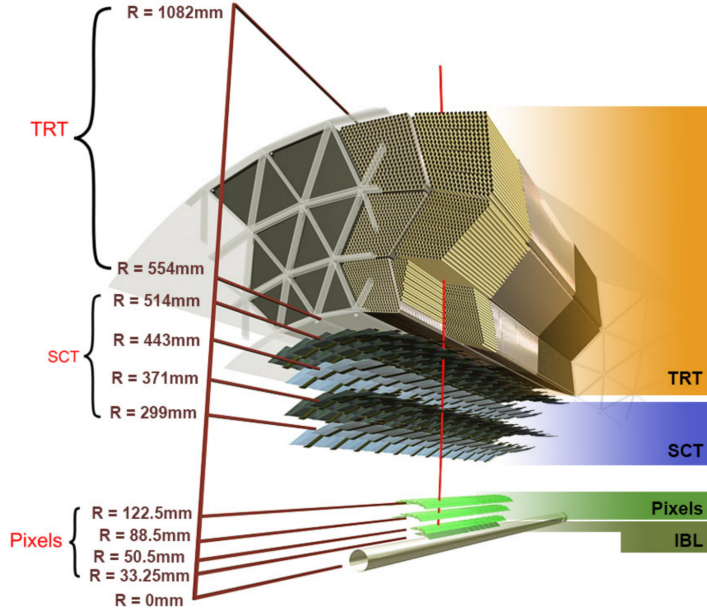


Figure 18: A computer generated three-dimensional view of the inner detector along the line of the beam axis. The subdetectors and their positions are labeled.

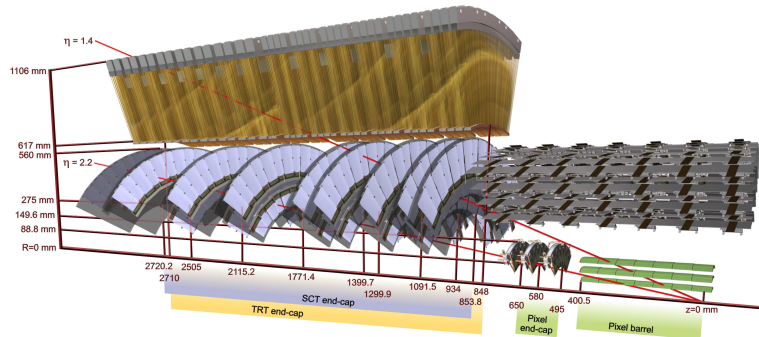


Figure 19: An alternative computer generated three-dimensional view of the inner detector transverse to the beam axis. The subdetectors and their positions are labeled.

1196      As the closest system to the interaction point, it is crucial for the inner de-  
 1197      tector to use as little material as possible to avoid scattering of charged parti-  
 1198      cles or photon conversions before they reach the remaining subdetectors. The  
 1199      various components, including the readout electronics, cooling infrastructure,  
 1200      gas volumes, and support structures, were designed to use as little material as

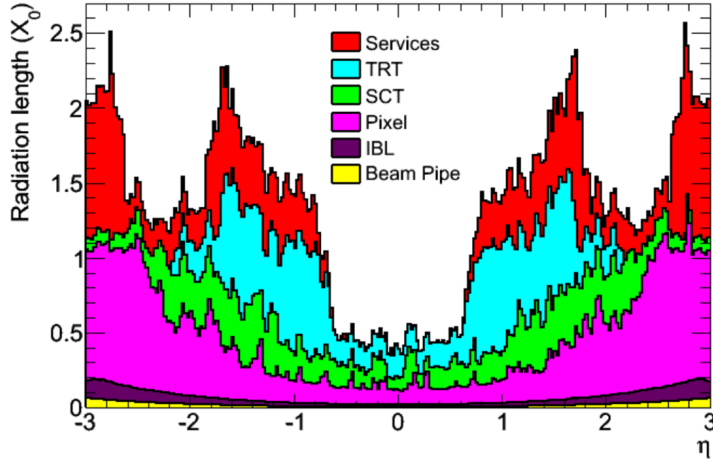


Figure 20: The integrated radiation lengths traversed by a straight track at the exit of the ID envelope, including the services and thermal enclosures. The distribution is shown as a function of  $|\eta|$  and averaged over  $\phi$ . The breakdown indicates the contributions of individual sub-detectors, including services in their active volume.

possible. Even with these optimizations, the combination of stringent performance requirements and the harsh radiation environment in the inner detector requires a significant amount of material. This material causes many electrons to lose most of their energy before reaching the electromagnetic calorimeter and approximately 40% of photons convert into an electron-positron pair while traversing the inner detector. Figure 20 shows the integrated radiation lengths traversed by a straight track in the inner detector as a function of  $\eta$ , grouped by subdetector. There is a large increase in the amount of material for support structures around  $|\eta| = 1.7$ , where the inner detector transitions from barrel to endcap.

The inner detector is designed to work as a cohesive unit to provide complete tracking information for charged particulars, and the subdetectors are complementary. Table 4 summarizes the parameters of each of the subdetectors as well as the parameters of the combined inner detector. Table 5 summarizes the expected performance that can be achieved by the inner detector as a whole.

### 6.3.1 PIXEL DETECTOR

The Pixel detector is the closest detector to the interaction point and therefore is designed to provide extremely high granularity while simultaneously handling a very large dose of radiation from collisions. It consists of four layers of silicon pixel modules, each of which provides a precision measurement on the trajectory of any charged particle. In the barrel region, the four layers are located at radial distances of 31 mm, 51 mm, 89 mm, and 123 mm. The three outer layers also include endcap elements, illustrated in Figure 17, which are located at 495 mm, 580 mm, and 650 mm away from the interaction point.

Parameter	Inner Detector	Pixel	SCT	TRT
Inner Radius	3.1 cm	3.1 cm	30 cm	56 cm
$ \eta $ Coverage	-	2.5	2.5	2.0
Cell Width	-	50 $\mu\text{m}$	80 $\mu\text{m}$	4 mm
Cell Length	-	400 $\mu\text{m}$	12 cm	70 cm
Material at $ \eta  = 0.0$	$0.3 X/X_0$			
Material at $ \eta  = 1.7$	$1.2 X/X_0$			
Material at $ \eta  = 2.5$	$0.5 X/X_0$			
Number of Hits	48	4	8	36
Channels	99 M	92 M	6.3 M	350 k

Table 4: A summary of the parameters of the inner detector and each of the subdetectors [3].

1225      The pixel sensor technology uses a p-n junction of n-type bulk that contains  
 1226      both p<sup>+</sup> and n<sup>+</sup> impurities. This combination is crucial in maintaining perfor-  
 1227      mance after a significant radiation dose, as the n<sup>+</sup> implants allow the sensor to  
 1228      continue function after the n-type bulk has been converted to a p-type bulk by  
 1229      the accumulation of radiation.

1230      The size of the pixels in the original three layers are 50  $\mu\text{m} \times$  400  $\mu\text{m}$  in the  
 1231       $r - \phi$  and  $z$  directions, respectively. Those pixels are bump-bonded to front-end  
 1232      readout chips, the FE-I3, which contains a total of 2880 pixels per chip. In the  
 1233      three original pixel layers, the chips are grouped into modules composed of 16  
 1234      chips each with 46,080 pixels per module and a total size of 20 mm x 60 mm  
 1235      x 250  $\mu\text{m}$ . The modules are further arranged into long rectangular structures  
 1236      that run parallel to the beamline called staves. By tiling several staves with an  
 1237      offset of 20°, the stave geometry provides full azimuthal coverage in the barrel  
 1238      region while accommodating the readout and cable systems. The endcap regions  
 1239      are instead arranged into petals and then into wheels. This arrangement can be  
 1240      seen in Figure 21 which shows a computer-generated, cut-away image of the  
 1241      outer three layers of the pixel detector. Together these three layers contain 1744  
 1242      modules between the barrel and two endcap sections.

1243      The innermost layer, the IBL, was added during the long shutdown before Run  
 1244      2, and provides the fourth track measurement. It was inserted directly into the  
 1245      existing pixel detector by removing the existing beam pipe and replacing it with  
 1246      a significantly smaller version. This insertion can be seen in action in Figure 22,  
 1247      which emphasizes the extreme precision required to place the the 70 cm long  
 1248      layer with only 2 mm of clearance. The IBL was commissioned to provide con-  
 1249      tinued tracking robustness and high precision in the higher luminosity environ-  
 1250      ment of Run 2 [9]. The proximity of this layer to the collisions necessitated an  
 1251      even higher granularity and better radiation hardness than the other pixel lay-  
 1252      ers. And the strict space requirements to add an active sensing layer so close to  
 1253      the interaction point required a sensor chip with a much higher active area and  
 1254      a larger overall area per chip. These requirements led to the development of a

Parameter	Particle	Value
Reconstruction Efficiency	Muon, $p_T = 1 \text{ GeV}$	96.8%
	Pion, $p_T = 1 \text{ GeV}$	84.0%
	Electron, $p_T = 5 \text{ GeV}$	90.0%
Momentum Resolution	$p_T = 1 \text{ GeV},  \eta  \approx 0$	1.3%
	$p_T = 1 \text{ GeV},  \eta  \approx 2.5$	2.0%
	$p_T = 100 \text{ GeV},  \eta  \approx 0$	3.8%
	$p_T = 100 \text{ GeV},  \eta  \approx 2.5$	11%
Transverse IP Resolution	$p_T = 1 \text{ GeV},  \eta  \approx 0$	$75 \mu\text{m}\%$
	$p_T = 1 \text{ GeV},  \eta  \approx 2.5$	$200 \mu\text{m}$
	$p_T = 1000 \text{ GeV},  \eta  \approx 0$	$11 \mu\text{m}$
	$p_T = 1000 \text{ GeV},  \eta  \approx 2.5$	$11 \mu\text{m}$
Longitudinal IP Resolution	$p_T = 1 \text{ GeV},  \eta  \approx 0$	$150 \mu\text{m}\%$
	$p_T = 1 \text{ GeV},  \eta  \approx 2.5$	$900 \mu\text{m}$
	$p_T = 1000 \text{ GeV},  \eta  \approx 0$	$90 \mu\text{m}$
	$p_T = 1000 \text{ GeV},  \eta  \approx 2.5$	$190 \mu\text{m}$

Table 5: A summary of the expected performance of the combined inner detector [8]. Included are the reconstruction efficiencies for multiple particle types as well as the momentum and IP resolution for various momenta.

1255 new chip type, the FE-I4 (compared to the FE-I3 chips used in the original pixel  
 1256 detector) with improved radiation hardness and a larger active footprint of 90%.  
 1257 The IBL is comprised of 448 of these individual chips arranged in 14 staves, with  
 1258 26,880 pixels per chip and a chip size of 18.5 mm x 41.3 mm x 200  $\mu\text{m}$ . The  
 1259 staves, like in the other layers of the pixel detector, are offset by 14° to provide  
 1260 full azimuthal coverage. This arrangement can be seen in Figure 23, which shows  
 1261 two computer-generated images of the IBL geometry and includes the some of  
 1262 the remaining pixel layers.

### 1263 6.3.2 SEMICONDUCTOR TRACKER

1264 The SCT, the subdetector which immediately surrounds the Pixel detector, pro-  
 1265 vides additional discrete measurements of the trajectory of a charged particle.  
 1266 Because the SCT is further away from the interaction point, the spatial resolution  
 1267 does not need to be as high as in the pixel detector, and so the SCT uses micro-  
 1268 strips instead of pixels. Although pixels provide a more accurate measurement,  
 1269 the number of pixels and readout channels required to cover the cylindrical area  
 1270 at the radius of the SCT layers would be prohibitively complicated and expensive.

1271 Each individual silicon strip sensor contains 768 individual readout strips  
 1272 with a total area of 6.36 cm x 6.40 cm and a pitch of 80  $\mu\text{m}$ . Pairs of these sen-  
 1273 sors are then bonded together to form a combined strip with a length of 12.8 cm.  
 1274 Two of these combined strips are then placed back to back with a relative tilt

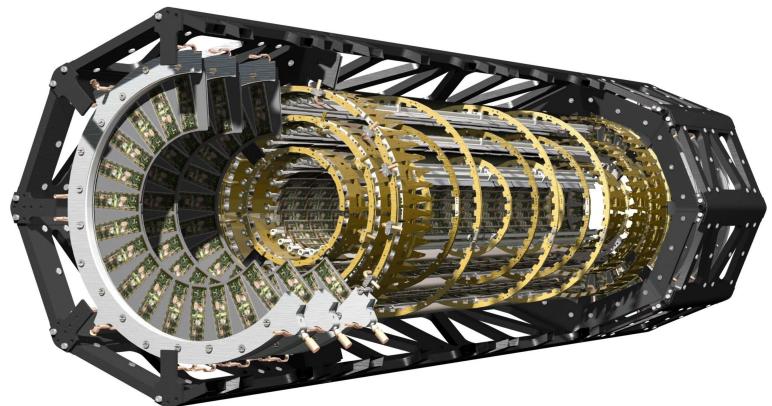


Figure 21



Figure 22: An image of the insertion of the [IBL](#) into the current pixel detector.

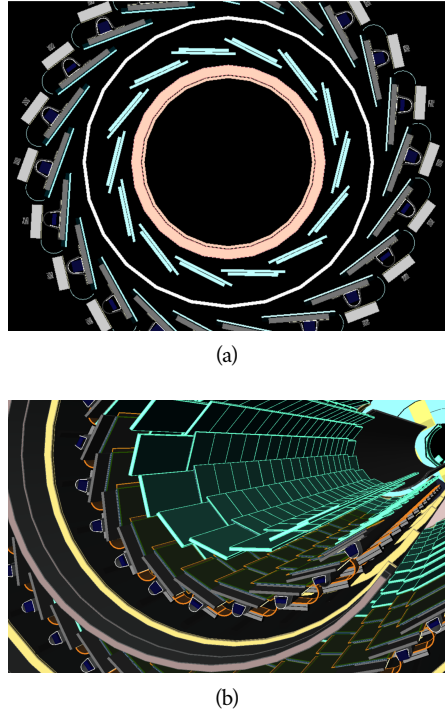


Figure 23: A three-dimensional computer-generated image of the geometry of the [IBL](#) with a view (a) mostly transverse to the beam pipe (b) mostly parallel to the beam pipe.

of 40 mrad. This geometry is illustrated in an exploded-out view in Figure 24. The purpose of angular offset of the consecutive layers is to allow the strip sensor areas to more accurately measure the position of a particle by comparing the overlap of the two strips which were traversed by a track.

Four of these double layers are placed in the barrel region, with radii of 284 mm, 355 mm, 427 mm, and 498 mm. Together these layers provide eight additional measurements for each track that traverses the central  $|\eta|$  region. In the endcap region, the layers are arranged in wheels, with the double layers similarly offset to provide improved resolution. With these configurations, the [SCT](#) achieves a spatial resolution of  $17 \mu\text{m}$  in the  $r - \phi$  direction and  $580 \mu\text{m}$  in the  $z$  direction.

### 6.3.3 TRANSITION RADIATION TRACKER

The final component of the inner detector, the [TRT](#), provides continuous tracking using straw drift tubes. The tubes are made of Kapton and aluminum with a diameter of 4 mm and are filled with a gas mixture of 70% Xe, 27% CO<sub>2</sub>, and 3% O<sub>2</sub>. At the center of each tube is a gold-plated anode tungsten wire  $30 \mu\text{m}$  in diameter. When a charged particle passes through these tubes, it ionizes the gas within. The ions produced drift in the electric field established between the wire and the tube wall, and the large electric field near the wire produces avalanche multiplication and results in an electric current on the wire that is read out by the electronics and provides a track measurement. The time it takes the ioniza-

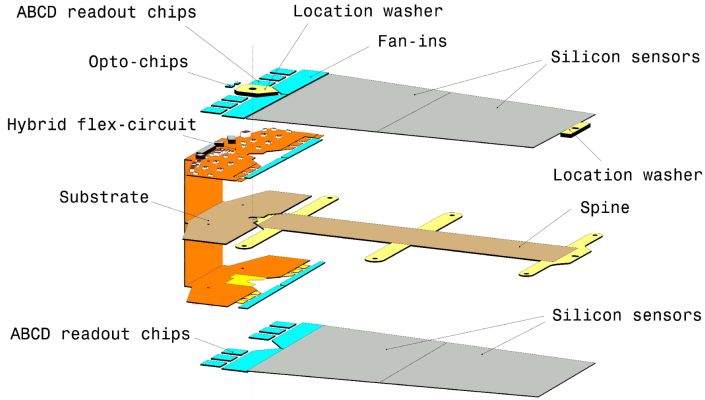


Figure 24: An exploded view of the geometry of the [SCT](#) double layers in the barrel region.

tion to drift to the wire can be used to estimate the distance from the wire that the particle passed through the tube; this gives a resolution on the distance of approximately  $130\mu\text{m}$ . Combining several such measurements between consecutive hits in the [TRT](#) tubes allows the trajectory of the particle to be reconstructed.

In addition to the continuous tracking, the detector can use transition radiation produced when a particle passes between the layers to distinguish between electrons and heavier charged particles. The space between the tubes is filled with  $\text{CO}_2$ , and so has a different dielectric constant than the gas within the tubes which contains Xe. At the transition between those media, a relativistic particle emits radiation proportional to  $\gamma$ , so inversely proportional to mass at a fixed momentum. The photons produced in this transition then produces an ionization cascade which is significantly larger than the signal for the minimally-ionizing charged particles. To distinguish between these two cases, the [TRT](#) defines two signal thresholds, a low threshold for the typical signal produced by a minimally ionizing particle ([MIP](#)) and a high threshold for the the signal produced by transition radiation. A high momentum electron is expected to produce approximately 7 to 10 high threshold hits as it traverses the [TRT](#), and thus these hits provide a way to distinguish electrons from other charged particles.

The [TRT](#) contains 351,000 tubes in total, divided between the barrel and endcap regions. In the barrel region, the tubes are 144 cm long and arranged in 73 layers parallel to the beampipe. In the endcap region, the tubes are 37 cm long and arranged in 160 layers transverse to the beampipe. These configurations can be seen in Figure 18 and Figure 19. With this geometry the [TRT](#) achieves a resolution of  $130\mu\text{m}$  in the  $r - \phi$  direction.

## 6.4 CALORIMETRY

The combination of calorimeter systems used in [ATLAS](#) can measure the energy of electrons, photons, hadrons, and hadronic jets with complete coverage up to  $|\eta| < 4.9$  and across  $\phi$ . Unlike the inner detector, the calorimeters are capable of measuring neutral particles. To accomplish precision measurements of these

1325 particle types, the [ATLAS](#) calorimeter system uses four individual calorimeters,  
 1326 a [LAr](#) electromagnetic calorimeter in the barrel region, a tile hadronic calorime-  
 1327 ter in the barrel region, a [LAr](#) hadronic endcap calorimeter, and a [LAr](#) forward  
 1328 calorimeter. Together these provide hermetic coverage for the [ATLAS](#) detector.  
 1329 The configuration of these calorimeters is illustrated in Figure 25. **Note: I could**  
 1330 **make this section much longer. It might be nice to include a more com-**  
 1331 **plete description of showers for example. I will extend this section if their**  
 1332 **is space at the end.**

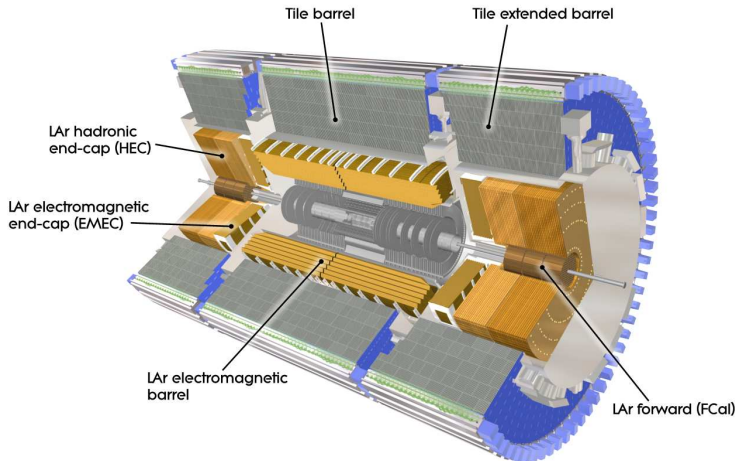


Figure 25

1333 The calorimeters are designed to absorb and measure the energy carried by  
 1334 a particle, and completely stop the particle's propagation in the process. This  
 1335 requires a significant amount of material to provide interactions. These interac-  
 1336 tions then produce secondary particles, which can produce secondary particles  
 1337 in turn, and thus form a cascade of particles called an electromagnetic ([EM](#)) or  
 1338 hadronic shower, depending on the governing mechanism. Electromagnetic and  
 1339 hadronic showers have very different properties and require different technolo-  
 1340 gies to measure them accurately. All of the calorimeters in the [ATLAS](#) calorimeter  
 1341 system are sampling calorimeters, that is they use alternating layers of absorbing  
 1342 and active material. The dense absorbing layers initiate the showers while the ac-  
 1343 tive layers measure the energy of the produced particles. A fraction of the energy  
 1344 is lost in the inactive layers, so the energy measurement from the active layers  
 1345 has to be corrected to estimate the actual energy of the particle.

1346 The [EM](#) calorimeter provides around 20 radiation lengths ( $X_0$ ) while the hadronic  
 1347 calorimeter provides around 10 interaction lengths ( $\lambda_0$ ). As mentioned previ-  
 1348 ously, radiation lengths measure the distance over which an electromagnetically  
 1349 interacting particle loses a characteristic fraction of its energy. Interaction lengths,  
 1350 on the other hand, measure the mean distance traveled by a hadronic particle be-  
 1351 fore undergoing a nuclear interaction [7]. Figure 26 show the radiation lengths  
 1352 in the layers of the [EM](#) calorimeter in the barrel region as well as the interaction  
 1353 lengths for all calorimeters.

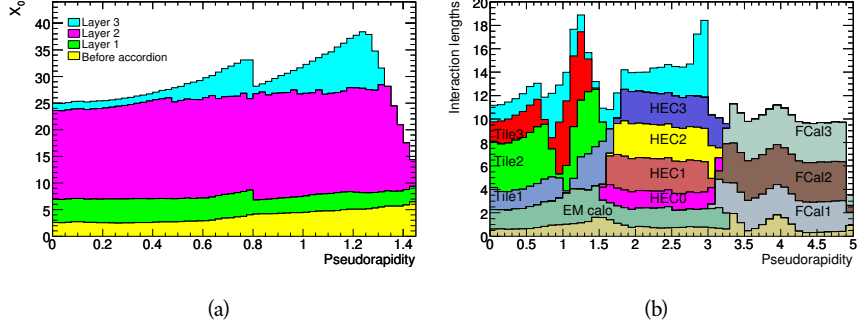


Figure 26: The depth of (a) the electromagnetic barrel calorimeter in radiation lengths and (b) all calorimeters in interaction lengths as a function of pseudorapidity.

## 1354 6.41 ELECTROMAGNETIC CALORIMETER

1355 The electromagnetic calorimeters use alternating layers of Liquid Argon and  
1356 lead in an accordion shape. The accordion shape allows a construction that pro-  
1357 vides complete coverage in the  $\phi$  direction while also providing many alterna-  
1358 ting layers for the a particle to pass through. The configuration is detailed in  
1359 Figure 27. When an electron or photon passes through the lead, it produces an  
1360 electromagnetic shower. The particles produced in those showers then pass into  
1361 and ionize the Liquid Argon; the ions produced can then be collected by an elec-  
1362 trode in the Liquid Argon layer to provide the actual energy measurement.

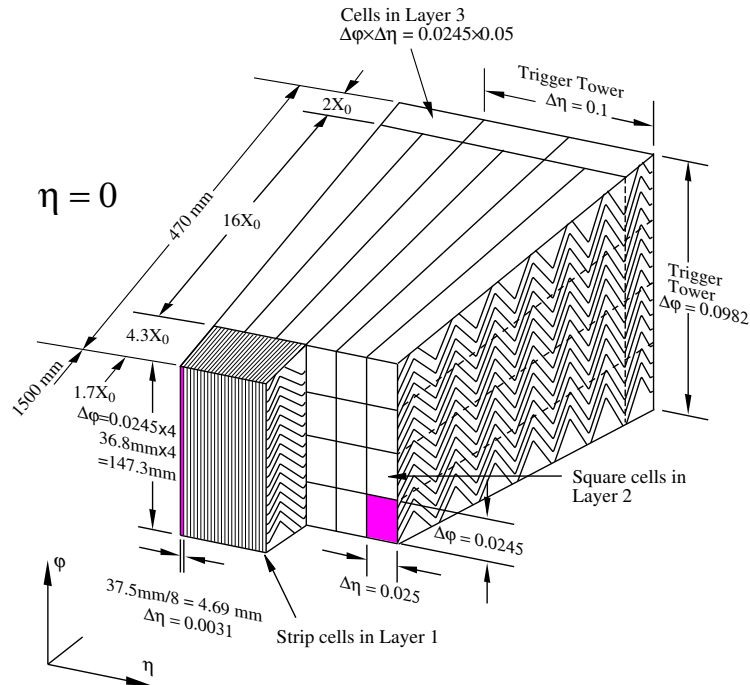


Figure 27: A schematic of the LAr calorimeter in the barrel region, highlighting the accordion structure.

The barrel region is covered by a presampler and three separate sampling layers with decreasing segmentation. The presampler is just a thin layer of Liquid Argon which measures the energy of any electromagnetic showers which are initiated before the particle reaches the calorimeter due to interactions with the detector material. The first layer is the strip layer, which has fine segmentation in  $\eta$  to enhance the identification of shower shapes and to provide a precise  $\eta$  measurement for reconstructing photons and electrons. The strip layer has only 4 radiation lengths worth of material, and has a segmentation of  $\Delta\eta = 0.003$  and  $\Delta\phi = 0.1$ . The second layer is also finely segmented, with a segmentation of  $\Delta\eta = 0.025$  and  $\Delta\phi = 0.025$ , and a thickness of  $16 X_0$ . This layer is designed to contain an electromagnetic shower and to measure the majority of the energy for photons and electrons. The third layer is only  $2 X_0$  thick and measures the energy of electromagnetic showers which leak out of the second layer, and helps to separate electromagnetic showers from hadronic showers. The structure of the LAr endcap calorimeter is similar except that the layers are arranged parallel to the beampipe to measure energy deposits from high  $\eta$  particles.

#### 6.4.2 HADRONIC CALORIMETERS

The hadronic calorimeters use a few different technologies to satisfy the resolution demands in the different areas of the detector, and together they cover the region  $|\eta| < 2.7$ . In the barrel region, for  $|\eta| < 1.7$ , the hadronic calorimeters are constructed of alternating tiles of steel and plastic scintillator. Like in the electromagnetic calorimeter, the dense layer initiates a shower (in this case the dense layer is the steel and the shower is hadronic) of particles which pass into and ionize the following layer. The ionization in the plastic scintillator instead produces a light signal proportional to the amount of ionization produced by the shower, and this signal is measured using photomultipliers and provides the actual energy measurement. The construction of a tile in the calorimeter is shown Figure 28, which highlights the alternating layers of steel and scintillator.

This tile calorimeter, as well as the remaining hadronic calorimeters, have a much coarser granularity than the electromagnetic calorimeters. The high granularity is not needed for an accurate energy measurement, and the hadronic calorimeters are not designed to distinguish particle types like the electromagnetic calorimeters. The tile granularity is approximately  $\Delta\eta = 0.1$  and  $\Delta\phi = 0.1$ , and the segmentation in depth and  $\eta$  is shown in Figure 29.

The remaining hadronic calorimeters all use the same alternating, sampling structure but with different active and inactive materials. The hadronic endcap calorimeter covers the range of  $1.5 < |\eta| < 3.2$  and uses an inactive layer of copper and an active layer of Liquid Argon. The forward calorimeter covers the range of  $3.1 < |\eta| < 4.9$  and uses a dense matrix of copper and tungsten filled with Liquid Argon.

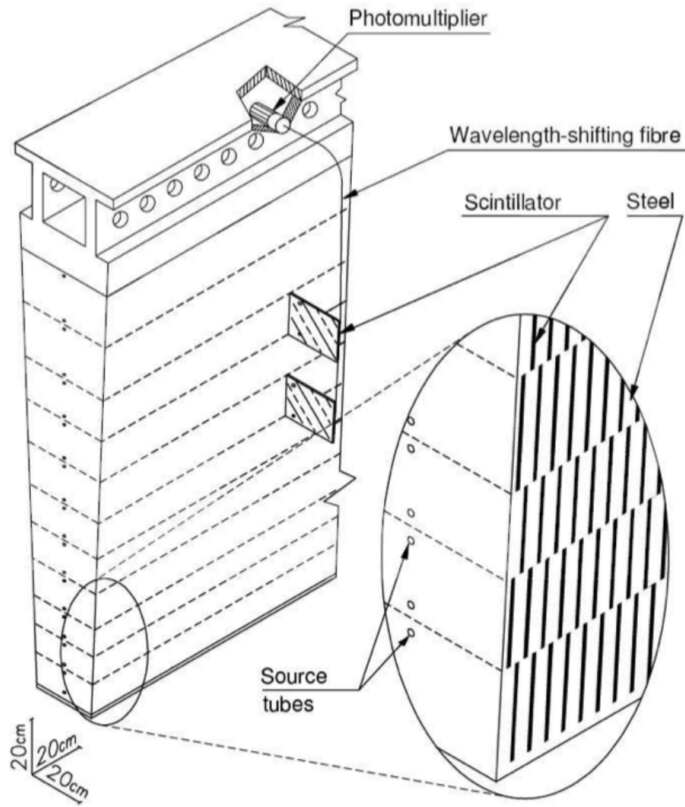


Figure 28: A schematic of a hadronic tile module which shows the alternating layers of steel and plastic scintillator.

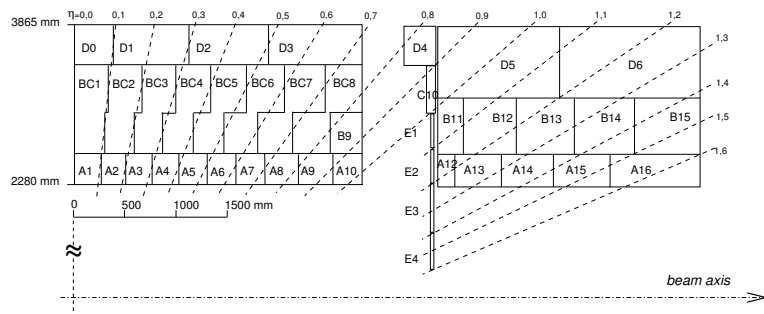


Figure 29: The segmentation in depth and  $\eta$  of the tile-calorimeter modules in the central (left) and extended (right) barrels.

## 1403 6.5 MUON SPECTROMETER

1404 Among SM particles, only muons and neutrinos consistently pass through the  
 1405 calorimeters. Because the neutrinos are also electrically neutral, there is no fea-  
 1406 sible option to measure them directly in ATLAS. The muons, on the other hand,  
 1407 are charged and are thus already measured as a track in the inner detector. The  
 1408 muon spectrometer provides a way to consistently identify muon tracks and also  
 1409 a way to provide an additional measurement of their momentum.

1410 The muon spectrometer contains four subdetectors that cover the barrel and  
 1411 endcap regions. In the barrel region, the muon spectrometer uses a combination  
 1412 of Resistive Plate Chambers (RPCs) and MDTs to provide both a coarse, fast mea-  
 1413 surement for triggering and a precise momentum measurement for offline event  
 1414 reconstruction. Similarly, in the endcap region, the TGCs, MDTs, and CSCs allow  
 1415 for both triggering and precise measurements. The CSCs are used only in the in-  
 1416 nermost layer of the endcap region between  $2.0 < |\eta| < 2.7$  where the particle  
 1417 flux is too large for the MDTs to provide accurate measurements. The overall  
 1418 layout of the muon systems are shown in the cut-away diagram in Figure 30,  
 1419 and Figure 31 shows a precise schematic of the layout of each of the detecting  
 1420 elements. The geometric arrangement shown provides consistent coverage for  
 1421 muons produced up to  $|\eta| < 2.7$ , and takes full advantage of the bending of the  
 1422 muons in the toroidal magnetic field, described in Section 6.2, to measure their  
 1423 momentum. Figure 32 shows a cross-section of the arrangement of the muon  
 1424 spectrometer in the barrel; the layers are divided into eight small and eight large  
 1425 chambers that are overlapped to provide complete coverage in  $\phi$ .

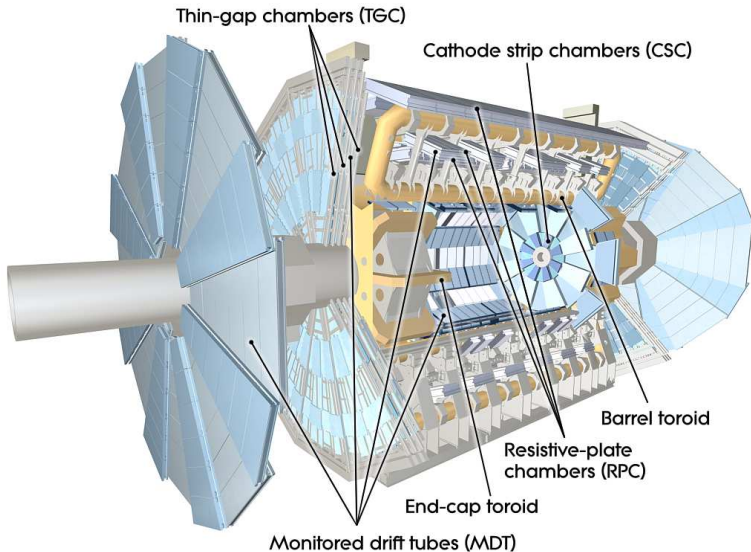


Figure 30: A cut-away diagram of the muon systems on ATLAS.

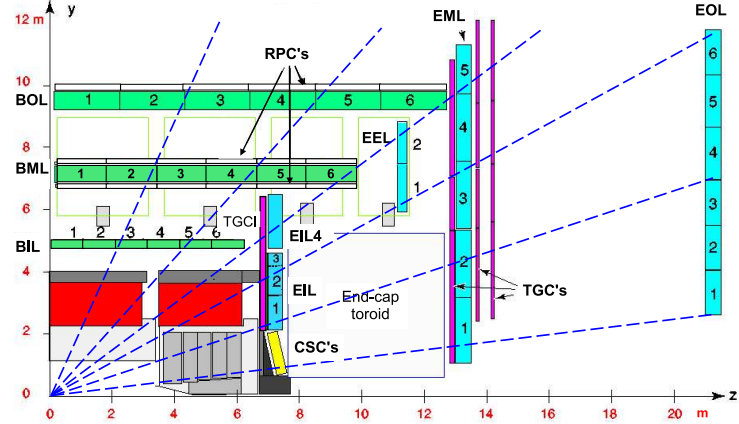


Figure 31: A quarter view of the muon spectrometer which highlights the layout of each of the detecting elements. The BOL, BML, BIL, EOL, EML, and EIL are all MDT elements, where the acronyms encode their positions.

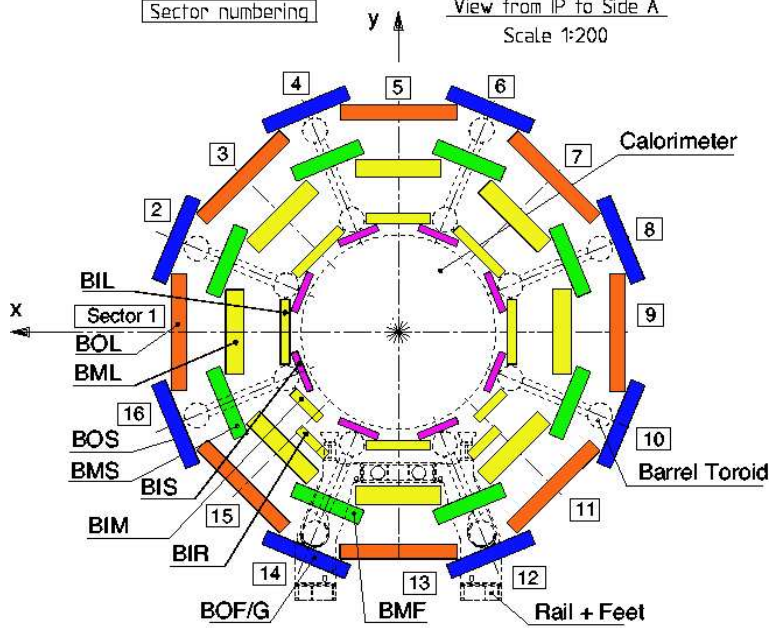


Figure 32: A schematic of the cross-section of the muon spectrometer in the barrel region.

## 1426 6.5.1 MONITORED DRIFT TUBE

1427 The momentum measurements in the barrel region are provided by three con-  
 1428 secutive layers of MDT elements, located at approximately 5 m, 7 m, and 9 m from  
 1429 the interaction point. Each of these layers is a composite of two multilayers of  
 1430 drift tubes: two layers of three to four layers of tubes, as shown in Figure 33.  
 1431 These aluminum tubes are 3 cm in diameter, with lengths between 0.9 and 6.2 m,  
 1432 and are filled with a mixture of ArCO<sub>2</sub> kept at 3 bar absolute pressure. A central  
 1433 tungsten-rhenium wire with a diameter of 50  $\mu\text{m}$  runs along the length of the  
 1434 tube, and is kept at a potential of 3080 V.

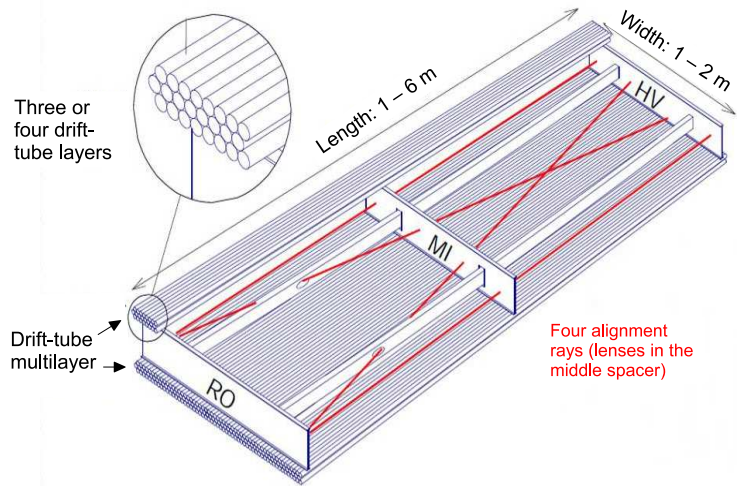


Figure 33: A schematic of a single MDT chamber, which shows the multilayers of drift tubes as well as the alignment system.

1435 A muon traversing these tubes ionizes the gas, and the ionization electrons  
 1436 then drift in the electric field toward the central wire. Close to the wire, the  
 1437 electric field is strong enough to cause the original ionization electrons to ion-  
 1438 ize additional electrons, producing an avalanche that can be measured as a cur-  
 1439 rent along the wire. The time of arrival of that current depends on how far the  
 1440 muon entered from the wire, and can be used to achieve a position resolution of  
 1441 80  $\mu\text{m}$  in an individual tube. The combination of the measurements in the con-  
 1442 secutive layers of tubes improves this position resolution to 35  $\mu\text{m}$ .

1443 To achieve a good resolution over the entire length of a muon track, the rel-  
 1444 ative positions of the tubes of the muon spectrometer must be known to an ac-  
 1445 curacy of 30  $\mu\text{m}$ . This is achieved by an optical laser alignment system placed in  
 1446 each of the individual chambers and throughout the cavern. These monitor any  
 1447 changes in position or alignment due to effects like gravitational sag, tempera-  
 1448 ture shifts, and the magnetic field. The configuration of the alignment system  
 1449 within an individual chamber is also shown in Figure 32.

## 1450 6.5.2 RESISTIVE PLATE CHAMBER

1451 The **RPC** is the outermost detecting layer in the muon spectrometer in the barrel  
 1452 region, and provides a fast measurement of the  $\phi$  position of muons for trig-  
 1453 gering. The speed of the measurement, with a time resolution of just a few  
 1454 nanoseconds, requires a poor spatial resolution of approximately 1 cm. There  
 1455 are three **RPCs** layers in the muon spectrometer, two located on either side of  
 1456 the central **MDT** layer and one located outside the final **MDT** layer, as shown in  
 1457 Figure 31. The **RPCs** consist of two layers of parallel plates filled with a gas mix-  
 1458 ture of  $C_2H_2F_4$ . A muon passing through these systems ionizes the gas, like in  
 1459 the **MDT**, which causes an avalanche of ionization electrons in the electric field  
 1460 maintained between the plates. Metal strips on the outside of the chamber ca-  
 1461 pacitively couple to the accumulated charge, and are read out to measure the  $\eta$   
 1462 and  $\phi$  positions of the muon track.

## 1463 6.5.3 CATHODE STRIP CHAMBER

1464 The majority of the momentum measurements in the endcap region are provided  
 1465 by the **MDTs**. In the most forward region of the muon spectrometer, between  
 1466  $2.0 < \eta < 2.7$ , the particle flux is very high due to contributions from low energy  
 1467 photons and neutrons. The **MDT** can only sustain a hit rate of approximately 150  
 1468 Hz/cm<sup>2</sup> because of limitations in the drift times of the gas and the capacity of  
 1469 the readout electronics. The **CSCs** were designed to handle higher hit rates, up to  
 1470 1000 Hz/cm<sup>2</sup>, and provide the necessary coverage in that high flux region.

1471 The **CSC** consists of several multiwire proportional chambers, where the wires  
 1472 are oriented in the radial direction out from the beampipe. There are eight large  
 1473 and eight small chambers, arranged to partially overlap in the  $\phi$  direction, as  
 1474 shown in Figure 34. Like in the **MDT**, a muon traversing the system produces  
 1475 ionization in the gas; here, however, the ionization is collected on a number of  
 1476 wires. These wires couple to cathodes on the chambers which are segmented  
 1477 into strips in two directions. The relative amount of charge on each of the neigh-  
 1478 boring strips can be used to interpolate to the position of the muon in both  $\eta$   
 1479 and  $\phi$ .

## 1480 6.5.4 THIN GAP CHAMBER

1481 Like in the barrel region, a separate, fast detector is required to provide position  
 1482 measurements of muons for trigger in the endcap region. This is provided by  
 1483 the **TGC** which consists of seven layers in the middle station of the endcap, two  
 1484 doublet layers and one triplet layer, and a single doublet layer in the inner endcap  
 1485 station. Figure 35 shows the arrangement of the triple and doublet layers of the  
 1486 **TGCs**.

1487 Like the **CSCss**, the **TGCs** are multiwire proportional chambers with a wire-to-  
 1488 cathode distance of 1.4 mm and a wire-to-wire distance of 1.8 mm. Readout  
 1489 strips on the outside of the chambers run perpendicular to the wires, and couple  
 1490 to the charge collected on the wires to provide a position measurement in the  $\eta$

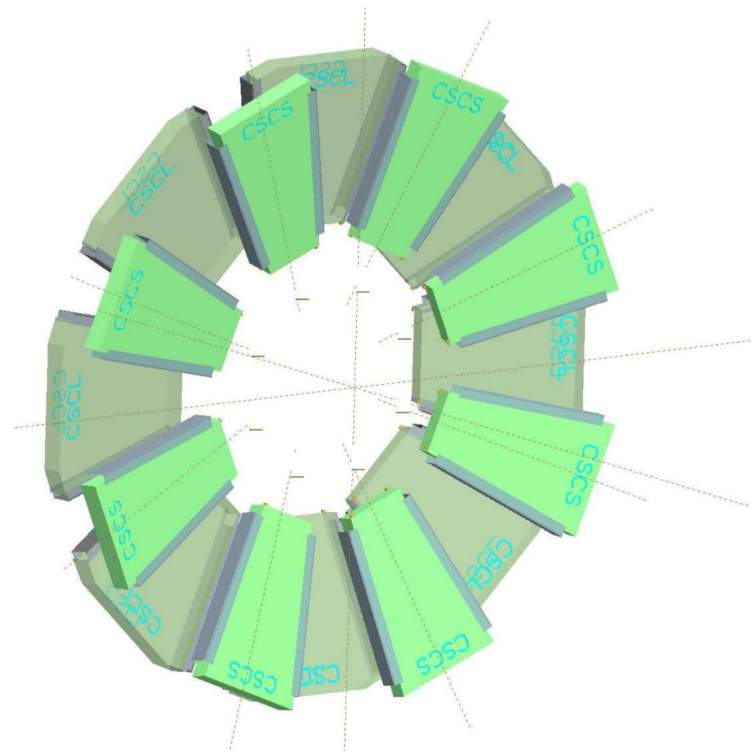


Figure 34: A schematic of the **CSC** endcap, showing the overlapping arrangement of the eight large and eight small chambers.

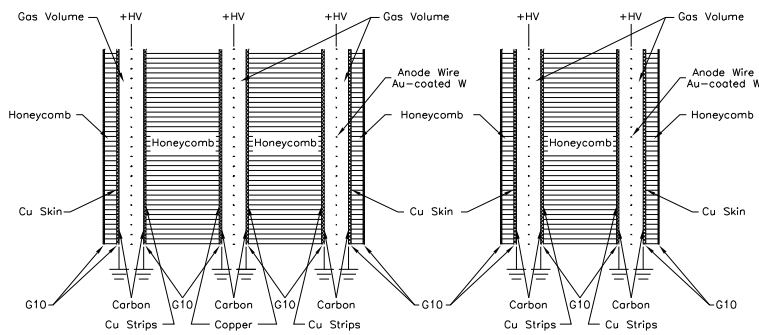


Figure 35: A schematic of the **TGC** doublet and triplet layers.

1491 direction. The current induced on the wires is also readout to provide a position  
 1492 measurement in the  $\phi$  direction. The high electric field and small wire-to-wire  
 1493 distance give it the required good time resolution to be used for triggering events.

## 1494 6.6 TRIGGER

1495 It is not possible for the detector and the associated computing systems to record  
 1496 the terabytes of data that the 40 MHz of proton-proton collisions produce every  
 1497 second. Instead, a small fraction of these events are selected by the trigger sys-  
 1498 tem to be recorded and later analyzed. Selecting interesting events at such a high  
 1499 rate poses a significant challenge for the both the detector design and the imple-  
 1500 mentation of a trigger decision and data acquisition system. The trigger must  
 1501 balance the time needed to decide to keep an event, to avoid losing information,  
 1502 with the filtering accuracy to consistently select a full menu of physics events  
 1503 that can be used for the wide array of searches and measurements targeted by  
 1504 [ATLAS](#).

1505 The [ATLAS](#) trigger system, as of Run 2, consists of two levels of decision mak-  
 1506 ing. The first level, referred to as L1, is hardware based and uses inputs from  
 1507 a subset of the detector elements to narrow the considered event rate from the  
 1508 original 40 MHz down to 100 kHz. The 100 kHz rate is the maximal rate that  
 1509 the event information can be transferred from the detector. The second level,  
 1510 referred to as the [HLT](#), makes the final decisions on which events to keep for  
 1511 analysis and selects a rate of around 1 kHz. The collection of selection criteria  
 1512 used to make the L1 decisions feed into subsequent selection criteria in the [HLT](#),  
 1513 and the set of these combinations of L1 and [HLT](#) criteria from the trigger menu  
 1514 which defines exactly what events are recorded on [ATLAS](#). The entirety of the  
 1515 trigger menu used for 2015 data collection is shown in Table 6, which summa-  
 1516 rizes the selection requirements at both levels and additionally shows the peak  
 1517 measured rates contributed by each.

1518 At L1, the trigger system uses information primarily from the calorimeters  
 1519 and muon spectrometer to select high  $p_T$  jets, electrons, photons, and muons.  
 1520 The electromagnetic calorimeter uses reduced granularity energy measurements  
 1521 as well as isolation requirements to select electrons and photons. The hadronic  
 1522 calorimeter also uses a combination of reduced granularity energy measurements  
 1523 and isolation to select high momentum jets and hadronically decaying tau lept-  
 1524 tons. The calorimeters are also used to provide triggers based on missing energy:  
 1525 the coarse granularity energy measurements are used to calculate a directional  
 1526 sum of energies and to trigger on a significant imbalance. Only the [RPCs](#) and [TGCs](#)  
 1527 muon subdetectors contribute to the decision at L1, and are used to identify high  
 1528 momentum muons. The contributions to the triggering rate of the various types  
 1529 of L1 triggers are shown in Figure 36. The total rate is indicated in black and  
 1530 is lower than the sum of individual rates because their is significant overlap be-  
 1531 tween different trigger channels. The majority of the rate comes from lepton  
 1532 and photon triggers.

1533 After an event is chosen by the L1 trigger, the detector measurements from the  
 1534 bunch crossing which fired the trigger is read out from the front-end electronics

Trigger	Typical offline selection	Trigger Selection		Level-1 Peak Rate (kHz)	HLT Peak Rate (Hz)
		Level-1 (GeV)	HLT (GeV)	$L = 5 \times 10^{33} \text{ cm}^{-2}\text{s}^{-1}$	
Single leptons	Single iso $\mu$ , $p_T > 21$ GeV	15	20	7	130
	Single $e$ , $p_T > 25$ GeV	20	24	18	139
	Single $\mu$ , $p_T > 42$ GeV	20	40	5	33
	Single $\tau$ , $p_T > 90$ GeV	60	80	2	41
Two leptons	Two $\mu$ 's, each $p_T > 11$ GeV	$2 \times 10$	$2 \times 10$	0.8	19
	Two $\mu$ 's, $p_T > 19, 10$ GeV	15	18, 8	7	18
	Two loose $e$ 's, each $p_T > 15$ GeV	$2 \times 10$	$2 \times 12$	10	5
	One $e$ & one $\mu$ , $p_T > 10, 26$ GeV	$20 (\mu)$	7, 24	5	1
	One loose $e$ & one $\mu$ , $p_T > 19, 15$ GeV	15, 10	17, 14	0.4	2
	Two $\tau$ 's, $p_T > 40, 30$ GeV	20, 12	35, 25	2	22
	One $\tau$ , one $\mu$ , $p_T > 30, 15$ GeV	12, 10 (+jets)	25, 14	0.5	10
Three leptons	One $\tau$ , one $e$ , $p_T > 30, 19$ GeV	12, 15 (+jets)	25, 17	1	3.9
	Three loose $e$ 's, $p_T > 19, 11, 11$ GeV	15, 2 $\times$ 7	17, 2 $\times$ 9	3	< 0.1
	Three $\mu$ 's, each $p_T > 8$ GeV	3 $\times$ 6	3 $\times$ 6	< 0.1	4
	Three $\mu$ 's, $p_T > 19, 2 \times 6$ GeV	15	18, 2 $\times$ 4	7	2
One photon	Two loose $\gamma$ 's, $p_T > 40, 30$ GeV	$2 \times 10$	$2 \times 10 (\mu's)$	0.8	0.2
	Two tight $\gamma$ 's, $p_T > 25, 25$ GeV	$2 \times 8, 10$	$2 \times 12, 10$	0.3	< 0.1
Two photons	one $\gamma$ , $p_T > 125$ GeV	22	120	8	20
	Two loose $\gamma$ 's, $p_T > 40, 30$ GeV	$2 \times 15$	35, 25	1.5	12
Single jet	Two tight $\gamma$ 's, $p_T > 25, 25$ GeV	$2 \times 15$	$2 \times 20$	1.5	7
	Jet ( $R = 0.4$ ), $p_T > 400$ GeV	100	360	0.9	18
$E_T^{\text{miss}}$	Jet ( $R = 1.0$ ), $p_T > 400$ GeV	100	360	0.9	23
	$E_T^{\text{miss}} > 180$ GeV	50	70	0.7	55
Multi-jets	Four jets, each $p_T > 95$ GeV	$3 \times 40$	$4 \times 85$	0.3	20
	Five jets, each $p_T > 70$ GeV	$4 \times 20$	$5 \times 60$	0.4	15
	Six jets, each $p_T > 55$ GeV	$4 \times 15$	$6 \times 45$	1.0	12
$b$ -jets	One loose $b$ , $p_T > 235$ GeV	100	225	0.9	35
	Two medium $b$ 's, $p_T > 160, 60$ GeV	100	150, 50	0.9	9
	One $b$ & three jets, each $p_T > 75$ GeV	$3 \times 25$	$4 \times 65$	0.9	11
	Two $b$ & two jets, each $p_T > 45$ GeV	$3 \times 25$	$4 \times 35$	0.9	9
$b$ -physics	Two $\mu$ 's, $p_T > 6, 4$ GeV plus dedicated $b$ -physics selections	6, 4	6, 4	8	52
Total				70	1400

Table 6: The trigger menu for the 2015 data collection with  $L = 5 \times 10^{33} \text{ cm}^{-2}\text{s}^{-1}$ . Both the L1 and HLT selection requirements and their trigger rates are shown measured at the specified luminosity are shown. The typical offline selections represent a typical set of offline requirements imposed after the trigger in an analysis.

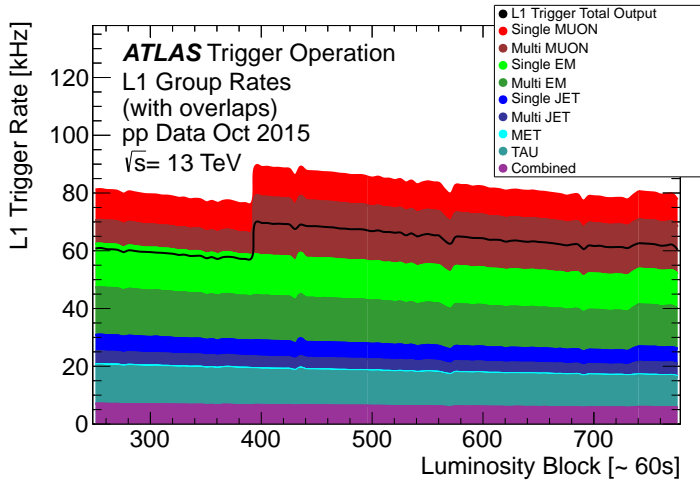


Figure 36: The L1 Trigger rate broken down into the types of triggers as a function of the luminosity block for the 2015 data collection period.

1535 and stored on read-out boards. This inclusive information is necessary to make  
 1536 more the more precise event selections than is possible with the reduced infor-  
 1537 mation at L1. The **HLT** then uses this information with software algorithms to  
 1538 decide whether or not to permanently record the event. The L1 trigger also for-  
 1539 wards which decision was made and Region of Interests (**RoIs**) to the **HLT**, which  
 1540 allows the **HLT** to focus on particular algorithms and particular sections of the  
 1541 detector to greatly improve the algorithmic selection speed. The additional in-  
 1542 formation available to the **HLT** allows it to implement additional trigger targets,  
 1543 such as identified jets from the decays of b-hadrons. The contributions to the  
 1544 triggering rate of the various types of **HLT** triggers are shown in Figure 37.

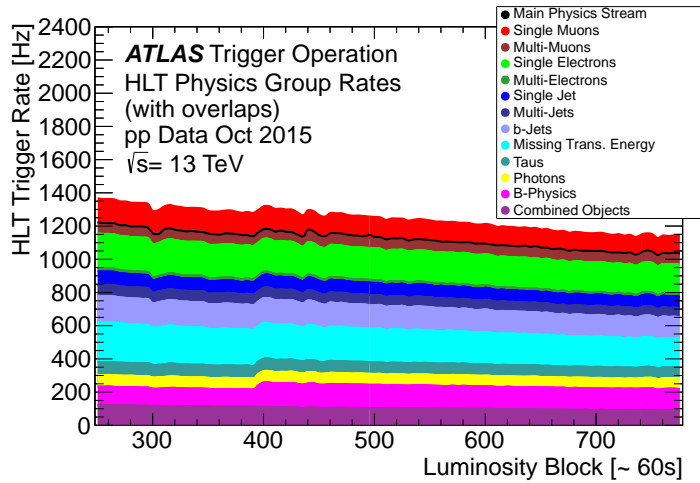


Figure 37: The HLT Trigger rate broken down into the types of triggers as a function of the luminosity block for the 2015 data collection period.

1545

1546 EVENT RECONSTRUCTION

---

1547 The ATLAS experiment combines measurements in the subdetectors to form a  
 1548 cohesive picture of each physics event. The majority of particles that traverse  
 1549 the detector leave behind some combination of ionization hits in the tracking  
 1550 detectors or energy deposits in the calorimeters, and these measurements can  
 1551 be used to reconstruct physical quantities like the particle's energy, momentum,  
 1552 or trajectory. Even the type of the particle can be distinguished by comparing  
 1553 the various ways that different species of stable particles interact with the subde-  
 1554 tectors. Reconstruction is the process which takes the electronic outputs of the  
 1555 detector and collects them into individual physics objects. The physics objects  
 1556 summarize the properties of particles produced by the collision or subsequent  
 1557 decays, either for individual isolated particles like leptons, or for a collection of  
 1558 the cascade of products produced in the decay of an energetic hadron, called a  
 1559 jet. These are the objects and quantities most often used in analysis to make  
 1560 measurements of SM processes or to search for new physics.

## 1561 7.1 TRACKS AND VERTICES

1562 As described in Section 6.3, charged particles that traverse the inner detector  
 1563 leave behind hits in the subdetectors. Each of these hits translates into a position  
 1564 measurement along the trajectory of that particle, with position resolutions de-  
 1565 pending on the subdetector that provided the measurement. Track reconstruc-  
 1566 tion uses these position measurements to cluster hits in consecutive layers of  
 1567 the detector into a trajectory consistent with a particle curving in a magnetic  
 1568 field [10, 11]. The number of hits in the inner detector for each event makes  
 1569 a combinatorial method completely infeasible: the algorithms that form tracks  
 1570 must be significantly more intelligent so that event reconstruction does not ex-  
 1571 haust computing resources.

1572 The first and primary algorithm employed in track reconstruction is called  
 1573 the inside-out method, which begins with the assumption that the track orig-  
 1574 inated from the interaction point. Its purpose is to identify primary particles,  
 1575 those which originate in the proton-proton collisions and with a lifetime long  
 1576 enough to reach the inner detector. Combinations of three space points are con-  
 1577 sidered from measurements in the Pixel detector and the first layer of the SCT,  
 1578 and form the seed for a track. The seed is then extrapolated into the SCT and  
 1579 hits in each layer are considered to be added to the track using a combinatorial  
 1580 Kalman filter [11]. After all of the SCT layers have been considered, tracks are  
 1581 filtered to reduce ambiguities from other nearby tracks or from combinatorial  
 1582 coincidences. Then the tracks are extended into the TRT in the same way. This  
 1583 algorithm is how the hits are chosen to be incorporated into a single track. Once  
 1584 the hits are collected, a fitting algorithm calculates the track parameters which

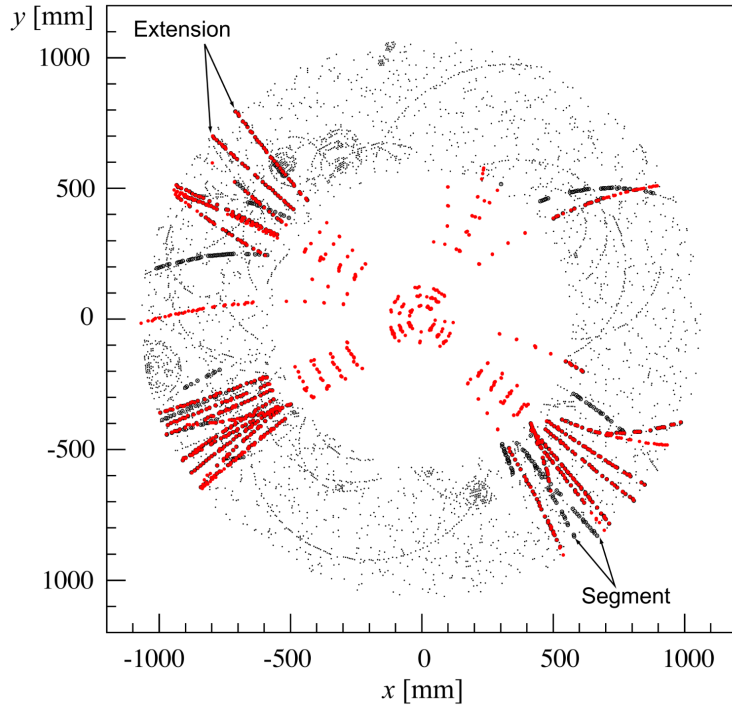


Figure 38: The  $x$  and  $y$  locations of the hits generated in a simulated  $t\bar{t}$  event in the inner detector. The hits which belong to tracks formed using the inside-out algorithm are highlighted in red, while the hits which belong to tracks formed using the outside-in algorithm are circled in black.

1585 best model the locations of the hits and their resolutions. Those parameters di-  
 1586 rectly determine the direction and momentum of the particle which produced  
 1587 the track.

1588 This inside-out algorithm is complemented by an outside-in algorithm, which  
 1589 is used to find tracks from secondary particles, those produced in the decays or  
 1590 interactions of the primary particles inside the detector. As the name indicates,  
 1591 the outside-in algorithm begins by seeding tracks in the outermost layers of the  
 1592 inner detector, in the TRT. The seed in this case is formed by a segment in the  
 1593 TRT, and the track is propagated backwards into the SCT before being refitted  
 1594 to use all the included points. Some tracks are found with TRT segments only,  
 1595 which can result from interactions with the detector following the SCT. Figure 38  
 1596 shows an example of the geometry of tracks formed by both algorithms, where  
 1597 the hits belonging to tracks found using the inside-out algorithm are highlighted  
 1598 in red, and the hits belonging to the tracks found using the outside-in algorithm  
 1599 are circled in black. The figure highlights the presence of a large number of  
 1600 both primary and secondary tracks in a single event, as well as the overall large  
 1601 number of hits present in the inner detector.

1602 The tracks resulting from these algorithms can be contaminated by nearby  
 1603 particles confusing the tracking algorithm in a high luminosity environment.  
 1604 For example, enough hits present in the inner detector can lead to fake tracks  
 1605 from combinations of hits from multiple individual tracks. Therefore, after the  
 1606 tracks are formed and fitted, additional quality requirements are imposed in

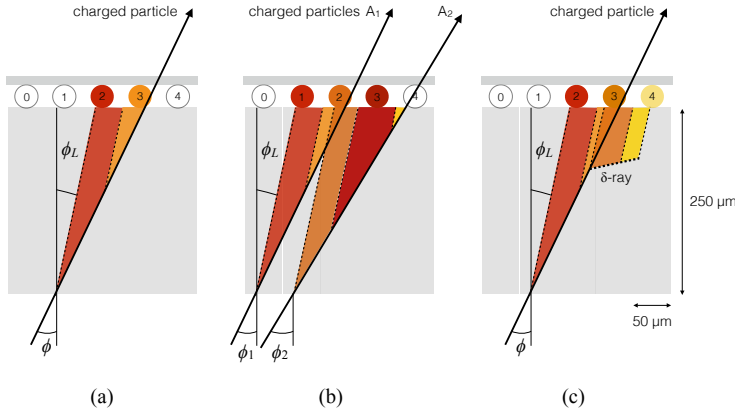


Figure 39: Examples of the clusters formed in a single layer of the pixel detector for (a) a single isolated particle, (b) two nearly-overlapping particles, and (c) a particle which emits a  $\delta$ -ray [12].

order to reduce such backgrounds. Most tracking applications require at least seven silicon hits, that is, seven hits between the Pixel detector and [SCT](#). Then the tracks are required to have at most two holes in the Pixel detector, where holes are non-existing but expected measurements in a layer of the subdetector. If the missing hit corresponds to an inactive module, however, it is not counted as a hole but instead as a hit for tracking as the lack of a measurement is expected in that case.

#### 7.1.1 PIXEL NEURAL NETWORK

The hits in the Pixel detector are not typically confined to a single pixel, but rather the charge is spread over several pixels per layer which are grouped together into clusters. The clustering of these pixels for isolated tracks is relatively straightforward, but complications can arise in the high track density environment where hits from multiple particles can overlap in a single cluster. Figure 39 shows examples of clusters generated by a single isolated particle, two nearly overlapping particles, and a particle which emits a  $\delta$ -ray. A  $\delta$ -ray is a secondary electron which is generated with enough energy to escape a significant distance away from the original particle and to generate additional ionization.

A series of neural-networks analyzes the shape of the clusters to determine how many particles produced the cluster and to find the positions of each of the particles within the cluster. These allow for an identification of clusters caused by more than one particle or by a particle that emits a  $\delta$ -ray. In a high-density tracking environment, the multiple position outputs can be used as the locations of individual hits to allow reconstruction of tracks which almost overlap and with a much better separation than is possible without the splitting of individual clusters.

## 1632 7.1.2 PIXEL DE/DX

1633 A hit in the Pixel detector corresponds to the voltage generated from ionization  
 1634 current rising above a threshold value that is tuned to consistently record the  
 1635 passing of MIPs. A larger amount of charge deposited results in a larger voltage,  
 1636 and a larger signal remains above the threshold for a longer period of time. The  
 1637 time over threshold (`ToT`) is read out of the Pixel detector, and can be used to  
 1638 provide a measurement of the charge deposited in each pixel. The charge mea-  
 1639 surements from each of the pixels included in a pixel cluster are summed to form  
 1640 one charge measurement per layer of the pixel detector. That charge measure-  
 1641 ment, combined with the angle of incidence of the track and the known sizes of  
 1642 each detector element, can be converted into a measurement of  $dE/dx$ , the ion-  
 1643 ization energy deposited per unit distance, measured in  $\text{MeVg}^{-1}\text{cm}^2$ . The IBL  
 1644 only has sixteen available values (4 bits) of `ToT` to readout, compared to the 256  
 1645 available values (8 bits) in the remaining pixel layers. To help alleviate this lack  
 1646 of range, the IBL also records if it is in overflow: when the ionization is sufficient  
 1647 to generate a `ToT` above the largest value that can be recorded in the 4 bits.

1648 The measurements across multiple layers are combined to form an average  
 1649 value of  $dE/dx$  for the track as a whole. To reduce the influence of the typical  
 1650 long Landau tails of the distribution of  $dE/dx$  deposits [7], the average is calcu-  
 1651 lated as a truncated mean. The value measured in the IBL is removed if it is in  
 1652 overflow, as the measured value is not reliable in that case. If a track has five  
 1653 measurements in the pixel detector, the two highest cluster values are removed.  
 1654 If a track has two, three, or four measurements in the pixel detector, only the  
 1655 single highest cluster value is removed. The remaining values are averaged to  
 1656 form the pixel  $dE/dx$ .

## 1657 7.1.3 VERTEX RECONSTRUCTION

1658 A vertex represents the intersection of multiple tracks and corresponds to the  
 1659 location of an interaction. If at least two charged particles result from the in-  
 1660 teraction, the intersection of their resulting tracks reveals its position with high  
 1661 precision. Vertices are divided into two groups, primary vertices which corre-  
 1662 spond to the actual proton-proton collisions, and secondary vertices which cor-  
 1663 respond to decays of short-lived particles or interactions with the detector. Pri-  
 1664 mary vertices are particularly important, as they can provide a precise location  
 1665 for the interaction which generated the observed particles. Understanding that  
 1666 location is crucial in understanding the geometry of the event.

1667 Primary vertices are reconstructed by iteratively identifying seeds from re-  
 1668 constructed tracks. Each track's extrapolated z position at the beamline forms a  
 1669 seed, and nearby tracks are fitted using that position as a point along their trajec-  
 1670 tory. The goodness of fit with that vertex is considered for each track, measured  
 1671 in  $\chi^2$ . The final position of the vertex is determined by a fit to all of the con-  
 1672 sidered tracks, where the contribution from each track is weighted according to  
 1673 the  $\chi^2$  compatibility with that vertex. Any tracks from this procedure that are  
 1674 displaced by more than  $7\sigma$  from that vertex are removed from the fit and used

1675 to seed a new vertex. This procedure is iterated until no additional vertices can  
 1676 be found.

1677 This procedure is typically performed twice. The first set of vertices is used  
 1678 to fit a profile for the beamspot, which indicates the position of the intersection  
 1679 of beams in that particular bunch crossing. The fitted beamspot then provides  
 1680 a constraint for the second attempt to locate primary vertices, where both the  
 1681 track fitting and seeding of vertices are required to be consistent with interac-  
 1682 tions occurring within the beamspot.

## 1683 7.2 ELECTRONS AND PHOTONS

1684 Electrons are measured as both a charged particle track and energy deposits in  
 1685 the electromagnetic calorimeter. Photons, on the other hand, leave energy de-  
 1686 posits in the electromagnetic calorimeter but do not produce a corresponding  
 1687 track. Because the electromagnetic interactions with the calorimeter of both  
 1688 photons and electrons produces more photons and electrons, the behavior in the  
 1689 calorimeter is very similar and there is significant overlap in the reconstruction  
 1690 techniques for each.

1691 The reconstruction of a photon or an electron in the calorimeter is based on  
 1692 clustering algorithms which identify groups of energy deposits [13]. For this  
 1693 purpose, the entire electromagnetic calorimeter is subdivided into a grid of 200  
 1694 by 256 towers in the  $\eta$  and  $\phi$  directions, respectively, where the individual grid  
 1695 units have a size of  $\Delta\eta = 0.025$  and  $\Delta\phi = 0.025$ . These towers correspond to  
 1696 individual cells in the middle, coarsest layer of the EM calorimeter, and in the  
 1697 remaining layers the cells are grouped together cover the same area in  $\eta - \phi$   
 1698 space. The clustering begins by finding seeds with a sliding-window algorithm  
 1699 based on the towers: a window of 3 by 5 towers is formed and translated until  
 1700 the sum of the energy within the window is maximized. If that energy is above  
 1701 2.5 GeV, then that region becomes a seed. The choice of 2.5 GeV was chosen to  
 1702 compromise between maximizing reconstruction efficiency while minimizing  
 1703 fake electron seeds from electronic noise or pileup. The seeds are rejected if the  
 1704 energy measured in the hadronic calorimeter behind the seed is large, as this  
 1705 typically indicates a hadron rather than an electron or photon.

1706 Next, the inner detector tracks within a cone of  $\Delta R = 0.3$  are compared to  
 1707 the location and energy of the seed. Tracks are matched to the cluster if the ex-  
 1708 trapolation of the track to the energy-weighted center in the middle layer of the  
 1709 EM calorimeter falls within  $\Delta\phi < 0.2$  in the direction of the curvature of the  
 1710 track or  $\Delta\phi < 0.05$  in the direction opposite of the curvature of the track. If the  
 1711 seed matches with a track that originated from a primary vertex, the combina-  
 1712 tion of track and electromagnetic cluster is reconstructed as an electron. If the  
 1713 seed matches with a track that did not originate from a primary vertex, then the  
 1714 electromagnetic cluster is reconstructed as a converted photon. And if there is  
 1715 no corresponding track in the inner detector, then the cluster is reconstructed  
 1716 as a photon.

1717 After classification, the final clustering of the energy in the EM calorimeter  
 1718 calorimeter is performed. The classification must be done first, as the expected

1719 size of the energy deposits in the calorimeter are different for electrons and pho-  
 1720 tons. In the barrel region, the final clusters for electrons are formed in rectangles  
 1721 of 3 towers in the  $\eta$ -direction and 7 towers in the  $\phi$ -direction. This asymmetric  
 1722 window accounts for the curving of the produced charged particles only in the  
 1723  $\phi$  direction. For photons, the size of the rectangle is 3 towers by 5 towers. In the  
 1724 endcap region, all object types are clustered in rectangles of 5 towers by 5 tow-  
 1725 ers, as the effect of the magnetic field curvature is less pronounced in this region.  
 1726 The sum of the energies in these clusters provide the final energy measurement  
 1727 for the electron or photon.

### 1728 7.2.1 PHOTON IDENTIFICATION

1729 The original requirement for constructing a photon cluster, a significant energy  
 1730 deposit in the electromagnetic calorimeter without a corresponding track or en-  
 1731 ergy deposits in the hadronic calorimeter, is already effective in identifying pho-  
 1732 tons. However, there is a significant background for prompt photon production  
 1733 from the decays of pions,  $\pi^0 \rightarrow \gamma\gamma$ . These can be identified using the shape of  
 1734 the cluster in the narrow  $\eta$  granularity in the first layer of the [EM](#) calorimeter.

### 1735 7.2.2 ELECTRON IDENTIFICATION

1736 Prompt electrons have a number of backgrounds, such as secondary electrons  
 1737 from hadron decays or misidentified hadronic jets, that can be rejected using ad-  
 1738 dditional information from the [EM](#) calorimeter and the inner detector. The most  
 1739 basic level of electron identification, referred to as Loose, makes requirements  
 1740 on the shower shapes in the high granularity first layer of the [EM](#) calorimeter  
 1741 as well as the quality of the inner detector track. It also requires a good match  
 1742 between the track and the calorimeter energy deposits and a small fraction of  
 1743 energy in the hadronic calorimeter behind the electromagnetic cluster. [ATLAS](#)  
 1744 defines several additional working points, including Medium and Tight, which  
 1745 provide progressively lower background rates for electrons by imposing addi-  
 1746 tionally strict requirements on the above variables as well as new requirements  
 1747 like the impact parameter of the inner detector track or the comparison of the  
 1748 cluster energy to the momentum in the inner detector.

## 1749 7.3 MUONS

1750 Muons produced in [ATLAS](#) first traverse the inner detector and leave behind a  
 1751 track as described in Section 7.1. The muon then passes through the calorimeter,  
 1752 leaving behind a small, characteristic amount of energy, and then passes through  
 1753 the muon spectrometer where it produces hits in the [MDTs](#) or [CSCs](#). Muon tracks  
 1754 are formed from local segments of hits in each layer of the [MDTs](#) or [CSCs](#), and  
 1755 then the final muon spectrometer track is formed by combining the two local  
 1756 segments. When a track is reconstructed in both the inner detector and the muon  
 1757 spectrometer, they are combined to form a combined muon.

1758 In a few regions of the detector, a muon may fail to leave behind both a com-  
 1759 plete inner detector and muon system track. For a very small fraction of the  
 1760 acceptance of the muon system, there is only one layer of muon chambers and a  
 1761 global muon system track is not formed. In this case, as long as the track in the  
 1762 inner detector exists and geometrically matches to a segment, a segment-tagged  
 1763 muon is formed using momentum measurements from the inner detector. In  
 1764 the region where the muon system has coverage but the inner detector does not,  
 1765  $2.5 < |\eta| < 2.7$ , a stand-alone muon is formed which uses only information  
 1766 from the muon system. And for muons produced within one of the few holes in  
 1767 the muon system, including  $|\eta| < 0.1$ , the characteristic energy deposits in the  
 1768 calorimeter can be used to tag an inner detector track as a calo-tag muon. These  
 1769 additional categories are used to achieve high efficiency over a larger range of  
 1770 acceptance, but the combined muons are the most reliable.

### 1771 7.3.1 MUON IDENTIFICATION

1772 The various types of muons are incorporated into three working points: Loose,  
 1773 Medium, and Tight, which reflect the increasing muon purity for each of the  
 1774 selections definitions. Tight muons include only combined muons with a good  
 1775 track fit quality and momentum resolution and at least two hits in a precision  
 1776 muon system layer. Medium muons include those in tight as well as combined  
 1777 muons with one precision hit and one precision hole, where hole is defined in  
 1778 the same way as in Section 7.1. The medium working point also includes stand-  
 1779 alone muons with  $|\eta| > 2.5$  and at least two hits in precision layers. And finally  
 1780 the loose working point includes both medium and tight muons, but additional  
 1781 includes segment-tagged and calo-tagged muons in the region  $|\eta| < 0.1$ .

## 1782 7.4 JETS

1783 A jet does not directly correspond to a physical particle, unlike all of the recon-  
 1784 structed objects described above, but instead tries to capture the conical cascade  
 1785 of particles produced in the hadronization of a quark or gluon from the proton-  
 1786 proton collision. The hadronization process creates a very large number of col-  
 1787 limated particles, with a high enough density that individually reconstructing all  
 1788 of the produced particles in the calorimeter is not possible within ATLAS. How-  
 1789 ever most analyses are interested only in the kinematics of the particle which  
 1790 produced the cascade, rather than the individual products. Therefore, jets are  
 1791 a useful tool to measure the combined energy and direction of the ensemble of  
 1792 products and thus represents the kinematics of the original. Jet algorithms are  
 1793 very generic and can be used to group together a number of types of objects to  
 1794 form aggregate representations. For example, truth particles in simulation can  
 1795 be grouped in truth jets, or tracks from the inner detector can be grouped to-  
 1796 gether to form track jets. This section, however, will focus on calorimeter jets  
 1797 which take topoclusters of energy deposits in the calorimeter as inputs and pro-  
 1798 duce a combined object which represents the energy measured by the calorime-  
 1799 ter and the location where it was deposited.

## 1800 74.1 TOPOLOGICAL CLUSTERING

1801 Hadrons often deposit their energy into multiple individual cells in both the elec-  
 1802 tromagnetic and hadronic calorimeters. The purpose of topological clustering is  
 1803 to group cells in all three dimensions into clusters that represent a single energy  
 1804 deposit. The procedure must be robust enough to reject noise fluctuations in  
 1805 the cell energy measurements that can come from both electronic noise and ad-  
 1806 ditional low energy particles produced in pileup activity. The background level  
 1807 of calorimeter noise is called  $\sigma_{\text{noise}}$ , and is an important component of the topo-  
 1808 logical clustering.

1809 The topological clusters are formed in a three step process called the 4-2-0  
 1810 threshold scheme, which uses three energy thresholds to build up a cluster from  
 1811 cells. First, any cells with a measured energy above  $4\sigma_{\text{noise}}$  are identified as seed  
 1812 cells. The cells adjacent to the seed cells with a measured energy above  $2\sigma_{\text{noise}}$  are  
 1813 called secondary cells. All of the cells which are adjacent to a secondary cell  
 1814 with  $E_{\text{cell}} > 2\sigma_{\text{noise}}$  are also labelled secondary cells. Tertiary cells are those  
 1815 immediately adjacent to a seed or secondary cell with a measured energy above  
 1816 zero. Adjacency in this sense is defined in three dimensions, cells are adjacent if  
 1817 they are neighbors within a layer but also if they have the same  $\eta - \phi$  coordinates  
 1818 but are in adjacent layers or even in an adjacent layer in another calorimeter.

1819 From these definitions, clusters are built by resolving the seeds in order of  
 1820 significance, the ratio  $E_{\text{cell}}/\sigma_{\text{noise}}$ . All adjacent secondary cells to the highest  
 1821 significance seed are added to that seed's topocluster, and any of those cells which  
 1822 would also have qualified as seeds are removed from the list of seeds. Once all  
 1823 of the secondary cells have been added, the tertiary cells are then added to that  
 1824 cluster as well. This procedure is then iterated until no seeds remain, forming  
 1825 the first round of topoclusters.

1826 It is also useful to split topoclusters into multiples if local maxima are present  
 1827 within the topocluster, as clusters produced by multiple nearby particles can  
 1828 merge. The splitting process begins by finding local maxima cells in the middle  
 1829 layer of the calorimeters with a minimum energy of 500 MeV and at least four  
 1830 neighboring secondary cells. These requirements reduce the likelihood to split  
 1831 a cluster due to random fluctuations, as the middle layers provide the most reli-  
 1832 able energy measurements. Cells between two local maxima can then be shared  
 1833 between two clusters to account for overlapping contributions from two parti-  
 1834 cles. The energy sharing is weighted by the energy of each cluster as well as the  
 1835 distance of the cell to the centroid of that cluster.

1836 The energies of all the cells in the cluster are then summed together to form  
 1837 the energy of that cluster. The energy needs to be corrected for the various losses  
 1838 expected in the calorimeter, as described in Section 6.4. The simplest correction,  
 1839 scaling the measured energy by the sampling fraction, brings the cluster energies  
 1840 to the EM scale. It is called the EM scale because it accurately describes the energy  
 1841 of electromagnetic showers.

1842 Another scale is defined to improve accuracy for hadronic processes, the local  
 1843 cluster weighted (LCW) scale, that helps to correct for the expected variations in  
 1844 hadronic energy deposits. The LCW correction first determines if the shower is

hadronic or electromagnetic, based on the depth of the shower and the cluster energy density. For hadronic showers, the energy is corrected for calorimeter non-compensation, an effect which reduces the measured energy of hadronic showers because some of the energy goes into invisible processes like the break up of nuclei. All clusters are then corrected for energy that may be deposited in uninstrumented regions in that cluster's location in the calorimeter, and they are also corrected with an estimate of how much energy falls outside the extent of the cluster based on its shape and the deposit type.

## 7.4.2 JET ALGORITHMS

Using the topological clusters as inputs, a jet algorithm groups them together into a collection of adjacent energy deposits that is intended to correspond to a single process. Jet algorithms need a few key characteristics to be usable for physics analysis. First, the jets produced by the algorithm should have little dependence on the addition of soft particles to the event (infrared safety), as a negligible addition of energy should not significantly modify the event topology. Similarly, the jets produced by the algorithm should also not significantly depend on mostly collinear splitting of an input particle (collinear safety); that is, a single quark splitting into two nearly parallel quarks should not change the resulting jets, which are intended to capture only the properties of the aggregate and not those of individual particles. And finally the algorithm needs to be sufficiently simple and fast to be used for the large rate of collected proton-proton collisions on [ATLAS](#).

The most commonly used algorithm on [ATLAS](#) that satisfies these requirements is called the anti- $k_t$  algorithm, and is discussed in further detail in Reference [14]. The anti- $k_t$ , in brief, relies on iteratively combining the input objects that are closest together, where closest is defined by a particular distance metric,  $d_{ij}$ . The combinations stop when the closest remaining object is the beam itself, where the distance to the beam is called  $d_{i,B}$ . An entire class of algorithms follows this procedure with the following distance metrics

$$d_{i,j} = \min(k_{ti}^{2p}, k_{tj}^{2p}) \frac{\Delta_{ij}^2}{R^2} \quad (13)$$

$$d_{i,B} = k_{ti}^{2p} \quad (14)$$

where  $\Delta_{ij} = (y_i - y_j)^2 + (\phi_i - \phi_j)^2$ ,  $k_{ti}$  is the transverse momentum of the object,  $y$  is the rapidity, and  $p$  is a parameter of the algorithm. Anti- $k_t$  is the particular case where  $p = -1$ , and is a choice that results in an algorithm that is both infrared and collinear safe.

The algorithm is repeated until there are no input objects remaining, which results in a series of jets. Each jet has a complete four momentum from the combination of its input clusters. The jet energies then need to be calibrated to attempt to match the energy of the object which produced the jet.

## 1882 74.3 JET ENERGY SCALE

1883 Though the [LCW](#) scheme attempts to correct the topoclusters to reflect the true  
 1884 deposited energy, the correction does not fully account for energy lost within  
 1885 the calorimeters. Because of these effects, the original reconstructed jet energy  
 1886 does not reflect the true energy of the particle which initiated the jet. Therefore  
 1887 it is necessary to additionally correct the reconstructed jet itself, in addition to  
 1888 the corrections on the inputs. This correction is referred to as the [JES](#), which  
 1889 combines several individual steps of calibration.

1890 The first calibration step corrections the direction of the jet to ensure that it  
 1891 points back to the primary vertex. Next, the energy of the jet is corrected for  
 1892 pileup by subtracting the expected contribution from pileup (measured in simu-  
 1893 lation) based on the momentum,  $\eta$ , and area of the jet as well as the number of  
 1894 reconstructed vertices and expected number of interactions per crossing. The  
 1895 largest single correction is the absolute  $\eta$  and [JES](#) correction, where the jet energy  
 1896 and pseudorapidity is corrected to attempt to match the energy and pseudorapid-  
 1897 ity of the parton which produced it. This correction is measured in simulation  
 1898 by comparing the reconstructed jet energies to the energy of the truth particle  
 1899 which produced it. However the simulation is not relied on alone to estimate  
 1900 this correction, and an additional step applies an additional energy correction  
 1901 based on in-situ measurements in data. These corrections come from various  
 1902 techniques which measure jet energies indirectly by balancing them with other,  
 1903 well-measured objects. In the central region ( $|\eta| < 1.2$ ), jets are balanced against  
 1904 photons and the leptonic decays of Z bosons and high momentum jets ( $p_T > 210$   
 1905 GeV) are also balanced against multiple smaller jets in multijet events. Jets at  
 1906 larger pseudorapidities, above  $|\eta| = 1.2$ , are calibrated by balancing with lower  
 1907 pseudorapidity jets.

1908 These steps introduce a number of systematic uncertainties, referred to as  
 1909 the [JES](#) uncertainty. The largest of these comes from the in-situ measurements,  
 1910 which are statistically limited in measuring high momentum and high pseudora-  
 1911 pidity jets. The total, fractional [JES](#) uncertainty is shown as a function of  $p_T$  in  
 1912 Figure 40. The uncertainty falls to a minimum value of just over 1.0% around a  
 1913 few hundred GeV, and rises again at high momentum because of the difficulty of  
 1914 measuring jet balance in data above 2-3 TeV. The uncertainty is also minimized  
 1915 at low  $|\eta|$ , and grows at large  $|\eta|$  again where making in-situ measurements is  
 1916 difficult. This technique does not actually provide a measurement of the uncer-  
 1917 tainty for the highest energy jets, above 3 TeV, because there are not enough  
 1918 measured data events to provide them. An alternative method for deriving the  
 1919 [JES](#) and [JES](#) uncertainty that can be used even for very high  $p_T$  jets will be dis-  
 1920 cussed in Chapter 9.

## 1921 7.5 MISSING TRANSVERSE ENERGY

1922 Among [SM](#) particles, only the neutrino cannot be directly measured in the [ATLAS](#)  
 1923 detector. Because the neutrino carries neither electric nor color charge, it is very  
 1924 unlikely to interact with the tracking detectors or the calorimeters, and instead

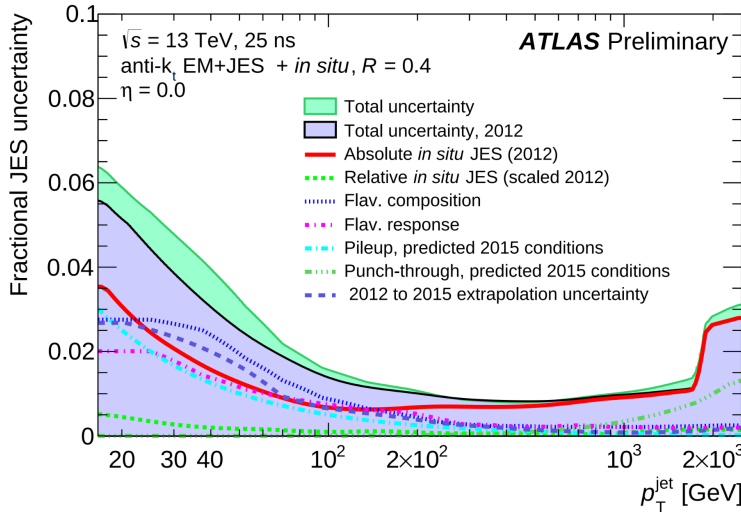


Figure 40: The total, fractional JES uncertainties estimated for 2015 data as a function of jet  $p_T$ .

passes through the detector completely unobserved. Some particles which have been conjectured to exist, like the LSP in many SUSY models, would also have the same behavior. Therefore, it is important for ATLAS to provide some way to assess the momentum carried away by a neutral, colorless particle. This can be accomplished through a measurement of missing energy in the transverse direction, or  $E_T^{\text{miss}}$ , which quantifies the momentum imbalance of the observed particles. From the conservation of momentum and the lack of the initial momentum in the transverse plane in the proton-proton collisions, any imbalance of momentum can be inferred to be carried away by an unmeasured particle.

$E_T^{\text{miss}}$  is more precisely defined as the magnitude of the vector sum of the  $(p_x, p_y)$  components of each observed object's momentum. The definition is simple, but there can be significant complexity in defining the inputs. As of Run 2, ATLAS uses a common algorithmic approach to carefully calculate missing energy, but each analysis is free to define its own inputs. For the analysis discussed throughout this thesis, the missing energy inputs consist of the electrons, photons, muons, and jets discussed in the previous sections, in addition to a track-based soft term.

To produce the most precise measurement of  $E_T^{\text{miss}}$ , it is important to use the best representation of the momentum of each of the input objects, which can often be reconstructed as multiple different types in a single event. For example, an electron can be reconstructed separately as an electron (Section 7.2) and a jet (Section 7.4), but the electron representation has the highest precision for reconstructing the true electron momentum. To ensure no duplications in the  $E_T^{\text{miss}}$  definition, the inputs are collectively considered for overlap removal. Only the most precise object type is kept for objects that fall within a cone of  $\Delta R < 0.2$  for pairs of electrons and jets and a cone of  $\Delta R < 0.4$  for other pair types.

The fully reconstructed objects do not include all of the energy within the events, as some clusters do not enter into a jet and some tracks are not classified as electrons or muons. These momentum carried by these objects is accounted

1954 for in a soft-term, which tallies all of the energy carried by the particles too soft  
1955 to form separate objects. The track soft term uses only tracking information to  
1956 estimate the contribution of soft objects, and does so by vectorially summing the  
1957 momentum of all well-reconstructed tracks with momentum above 400 MeV.

1958 All of these contributions together give a single  $E_T^{\text{miss}}$  value for a given event.  
1959 The direction of that missing energy is taken as opposite the vector sum of all the  
1960 constituents, to correspond to the momentum an invisible particle would have to  
1961 have to make the event balanced. Depending on the context, this missing energy  
1962 can be considered the energy of a neutrino or an LSP, with a large missing energy  
1963 being a common signal criteria for searches for new physics.

1964

## PART IV

1965

### CALORIMETER RESPONSE

1966

You can put some informational part preamble text here.



1967

1968 RESPONSE MEASUREMENT WITH SINGLE HADRONS

---

1969 As discussed in Section 7.4, colored particles produced in collisions hadronize  
1970 into jets of multiple hadrons. One approach to understanding jet energy mea-  
1971 surements in the ATLAS calorimeters is to evaluate the calorimeter response to  
1972 those individual hadrons; measurements of individual hadrons can be used to  
1973 build up an understanding of the jets that they form. The redundancy of the  
1974 momentum provided by the tracking system and the energy provided by the  
1975 calorimeter provides an opportunity to study calorimeter response using real  
1976 collisions, as described further in Section 8.2.

1977 Calorimeter response includes a number of physical effects that can be ex-  
1978 tracted to provide insight into many aspects of jet modeling. First, many charged  
1979 hadrons interact with the material of the detector prior to reaching the calorime-  
1980 ters and thus do not deposit any energy. Comparing this effect in data and simu-  
1981 lation is a powerful tool in validating the interactions of particles with the mate-  
1982 rial of the detector and the model of the detector geometry in simulation, see Sec-  
1983 tion 8.2.2. The particles which do reach the calorimeter deposit their energy into  
1984 several adjacent cells, which are then clustered together. The energy of the clus-  
1985 ter is then the total energy deposited by that particle. Comparing the response of  
1986 hadrons in data to that of simulated hadrons provides a direct evaluation of the  
1987 showering of hadronic particles and the energy deposited by particles in matter  
1988 (Section 8.2.4).

1989 The above studies all use an inclusive selection of charged particles, which are  
1990 comprised predominantly of pions, kaons, and (anti)protons. It is also possible to  
1991 measure the response to various identified particle types separately to evaluate  
1992 the simulated interactions of each particle, particularly at low energies where  
1993 differences between species are very relevant. Pions and (anti)protons can be  
1994 identified through decays of long-lived particles, in particular  $\Lambda$ ,  $\bar{\Lambda}$ , and  $K_S^0$ , and  
1995 then used to measure response as described above. This is discussed in detail in  
1996 Section 8.3.

1997 The results in this chapter use data collected at 7 and 8 TeV collected in 2010  
1998 and 2012, respectively. Both are included as the calorimeter was repaired and  
1999 recalibrated between those two data-taking periods. Both sets of data are com-  
2000 pared to an updated simulation that includes new physics models provided by  
2001 Geant4 [15] and improvements in the detector description [16, 17]. The present  
2002 results are published in European Physical Journal C (EPJC) [18] and can be com-  
2003 pared to a similar measurement performed in 2009 and 2010 [19], which used  
2004 the previous version of the simulation framework [20].

2005 8.1 DATASET AND SIMULATION

2006 8.1.1 DATA SAMPLES

2007 The two datasets used in this chapter are taken from dedicated low-pileup runs  
 2008 where the fraction of events with multiple interactions was negligible. These  
 2009 datasets are used rather than those containing full-pileup events to facilitate mea-  
 2010 surement of isolated hadrons. The 2012 dataset at  $\sqrt{s} = 8$  TeV contains 8 mil-  
 2011 lion events and corresponds to an integrated luminosity of  $0.1 \text{ nb}^{-1}$ . The 2010  
 2012 dataset at  $\sqrt{s} = 7$  TeV contains 3 million events and corresponds to an inte-  
 2013 grated luminosity of  $3.2 \text{ nb}^{-1}$ . The latter dataset was also used for the 2010 re-  
 2014 sults [19], but it has since been reanalyzed with an updated reconstruction in-  
 2015 cluding the final, best understanding of the detector description for the material  
 2016 and alignment from Run 1.

2017 8.1.2 SIMULATED SAMPLES

2018 The two datasets above are compared to simulated single-, double-, and non-  
 2019 diffractive events generated with Pythia8 [21] using the A2 configuration of  
 2020 hadronization [22] and the MSTW 2008 parton-distribution function set [23,  
 2021 24]. The admixture of the single-, double-, and non-diffractive events uses the  
 2022 default relative contributions from Pythia8. The conditions and energies for  
 2023 the two simulations are chosen so that they match those of the corresponding  
 2024 dataset.

2025 To evaluate the interaction of hadrons with detector material, the simulation  
 2026 uses two different collections of hadronic physics models, called physics lists, in  
 2027 Geant4 9.4 [25]. The first, QGSP\_BERT, combines the Bertini intra-nuclear  
 2028 cascade [26–28] below 9.9 GeV, a parametrized proton inelastic model from 9.5  
 2029 to 25 GeV [29], and a quark-gluon string model above 12 GeV [30–34]. The  
 2030 second, FTFP\_BERT, combines the Bertini intra-nuclear cascade [26–28] below  
 2031 5 GeV and the Fritiof model [35–38] above 4 GeV. In either list, Geant4 en-  
 2032 forces a smooth transition between models where multiple models overlap.

2033 8.1.3 EVENT SELECTION

2034 The event selection for this study is minimal, as the only requirement is selecting  
 2035 good-quality events with an isolated track. Such events are triggered by requir-  
 2036 ing at least two hits in the minimum-bias trigger scintillators. After trigger, each  
 2037 event is required to have exactly one reconstructed vertex, and that vertex is re-  
 2038 quired to have four or more associated tracks.

2039 The particles which are selected for the response measurements are first iden-  
 2040 tified as tracks in the inner detector. The tracks are required to have at least 500  
 2041 MeV of transverse momentum. To ensure a reliable momentum measurement,  
 2042 these tracks are required to have at least one hit in the pixel detector, six hits in  
 2043 the SCT, and small longitudinal and transverse impact parameters with respect  
 2044 to the primary vertex [19]. For the majority of the measurements in this chapter,

2045 the track is additionally required to have 20 hits in the TRT, which significantly  
 2046 reduces the contribution from tracks which undergo nuclear interactions. This  
 2047 requirement and its effect is discussed in more detail in Section 8.2.5. In addition,  
 2048 tracks are rejected if there is any other reconstructed track which extrapolates  
 2049 to the calorimeter within a cone of  $\Delta R = \sqrt{(\Delta\phi)^2 + (\Delta\eta)^2} < 0.4$ . This require-  
 2050 ment guarantees that the contamination of energy from nearby charged particles  
 2051 is negligible [19].

## 2052 8.2 INCLUSIVE HADRON RESPONSE

2053 The calorimeter response is more precisely defined as the ratio of the measured  
 2054 calorimeter energy to the true energy carried by the particle, although this true  
 2055 energy is unknown. For charged particles, however, the inner detector provides  
 2056 a very precise measurement of momentum (with uncertainty less than 1%) that  
 2057 can be used as a proxy for true energy. The ratio of the energy deposited by  
 2058 the charged particle in the calorimeter,  $E$ , to its momentum measured in the  
 2059 inner detector  $p$ , forms the calorimeter response measure called  $E/p$ . Though  
 2060 the distribution of  $E/p$  contains a number of physical features, this study focuses  
 2061 on the trends in two aggregated quantities:  $\langle E/p \rangle$ , the average of  $E/p$  for the  
 2062 selected tracks, and the zero fraction, the fraction of tracks with no associated  
 2063 energy in the calorimeter for those tracks.

2064 The calorimeter energy assigned to a track is defined using clusters. The clus-  
 2065 ters are formed using a 4–2–0 algorithm [39] that begins with seeds requiring  
 2066 at least 4 times the average calorimeter cell noise. The neighboring cells with  
 2067 at least twice that noise threshold are then added to the cluster, and all bound-  
 2068 ing cells are then added with no requirement. This algorithm minimizes noise  
 2069 contributions through its seeding process, and including the bounding cells im-  
 2070 proves the energy resolution [40]. The clusters are associated to a given track  
 2071 if they fall within a cone of  $\Delta R = 0.2$  of the extrapolated position of the track,  
 2072 which includes about 90% of the energy on average [19]. This construction is  
 2073 illustrated in Figure 41.

### 2074 8.2.1 E/P DISTRIBUTION

2075 The  $E/p$  distributions measured in both data and simulation are shown in Fig-  
 2076 ure 42 for two example bins of track momentum and for tracks in the central  
 2077 region of the detector. These distributions show several important features of  
 2078 the  $E/p$  observable. The large content in the bin at  $E = 0$  comes from tracks that  
 2079 have no associated cluster, which occurs due to interactions with detector mate-  
 2080 rial prior to reaching the calorimeter or the energy deposit being insufficiently  
 2081 large to generate a seed, and are discussed in Section 8.2.2. The small negative  
 2082 tail also comes from tracks that do not deposit any energy in the calorimeter but  
 2083 are randomly associated to a cluster with an energy below the noise threshold.  
 2084 The long positive tail above 1.0 comes from the contribution of neutral parti-  
 2085 cles. Nearby neutral particles deposit (sometimes large) additional energy in the  
 2086 calorimeter but do not produce tracks in the inner detector, so they cannot be

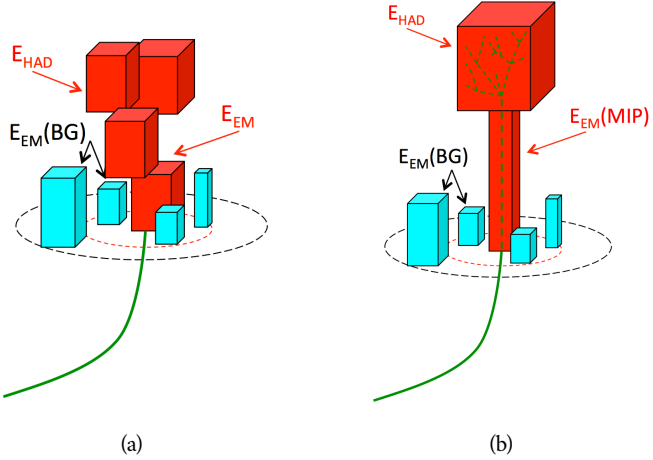


Figure 41: An illustration (a) of the  $E/p$  variable used throughout this paper. The red energy deposits come from the charged particle targeted for measurement, while the blue energy deposits are from nearby neutral particles and must be subtracted. The same diagram (b) for the neutral-background selection, described in Section 8.2.3.

2087 rejected by the track isolation requirement. Additionally the peak and mean of  
 2088 the distribution falls below 1.0 because of the loss of energy not found within  
 2089 the cone as well as the non-compensation of the calorimeter.

2090 The data and simulation share the same features, but the high and low tails  
 2091 are significantly different. The simulated events tend to overestimate the con-  
 2092 tribution of neutral particles to the long tail, an effect which can be isolated and  
 2093 removed as discussed in Section 8.2.3. Additionally, the simulated clusters have  
 2094 less noise on average, although this is a small effect on the overall response.

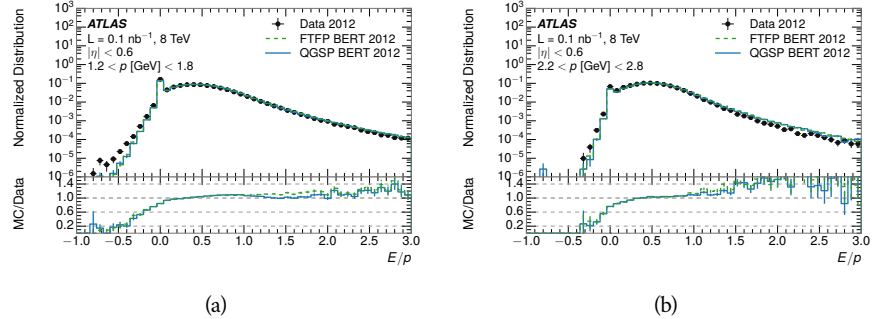


Figure 42: The  $E/p$  distribution and ratio of simulation to data for isolated tracks with  
 (a)  $|\eta| < 0.6$  and  $1.2 < p/\text{GeV} < 1.8$  and (b)  $|\eta| < 0.6$  and  $2.2 < p/\text{GeV} < 2.8$ .

### 2095 8.2.2 ZERO FRACTION

2096 The fraction of particles with no associated clusters, or similarly those with  $E \leq$   
 2097 0, reflects the modeling of both the detector geometry and hadronic interactions.

2098 The zero fraction is expected to rise as the amount of material a particle traverses  
 2099 increases, while it is expected to decrease as the particle energy increases. This  
 2100 dependence can be seen in Figure 43, where the zero fraction in data and simulation  
 2101 is shown as a function of momentum and the amount of material measured  
 2102 in interaction lengths. The trends are similar between 2010 and 2012 and for  
 2103 positively and negatively charged particles. The zero fraction decreases with  
 2104 energy as expected. The absolute discrepancy in zero fraction decreases with  
 2105 momentum from 5% to less than 1%, but this becomes more pronounced in the  
 2106 ratio as the zero fraction shrinks quickly with increasing momentum. There is  
 2107 a small constant difference between the data and simulation in both interaction  
 2108 models that becomes more pronounced. The amount of material in the detector  
 2109 increases with  $\eta$ , which is used to obtain results for interaction lengths ranging  
 2110 between 0.1 and 0.65  $\lambda$ . As the data and simulation have significant disagree-  
 2111 ment in the zero fraction over a number of interaction lengths, the difference  
 2112 must be primarily from the modeling of hadronic interactions with detector ma-  
 2113 terial and not just the detector geometry. Although two different hadronic in-  
 2114 teraction models are shown in the figure, they have very similar discrepancies to  
 2115 data because both use the same description (the BERT model) at low momentum.

### 2116 8.2.3 NEUTRAL BACKGROUND SUBTRACTION

2117 The isolation requirement on hadrons is only effective in removing an energy  
 2118 contribution from nearby charged particles. Nearby neutral particles, predomi-  
 2119 nantly photons from  $\pi^0$  decays, also add their energy to the calorimeter clusters,  
 2120 but mostly in the electromagnetic calorimeter. It is possible to measure this con-  
 2121 tribution, on average, using late-showering hadrons that minimally ionize in the  
 2122 electromagnetic calorimeter. Such particles are selected by requiring that they  
 2123 deposit less than 1.1 GeV in the EM calorimeter within a cone of  $\Delta R < 0.1$   
 2124 around the track. To ensure that these particles are well measured, they are addi-  
 2125 tionally required to deposit between 40% and 90% of their energy in the hadronic  
 2126 calorimeter within the same cone.

2127 These particles provide a clean sample to measure the nearby neutral back-  
 2128 ground because they do not deposit energy in the area immediately surrounding  
 2129 them in the EM calorimeter, as shown in Figure 41. So, the energy deposits in the  
 2130 region  $0.1 < \Delta R < 0.2$  can be attributed to neutral particles alone. To estimate  
 2131 the contribution to the whole cone considered for the response measurement,  
 2132 that energy is scaled by a geometric factor of  $4/3$ . This quantity,  $\langle E/p \rangle_{BG}$ , mea-  
 2133 sured in aggregate over a number of particles, gives the contribution to  $\langle E/p \rangle$   
 2134 from neutral particles in the EM calorimeter. Similar techniques were used in  
 2135 the individual layers of the hadronic calorimeters to show that the background  
 2136 from neutrals is negligible in those layers [19].

2137 The distribution of this background estimate is shown in Figure 44 for data  
 2138 and simulation with the two different physics lists. The contribution from neu-  
 2139 tral particles falls from 0.1 at low momentum to around 0.03 for particles above  
 2140 7 GeV. Although the simulation captures the overall trend, it significantly over-  
 2141 estimates the neutral contribution for tracks with momentum between 2 and 8

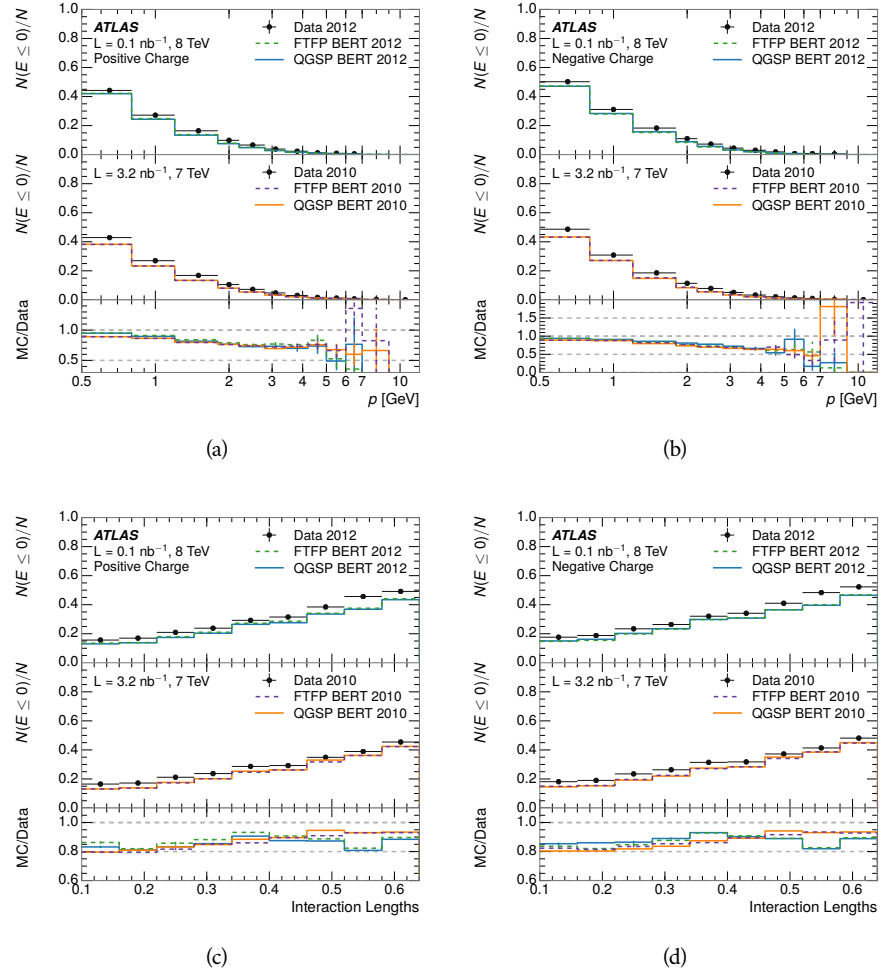


Figure 43: The fraction of tracks as a function (a, b) of momentum, (c, d) of interaction lengths with  $E \leq 0$  for tracks with positive (on the left) and negative (on the right) charge.

2142 GeV. This effect was also seen in the tails of the  $E/p$  distributions in Figure 42.  
 2143 This difference is likely due to modeling of coherent neutral particle radiation  
 2144 in Pythia8 that overestimates the production of  $\pi^0$  near the production of the  
 2145 charged particles. The discrepancy does not depend on  $\eta$  and thus is unlikely to  
 2146 be a mismodeling of the detector. This difference can be subtracted to form a  
 2147 corrected average  $E/p$ , as in Section 8.2.4.

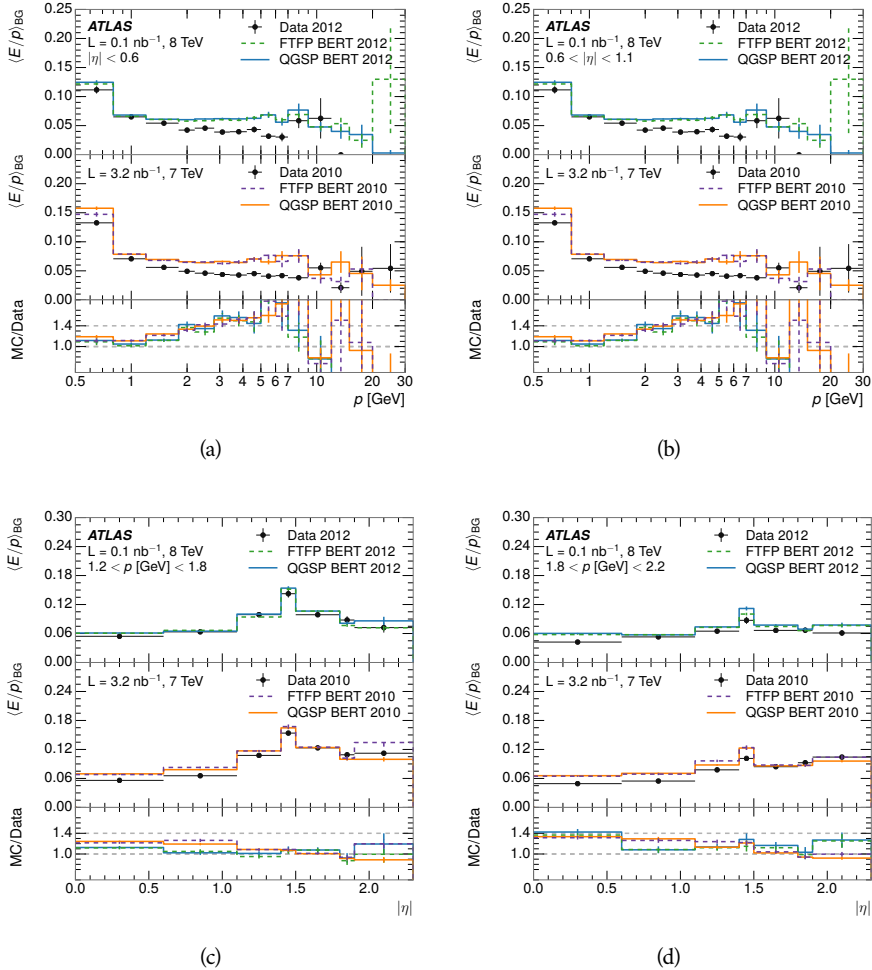


Figure 44:  $\langle E/p \rangle_{BG}$  as a function of the track momentum for tracks with (a)  $|\eta| < 0.6$ ,  
 (b)  $0.6 < |\eta| < 1.1$ , and as a function of the track pseudorapidity for tracks  
 with (c)  $1.2 < p/\text{GeV} < 1.8$ , (d)  $1.8 < p/\text{GeV} < 2.2$ .

#### 2148 8.2.4 CORRECTED RESPONSE

2149 Figure 45 shows  $\langle E/p \rangle_{COR}$  as a function of momentum for several bins of pseudo-  
 2150 rapidity. This corrected  $\langle E/p \rangle_{COR} \equiv \langle E/p \rangle - \langle E/p \rangle_{BG}$  measures the average  
 2151 calorimeter response without the contamination of neutral particles. It is the  
 2152 most direct measurement of calorimeter response in that it is the energy mea-  
 2153 sured for fully isolated hadrons. The correction is performed separately in data  
 2154 and simulation, so that the mismodeling of the neutral background in simulation

is removed from the comparison of response. The simulation overestimates the response at low momentum by about 5%, an effect that can be mostly attributed to the underestimation of the zero fraction mentioned previously. For  $|\eta| < 0.6$ , the data-simulation agreement has a larger discrepancy by about 5% for 2010 than 2012, although this is not reproduced in at higher pseudorapidity.

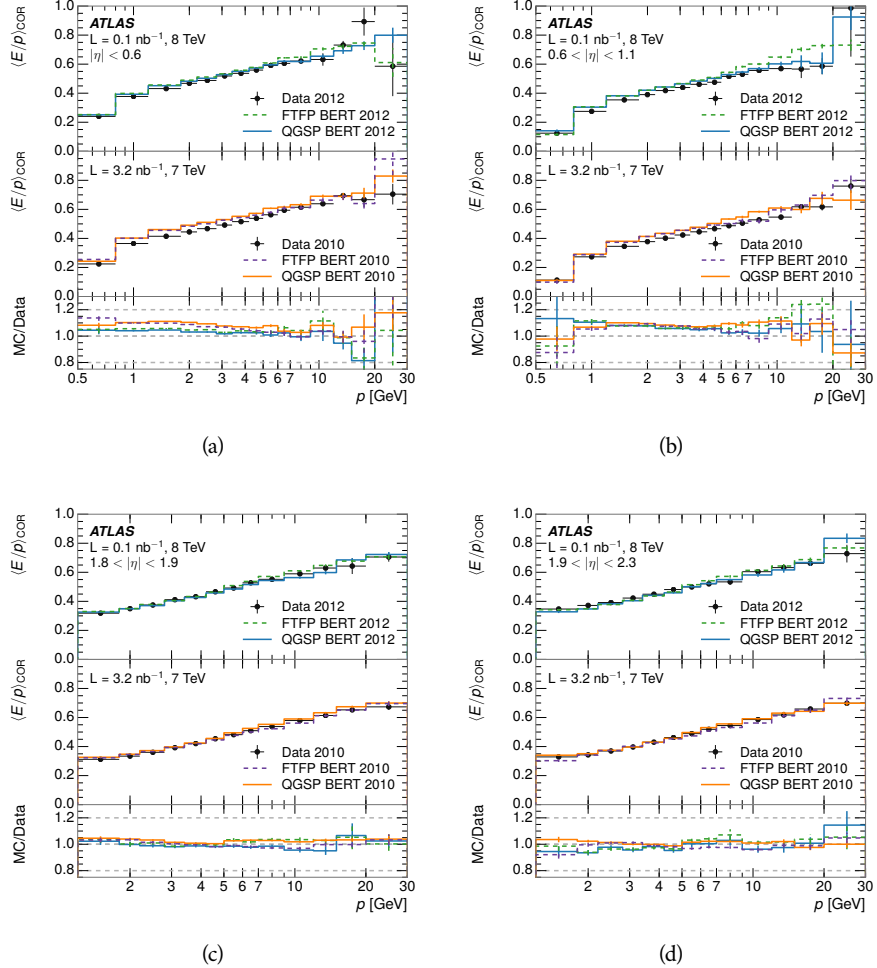


Figure 45:  $\langle E/p \rangle_{\text{COR}}$  as a function of track momentum, for tracks with (a)  $|\eta| < 0.6$ , (b)  $0.6 < |\eta| < 1.1$ , (c)  $1.8 < |\eta| < 1.9$ , and (d)  $1.9 < |\eta| < 2.3$ .

The response measurement above used topological clustering at the EM scale, that is clusters were formed to measure energy but no corrections were applied to correct for expected effects like energy lost outside of the cluster or in uninstrumented material. It is also interesting to measure  $\langle E/p \rangle_{\text{COR}}$  using LCW energies, which accounts for those effects by calibrating the energy based on the properties of the cluster such as energy density and depth in the calorimeter. Figure 46 shows these distributions for tracks with zero or more clusters and separately for tracks with one or more clusters. The calibration moves the mean value of  $\langle E/p \rangle_{\text{COR}}$  significantly closer to 1.0 as desired. The agreement between data and simulation improves noticeably when at least one cluster is required, as this removes the contribution from the mismodeling of the zero fraction. The

good agreement in that case again demonstrates that the difference in  $\langle E/p \rangle_{\text{COR}}$  between data and simulation is caused predominantly by the difference in zero fraction.

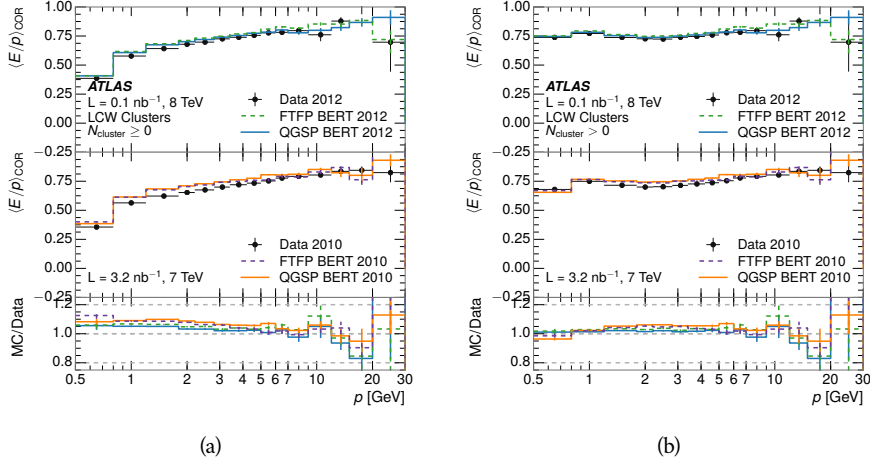


Figure 46:  $\langle E/p \rangle_{\text{COR}}$  calculated using LCW-calibrated topological clusters as a function of track momentum for tracks with (a) zero or more associated topological clusters or (b) one or more associated topological clusters.

## 8.2.5 ADDITIONAL STUDIES

As has been seen in several measurements in previous sections, the simulation does not correctly model the chance of a low momentum hadron to reach the calorimeter. Because of the consistent discrepancy across pseudorapidity and interaction lengths, this can be best explained by incomplete understanding of hadronic interactions with the detector [18]. For example, a hadron that scatters off of a nucleus in the inner detector can be deflected through a significant angle and not reach the expected location in the calorimeter. In addition, these interactions can produce secondary particles that are difficult to model.

The requirement used throughout the previous sections on the number of hits in the TRT reduces these effects by preferentially selecting tracks that do not undergo nuclear interactions. It is interesting to check how well the simulation models tracks with low numbers of TRT hits, which selects tracks that are more likely to have undergone a hadronic interaction. Figure 47 compares the distributions with  $N_{\text{TRT}} < 20$  to  $N_{\text{TRT}} > 20$  for real and simulated particles. As expected, the tracks with fewer hits are poorly modeled in the simulation as  $\langle E/p \rangle_{\text{COR}}$  differs by as much as 25% at low momentum.

Another interesting aspect of the simulation is the description of antiprotons at low momentum, where QGSP\_BERT and FTFP\_BERT have significant differences. This can be seen to have an effect in the inclusive response measurement when separated into positive and negative charge. The  $\langle E/p \rangle_{\text{COR}}$  distributions for positive and negative particles are shown in Figure 48, where a small difference between QGSP\_BERT and FTFP\_BERT can be seen in the distribution for

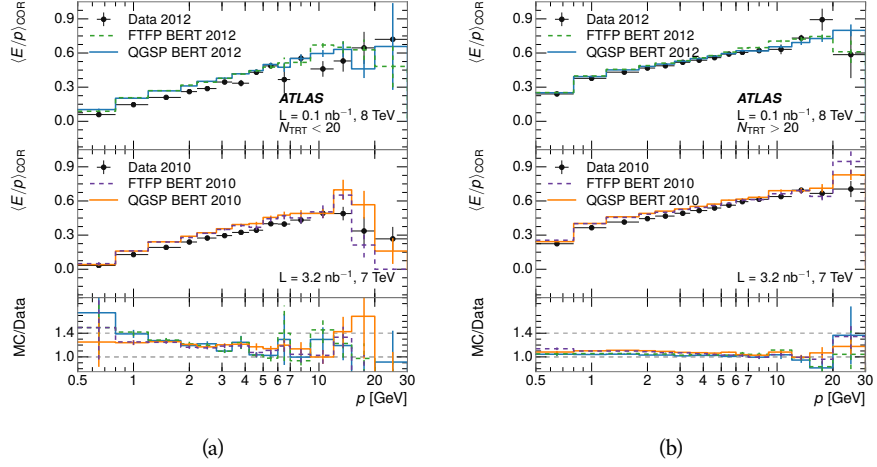


Figure 47: Comparison of the  $\langle E/p \rangle_{\text{COR}}$  for tracks with (a) less than and (b) greater than 20 hits in the TRT.

negative tracks. This is demonstrated more clearly in Figure 49, which shows the  $E/p$  distribution in the two simulations separated by charge. There is a clear difference around  $E/p > 1.0$ , which can be explained by the additional energy deposited by the annihilation of the antiproton in the calorimeter that is modeled well only in FTFP\_BERT. This is also explored with data using identified antiprotons in Section 8.3.

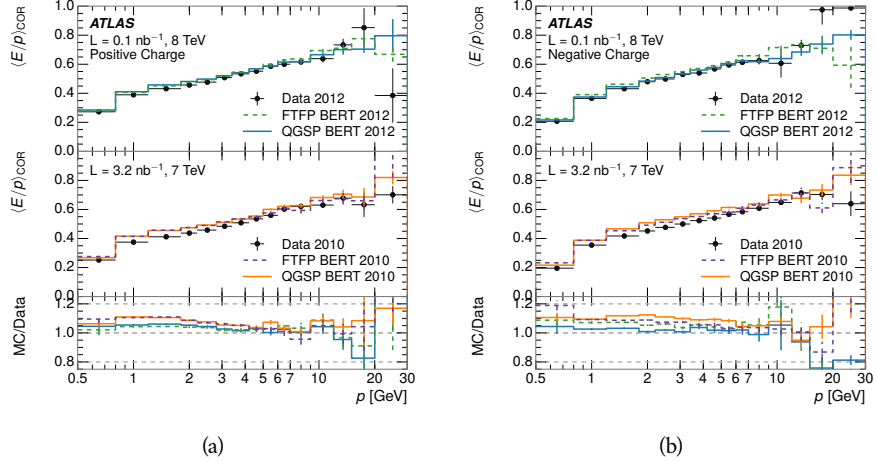


Figure 48: Comparison of the  $\langle E/p \rangle_{\text{COR}}$  for (a) positive and (b) negative tracks as a function of track momentum for tracks with  $|\eta| < 0.6$ .

The  $\langle E/p \rangle$  results in previous sections have considered the electromagnetic and hadronic calorimeters together as a single energy measurement, to emphasize the total energy deposited for a given particle. However, the deposits in each calorimeter are available separately and  $\langle E/p \rangle$  can be constructed for each layer. As the layers are composed of different materials and are modeled separately in the detector geometry, confirmation that the simulation matches the data well

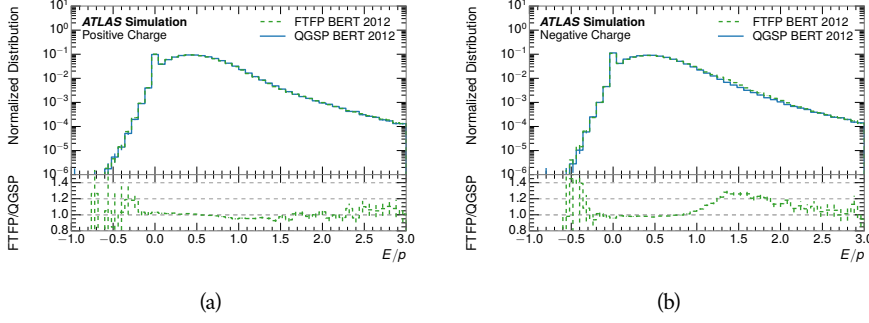


Figure 49: Comparison of the  $E/p$  distributions for (a) positive and (b) negative tracks with  $0.8 < p/\text{GeV} < 1.2$  and  $|\eta| < 0.6$ , in simulation with the FTFP\_BERT and QGSP\_BERT physics lists.

in each layer adds confidence in both the description of hadronic interactions with the two different materials and also the geometric description of each.

The technique discussed in Section 8.2.3 for selecting MIPS in the electromagnetic calorimeter is also useful in studying deposits in the hadronic calorimeter. Those MIPS deposit almost all of their energy exclusively in the hadronic calorimeter. Figure 50 shows  $\langle E/p \rangle_{\text{RAW}}^{\text{Had}}$ , where RAW indicates that no correction has been applied for neutral backgrounds and Had indicates that only clusters for the hadronic calorimeter are included. The RAW and COR versions of  $\langle E/p \rangle$  in this case are the same, as the neutral background is negligible in that calorimeter layer. The distributions are shown both for the original EM scale calibration and after LCW calibration. The data and simulation agree very well in this comparison, except in the lowest momentum bin which has 5% discrepancy that has already been seen in similar measurements.

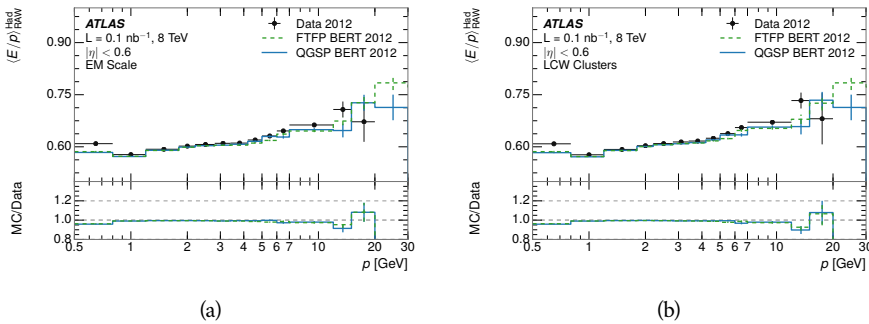


Figure 50: Comparison of the response of the hadronic calorimeter as a function of track momentum (a) at the EM-scale and (b) after the LCW calibration.

A similar comparison can be made in the electromagnetic calorimeter by selecting particles which have no associated energy in the hadronic calorimeter. These results are measured in terms of  $\langle E/p \rangle_{\text{COR}}^{\text{EM}}$ , where EM designates that only clusters in the electromagnetic calorimeter are included and COR designates that the neutral background is subtracted as the neutral background is present in this case. Figure 51 shows the analogous comparisons to Figure 50 in

the electromagnetic calorimeter. In this case the disagreement between data and simulation is more pronounced, with discrepancies as high as 5% over a larger range of momenta. This level of discrepancy indicates that the description of the electromagnetic calorimeter is actually the dominant source of discrepancy in the combined distributions in Section 8.2.4.

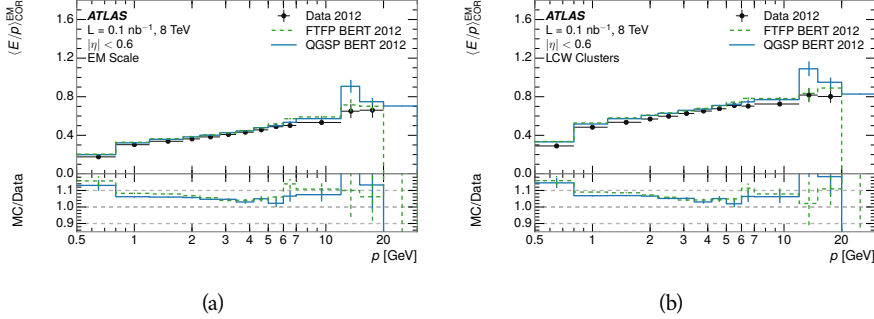


Figure 51: Comparison of the response of the EM calorimeter as a function of track momentum (a) at the EM-scale and (b) with the LCW calibration.

**NOTE: There are more studies that I skipped for brevity that could be included if interesting.  $E/p$  at different cluster threshold settings,  $E/p$  with pileup,  $E/p$  with cells. I also left out a lot of eta bins that appear in the paper so that this section didn't turn into 20 pages of plots.**

### 8.3 IDENTIFIED PARTICLE RESPONSE

The inclusive response measurement for hadrons can be augmented by measuring the response for specific particle species. The simulation models each particle type separately, and understanding the properties of each is important in constraining the uncertainty on jets. In order to select and measure specific hadrons, this section relies on the displaced decays of long-lived particles. Such decays can be identified by reconstructing secondary vertices with a requirement on mass. In particular,  $\Lambda$ ,  $\bar{\Lambda}$ , and  $K_S^0$  can be used to select a pure sample of protons, antiprotons, and pions, respectively.

#### 8.3.1 DECAY RECONSTRUCTION

The measurement of response for identified particles uses the same selection as for inclusive particles (Section 8.1.3) with a few additions. Each event used is required to have at least one secondary vertex, and the tracks are required to match to that vertex rather than the primary vertex. Pions are selected from decays of  $K_S^0 \rightarrow \pi^+ \pi^-$ , which is the dominant decay for  $K_S^0$  to charged particles. Protons are selected from decays of  $\Lambda \rightarrow \pi^- p$  and antiprotons from  $\bar{\Lambda} \rightarrow \pi^+ \bar{p}$ , which are similarly the dominant decays of  $\Lambda$  and  $\bar{\Lambda}$  to charged particles. The species of parent hadron in these decays is determined by reconstructing the mass of the tracks associated to the secondary vertex. The sign of the higher

momentum decay particle can distinguish between  $\Lambda$  and  $\bar{\Lambda}$ , which of course have the same mass, as the proton or antiproton is kinematically favored to have higher momentum. Examples of the reconstructed masses used to select these decays are shown in Figure 52.

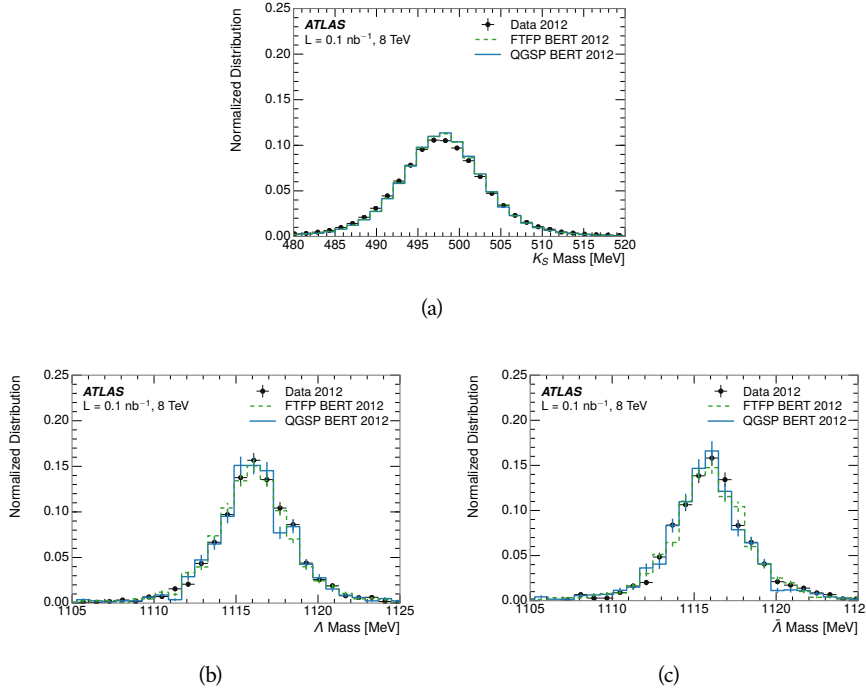


Figure 52: The reconstructed mass peaks of (a)  $K_S^0$ , (b)  $\Lambda$ , and (c)  $\bar{\Lambda}$  candidates.

The dominant backgrounds for the identified particle decays are nuclear interactions and combinatoric sources. These are suppressed by the kinematic requirements on the tracks as well as an additional veto which removes candidates that are consistent with both a  $\Lambda$  or  $\bar{\Lambda}$  and a  $K_S^0$  hypothesis, which is possible because of the different assumptions on particle mass in each case [19]. After these requirements, the backgrounds are found to be negligible compared to the statistical errors on these measurements.

### 8.3.2 IDENTIFIED RESPONSE

With these techniques the  $E/p$  distributions are extracted in data and simulation for each particle species and shown in Figure 53. These distributions are shown for a particular bin of  $E_a$  ( $2.2 < E_a/\text{GeV} < 2.8$ ), rather than  $p$ .  $E_a$  is the energy available to be deposited in the calorimeter: for pions  $E_a = \sqrt{p^2 + m^2}$ , for protons  $E_a = \sqrt{p^2 + m^2} - m$ , and for antiprotons  $E_a = \sqrt{p^2 + m^2} + m$ . The features of the  $E/p$  distributions are similar to the inclusive case. There is a small negative tail from noise and a large fraction of tracks with zero energy from particles which do not reach the calorimeter. The long positive tail is noticeably more pronounced for antiprotons because of the additional energy generated by the annihilation in addition to the neutral background.

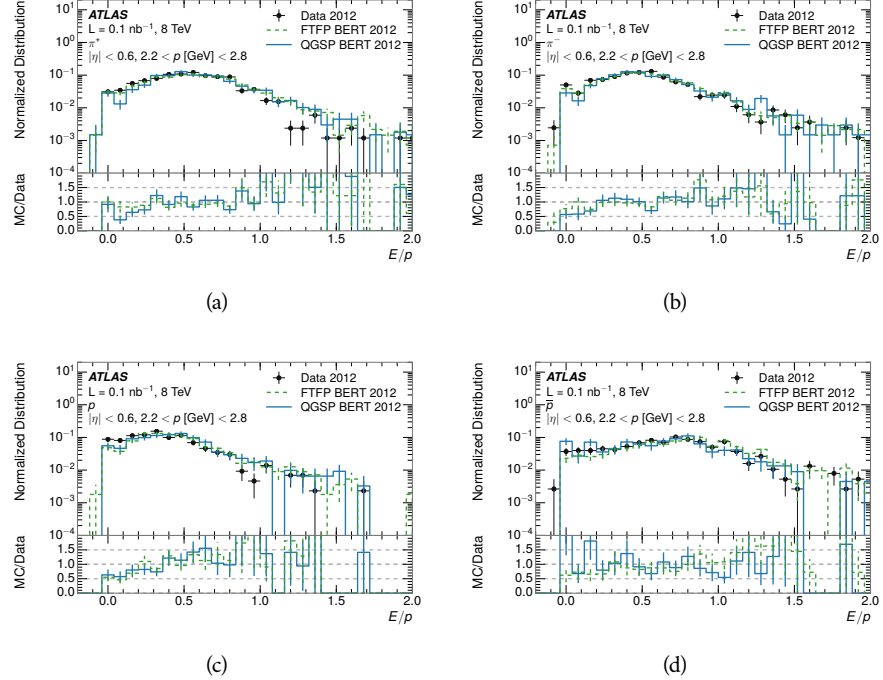


Figure 53: The  $E/p$  distribution for isolated (a)  $\pi^+$ , (b)  $\pi^-$ , (c) proton, and (d) anti-proton tracks.

The zero fraction is further explored in Figure 54 for pions and protons in data and simulation. The simulation consistently underestimates the zero fraction independent of particle species, which implies that this discrepancy is not caused by the model of a particular species but rather a feature common to all.

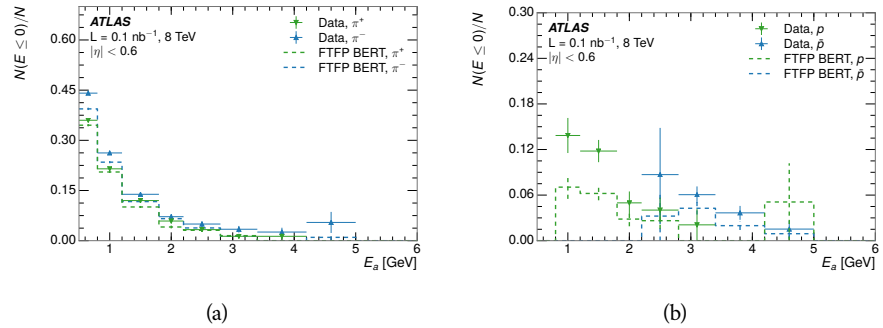


Figure 54: The fraction of tracks with  $E \leq 0$  for identified (a)  $\pi^+$  and  $\pi^-$ , and (b) proton and anti-proton tracks

It is also interesting to compare the response between the different particle species. One approach to do this is to measure the difference in  $\langle E/p \rangle$  between two types, which has the advantage of removing the neutral background. These differences are shown in various combinations in Figure 55. The response for  $\pi^+$  is greater on average than the response to  $\pi^-$  because of a charge-exchange effect which causes the production of additional neutral pions in the showers of

2288  $\pi^+$  [41]. The response for  $\pi^+$  is also greater on average than the response to  $p$ ,  
 2289 because a large fraction of the energy of  $\pi^+$  hadrons is converted to an electro-  
 2290 magnetic shower [42, 43]. However, the  $\bar{p}$  response is significantly higher than  
 2291 the response to  $\pi^-$  because of the annihilation of the antiproton. FTFP\_BERT  
 2292 does a better job of modeling this effect than QGSP\_BERT because of their differ-  
 2293 ent descriptions of  $\bar{p}$  interactions with material.

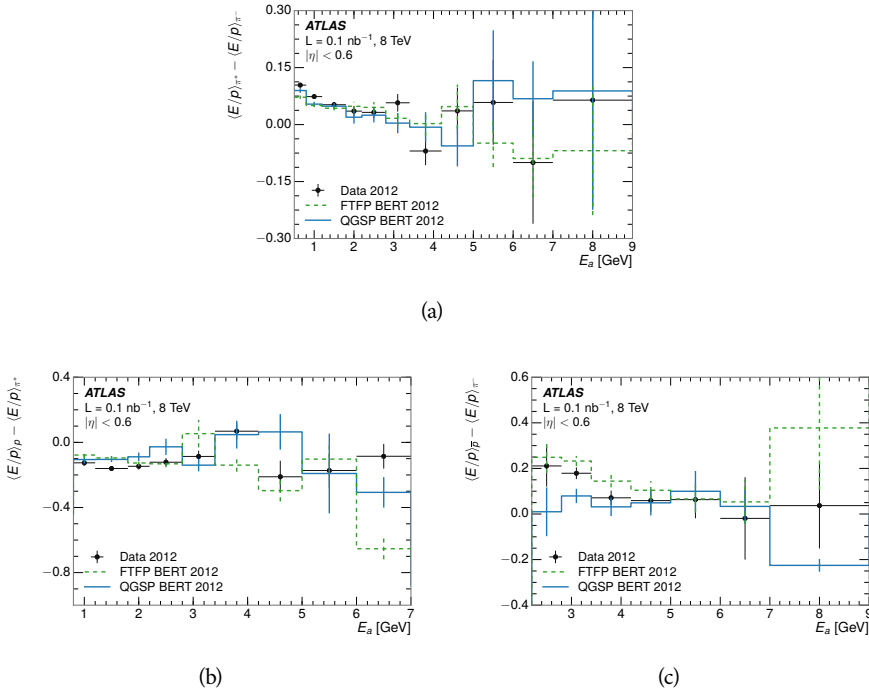


Figure 55: The difference in  $\langle E/p \rangle$  between (a)  $\pi^+$  and  $\pi^-$  (b)  $p$  and  $\pi^+$ , and (c)  $\bar{p}$  and  $\pi^-$ .

2294 It is also possible to remove the neutral background from these response dis-  
 2295 tributions using the same technique as in Section 8.2.3. The technique is largely  
 2296 independent of the particle species and so can be directly applied to  $\langle E/p \rangle$  for  
 2297 pions. The  $\langle E/p \rangle_{\text{COR}}$  distributions for pions are shown in Figure 56, which are  
 2298 very similar to the inclusive results. The inclusive hadrons are comprised mostly  
 2299 of pions, so this similarity is not surprising. It is also possible to see the small  
 2300 differences between  $\pi^+$  and  $\pi^-$  response here, where  $\langle E/p \rangle_{\text{COR}}$  is higher on av-  
 2301 erage for  $\pi^+$ . The agreement between data and simulation is significantly worse  
 2302 for the  $\pi^-$  distributions than for the  $\pi^+$ , with a discrepancy greater than 10%  
 2303 below 2-3 GeV.

### 2304 8.3.3 ADDITIONAL SPECIES IN SIMULATION

2305 The techniques above provide a method to measure the response separately for  
 2306 only pions and protons. However the hadrons which forms jets include a num-  
 2307 ber of additional species such as kaons and neutrons. The charged kaons are  
 2308 an important component of the inclusive charged hadron distribution, which is  
 2309 comprised of roughly 60-70% pions, 15-20% kaons, and 5-15% protons. These

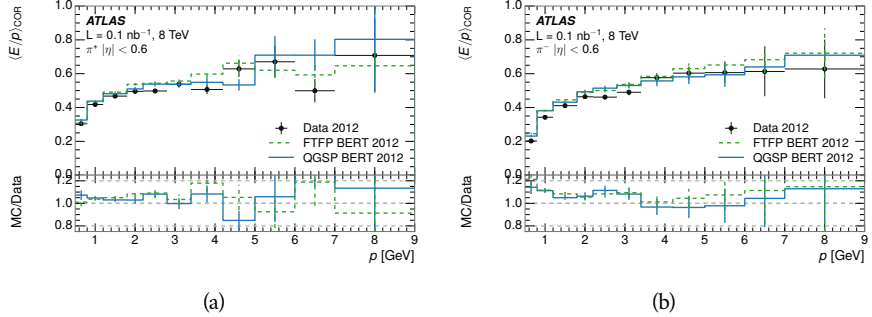


Figure 56:  $\langle E/p \rangle_{\text{COR}}$  as a function of track momentum for (a)  $\pi^+$  tracks and (b)  $\pi^-$  tracks.

are difficult to measure in data at the ATLAS detector, although a template subtraction technique has been proposed which may be effective with larger sample sizes [18]. The simulation of these particles includes noticeable differences in response at low energies, which are shown in Figure 57 for FTFP\_BERT. The significant differences in response between low energy protons and antiprotons are accounted for above in the definitions of  $E_a$ .

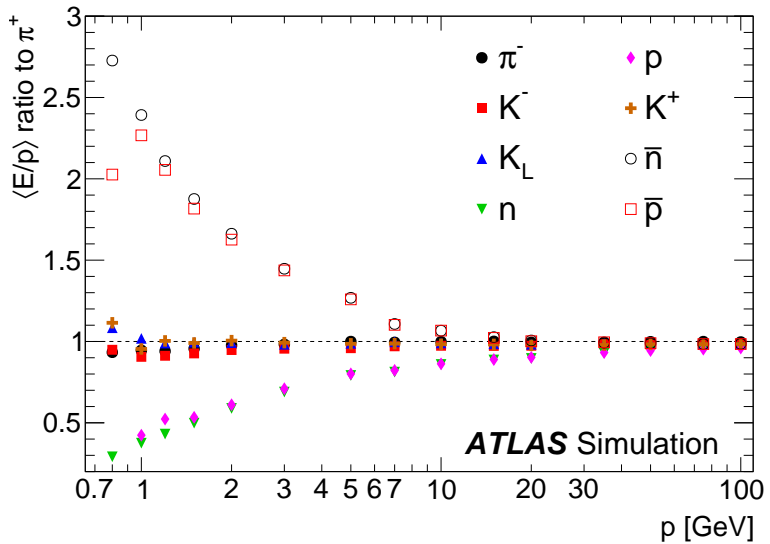


Figure 57: The ratio of the calorimeter response to single particles of various species to the calorimeter response to  $\pi^+$  with the physics list FTFP\_BERT.

2316 8.4 SUMMARY

2317 These various measurements of calorimeter response shown above for data and  
2318 simulation illuminate the accuracy of the simulation of hadronic interactions at  
2319 the ATLAS detector. The results were done using 2010 and 2012 data at 7 and 8  
2320 TeV, but reflect the most current understanding of the detector alignment and  
2321 geometry. A number of measurements focusing on a comparison between pro-

2322 tons and antiprotons suggest that FTFP\_BERT models those interaction more  
2323 accurately than QGSP\_BERT. These measurements, among others, were the moti-  
2324 vation to switch the default Geant4 simulation from FTFP\_BERT to QGSP\_BERT  
2325 for all ATLAS samples.

2326 Even with these updates, there are a number of small, approximately 5%, dis-  
2327 crepancies in response between the data and simulation at low energies. At  
2328 higher energies the simulation of hadronic interactions is very consistent with  
2329 data. Chapter 9 discusses how to use these observed differences to constrain the  
2330 jet energy scale and its associated uncertainties.



2331

## 2332 JET ENERGY RESPONSE AND UNCERTAINTY

## 2333 9.1 MOTIVATION

2334 As jets form a major component of many physics analyses at ATLAS, it is crucial  
 2335 to carefully calibrate the measurement of jet energies and to derive an uncer-  
 2336 tainty on that measurement. These uncertainties have often been the dominant  
 2337 systematic uncertainty in high-energy analyses at the LHC. Dijet and multijet  
 2338 balance techniques provide a method to constrain the JES and its uncertainty in  
 2339 data, and provide the default values used for ATLAS jet measurements at most  
 2340 energies [44]. These techniques are limited by their reliance on measuring jets  
 2341 in data, so they are statistically limited in estimating the jet energy scale at the  
 2342 highest jet energies. This chapter presents another method for estimating the jet  
 2343 energy scale and its uncertainty which builds up a jet from its components and  
 2344 thus can be naturally extended to high jet momentum. Throughout this chapter  
 2345 the jets studied are simulated using Pythia8 with the CT10 parton distribution  
 2346 set [45] and the AU2 tune [22], and corrections are taken from the studies includ-  
 2347 ing data and simulation in Chapter 8.

2348 As described in Section 7.4, jets are formed from topological clusters of energy  
 2349 in the calorimeters using the anti- $k_t$  algorithm. These clusters originate from a  
 2350 diverse spectrum of particles, in terms of both species and momentum, leading to  
 2351 significantly varied jet properties and response between jets of similar produced  
 2352 momentum. Figure 58 shows the simulated distribution of particles within jets  
 2353 at a few examples energies. The  $E/p$  measurements provide a thorough under-  
 2354 standing of the dominant particle content of jets, the charged hadrons.

## 2355 9.2 UNCERTAINTY ESTIMATE

2356 Simulated jets are not necessarily expected to correctly model the energy de-  
 2357 posits in the calorimeters, because of the various discrepancies discussed in Chap-  
 2358 ter 8. To evaluate a jet energy response, the simulated jet energies are compared  
 2359 to a corrected jet built up at the particle level. Each cluster in a jet is associated  
 2360 to the truth particle which deposited it, and the energy in that cluster is then  
 2361 corrected for a number of effects based on measurements in data. The primary  
 2362 corrections come from the single hadron response measurements in addition to  
 2363 response measured using the combined test beam which covers higher momen-  
 2364 tum particles [46]. These corrections include both a shift ( $\Delta$ ), in order to make  
 2365 the simulation match the average response in data, and an uncertainty ( $\sigma$ ) asso-  
 2366 ciated with the ability to constrain the difference between data and simulation.  
 2367 Some of the dominant sources of uncertainty are itemized in Table 7 with typi-  
 2368 cal values, and the full list considered is described in detail in the associated pa-

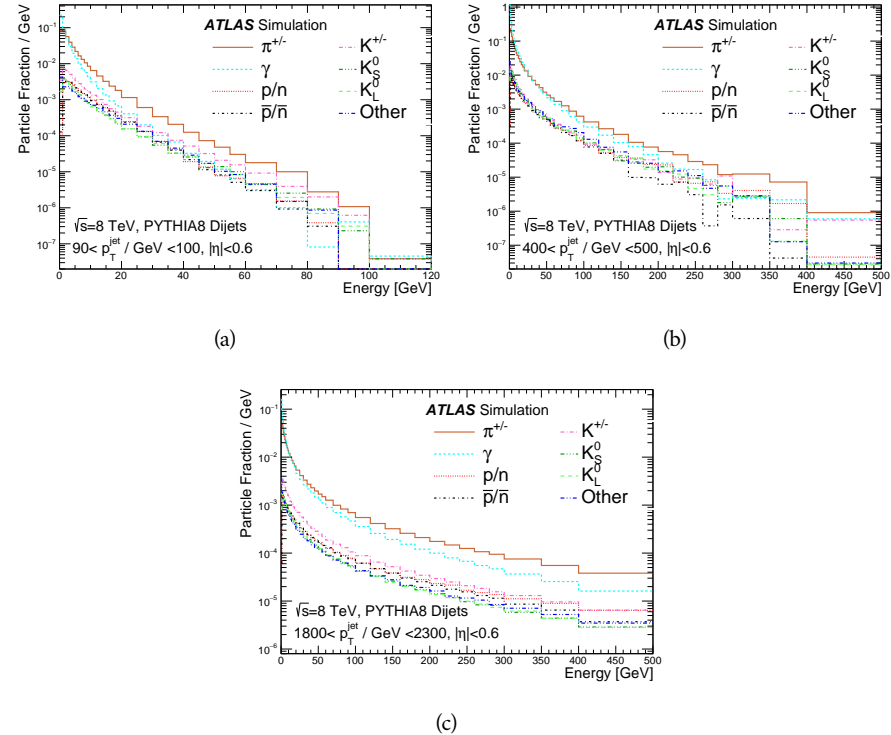


Figure 58: The spectra of true particles inside anti- $k_t$ ,  $R = 0.4$  jets with (a)  $90 < p_T/\text{GeV} < 100$ , (b)  $400 < p_T/\text{GeV} < 500$ , and (c)  $1800 < p_T/\text{GeV} < 2300$ .

2369 per [18]. These uncertainties cover differences between the data and simulation  
 2370 in the modeling of calorimeter response to a given particle. No uncertainties are  
 2371 added for the difference between particle composition of jets in data and simu-  
 2372 lation.

2373 From these terms, the jet energy scale and uncertainty is built up from indi-  
 2374 vidual energy deposits in simulation. Each uncertainty term is treated indepen-  
 2375 dently, and are taken to be gaussian distributed. The resulting scale and uncer-  
 2376 tainty is shown in Figure 59, where the mean response is measured relative to  
 2377 the calibrated energy reported by simulation. The dominant uncertainties come  
 2378 from the statistical uncertainties on the  $E/p$  measurements at lower energies and  
 2379 the additional uncertainty for out of range measurements at higher energies. The  
 2380 total uncertainty from this method at intermediate jet energies is comparable to  
 2381 other simulation-based methods [47] and is about twice as large as in-situ meth-  
 2382 ods using data [44]. This method is the only one which provides an estimation  
 2383 above 1.8 TeV, however, and so is still a crucial technique in analyses that search  
 2384 for very energetic jets.

2385 These techniques can also be used to measure the correlation between bins of  
 2386 average reconstructed jet momentum across a range of  $p_T$  and  $|\eta|$ , where cor-  
 2387 relations are expected because of a similarity in particle composition at similar  
 2388 energies. Figure 60 shows these correlations, where the uncertainties on jets in  
 2389 neighboring bins are typically between 30% and 60% correlated. The uncertainty  
 2390 on all jets becomes significantly correlated at high energies and larger pseudora-

Abbrev.	Description	$\Delta$ (%)	$\sigma$ (%)
In situ $E/p$	The comparison of $\langle E/p \rangle_{\text{COR}}$ as described in Chapter 8 with statistical uncertainties from 500 MeV to 20 GeV.	0-3	1-5
CTB	The main $\langle E/p \rangle$ comparison uncertainties, binned in $p$ and $ \eta $ , as derived from the combined test beam results, from 20 to 350 GeV [46].	0-3	1-5
$E/p$ Zero Fraction	The difference in the zero-fraction between data and MC simulation from 500 MeV to 20 GeV.	5-25	1-5
$E/p$ Threshold	The uncertainty in the EM calorimeter response from the potential mismodeling of threshold effects in topological clustering.	0	0-10
Neutral	The uncertainty in the calorimeter response to neutral hadrons based on studies of physics model variations.	0	5-10
$K_L$	An additional uncertainty in the response to neutral $K_L$ in the calorimeter based on studies of physics model variations.	0	20
$E/p$ Misalignment	The uncertainty in the $p$ measurement from misalignment of the ID.	0	1
Hadrons, $p > 350$ GeV	A flat uncertainty for all particles above the energy range or outside the longitudinal range probed with the combined test beam.	0	10

Table 7: The dominant sources of corrections and systematic uncertainties in the [JES](#) estimation technique, including typical values for the correcting shift ( $\Delta$ ) and the associated uncertainty ( $\sigma$ ).

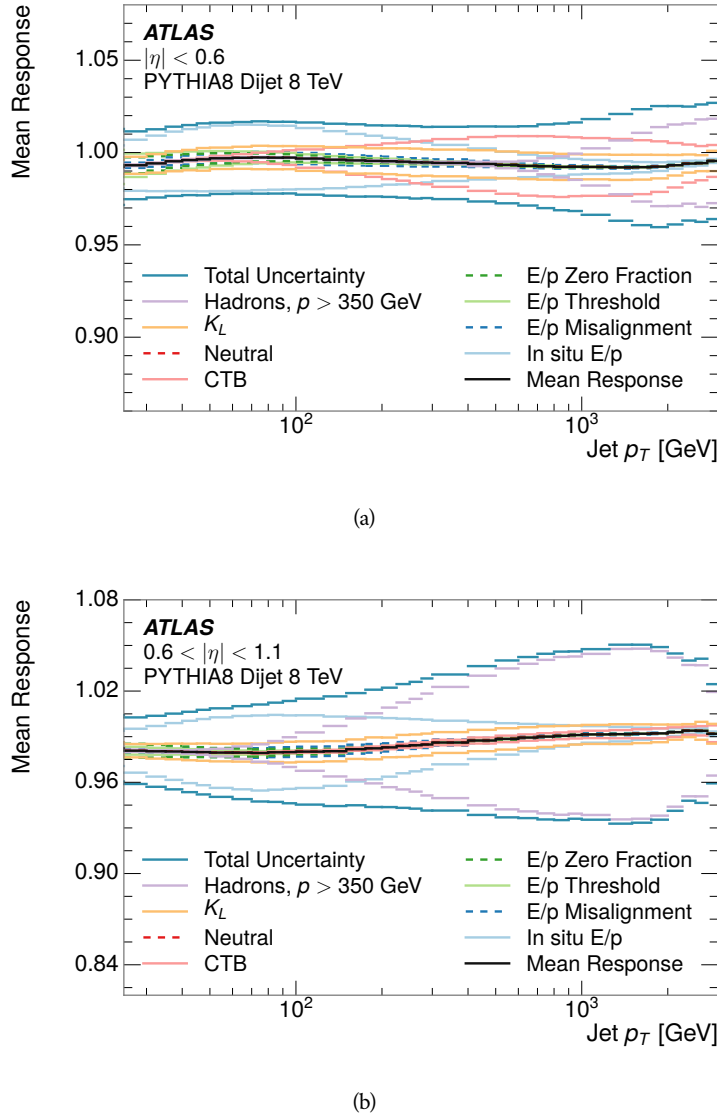


Figure 59: The [JES](#) uncertainty contributions, as well as the total [JES](#) uncertainty, as a function of jet  $p_T$  for (a)  $|\eta| < 0.6$  and (b)  $0.6 < |\eta| < 1.1$ .

2391      pidities, when the uncertainty becomes dominated by the single term reflecting  
 2392      out of range particles.

### 2393      9.3 SUMMARY

2394      The technique described above provides a jet energy scale and uncertainty by  
 2395      building up jet corrections from the energy deposits of constituent particles. The  
 2396       $E/p$  measurements are crucial in providing corrections for the majority of parti-  
 2397      cles in the jets. The uncertainty derived this way is between 2 and 5% and is about  
 2398      twice as large at corresponding momentum than jet balance methods. However  
 2399      this is the only uncertainty available for very energetic jets using 2012 data and  
 2400      simulation, and repeating this method with Run 2 data and simulation will be

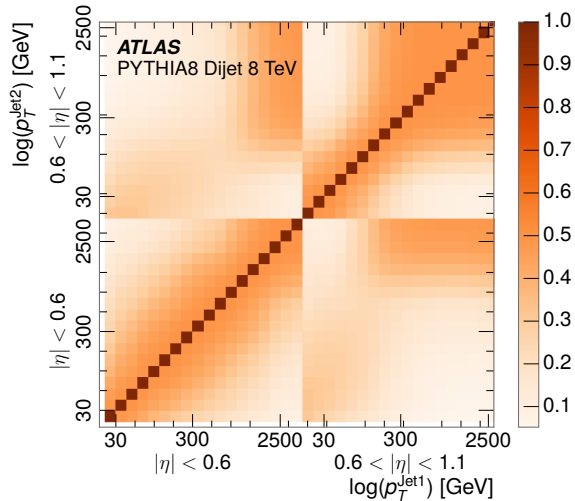


Figure 60: The **JES** correlations as a function of jet  $p_T$  and  $|\eta|$  for jets in the central region of the detector.

2401 important in providing an uncertainty for the most energetic jets in 13 TeV col-  
 2402 lisions.



2403

## PART V

2404

### SEARCH FOR LONG-LIVED PARTICLES

2405

You can put some informational part preamble text here.



2406

2407 LONG-LIVED PARTICLES IN ATLAS

---

2408 As discussed in Section ??, various limitations in the SM suggest a need for new  
 2409 particles at the TeV scale. A wide range of extensions to the Standard Model  
 2410 predict that these new particles can have lifetimes greater than approximately  
 2411 one-hundredth of a nanosecond. These include theories with universal extra-  
 2412 dimensions [48, 49], with new fermions [50], and with leptoquarks [51]. Many  
 2413 SUSY theories also produce these Long-Lived Particles (LLPs), in both R-Parity  
 2414 violating [52–54] and R-Parity conserving [55–58] formulations. Split super-  
 2415 symmetry [59, 60], for example, predicts long-lived gluinos with O(TeV) masses.  
 2416 This search focuses specifically on the SUSY case, but many of the results are  
 2417 generic to any model with LLPs.

2418 Long-lived gluinos or squarks carry color-charge and will thus hadronize into  
 2419 color neutral bound states called R-Hadrons. These are composit particles like  
 2420 the usual hadrons but with one supersymmetric constituent, for example  $\tilde{g}q\bar{q}$   
 2421 and  $\tilde{q}\bar{q}$ . Through this hadronization process, the neutral gluino can acquire a  
 2422 charge. Gluino pair production,  $pp \rightarrow \tilde{g}\tilde{g}$  has the largest cross sectional increase  
 2423 with the increase in energy to 13 TeV, and so this search focuses on gluino R-  
 2424 Hadrons. Planned future updates will extend the case to explicitly include squark  
 2425 and chargino models, but the method covers any long-lived, charged, massive  
 2426 particle.

## 2427 10.1 EVENT TOPOLOGY

2428 The majority of SUSY models predict that gluinos will be produced in pairs at  
 2429 the LHC, through processes like  $pp \rightarrow q\bar{q} \rightarrow \tilde{g}\tilde{g}$  and  $pp \rightarrow gg \rightarrow \tilde{g}\tilde{g}$ , where the  
 2430 gluon mode dominates for the collision energy and gluino masses considered  
 2431 for this search. During their production, the long-lived gluinos hadronize into  
 2432 color singlet bound states including  $\tilde{g}q\bar{q}$ ,  $\tilde{g}qqq$ , and even  $\tilde{g}g$  [61]. The probability  
 2433 to form the gluon-only bound states is a free parameter usually taken to be 0.1,  
 2434 while the meson states are favored among the R-Hadrons [62]. The charged and  
 2435 neutral states are approximately equally likely for mesons, so the R-Hadrons will  
 2436 be charged roughly 50% of the time.

2437 These channels produce R-Hadrons with large  $p_T$ , comparable to their mass,  
 2438 so that they typically propagate with  $0.2 < \beta < 0.9$  [62]. The fragmentation that  
 2439 produces these hadrons is very hard, so the jet structure around the R-Hadron  
 2440 is minimal, with less than 5 GeV of summed particle momentum expected in a  
 2441 cone of  $\Delta R < 0.25$  around the R-Hadron [62]. After hadronization, depending  
 2442 on the gluino lifetime, the R-Hadrons then decay into hadrons and a LSP [61].

2443 In summary, the expected event for pair-produced long-lived gluinos is very  
 2444 simple: two isolated, high-momentum R-Hadrons that propagate through the  
 2445 detector before decaying into jets. The observable features of such events depend

2446 strongly on the interaction of the R-Hadron with the material of the detector and  
 2447 also its lifetime. Section 10.1.1 describes the interactions of R-Hadrons which  
 2448 reach the various detector elements in ATLAS and Section 10.1.2 provides a sum-  
 2449 mary of the observable event descriptions for R-Hadrons of various lifetimes.

2450 10.11 DETECTOR INTERACTIONS

2451 After approximately 0.2 ns, the R-Hadron reaches the pixel detector. If charged,  
 2452 it deposits energy into the material through repeated single collisions that result  
 2453 in ionization of the silicon substrate [7]. Because of its comparatively low  $\beta$ , the  
 2454 ionization energy can be significantly greater than expected for SM particles be-  
 2455 cause the most-probable energy loss grows significantly as  $\beta$  decreases [7]. This  
 2456 large ionization can be measured through the ToT read out from the pixel detec-  
 2457 tor as described in Section 7.1.2. Large ionization in the inner detector is one of  
 2458 the major characteristic features of LLPs.

2459 Throughout the next few nanoseconds, the R-Hadron propagates through the  
 2460 remainder of the inner detector. A charged R-Hadron will provide hits in each  
 2461 of these systems as would any other charged particle, and can be reconstructed  
 2462 as a track. The track reconstruction provides a measurement of its trajectory  
 2463 and thus its momentum as described in Section 7.1. The large momentum is  
 2464 another characteristic feature of massive particles produced at the LHC. **Note: At**  
 2465 **this point I am failing to mention that the TRT provides a possible dE/dx**  
 2466 **measurement, because no one uses it as far as I know.**

2467 As of roughly 20 ns, the R-Hadron enters the calorimeter where it interacts  
 2468 hadronically with the material. Because of its large mass and momentum, the  
 2469 R-Hadron does not typically stop in the calorimeter, but rather deposits a small  
 2470 fraction of its energy through repeated interactions with nucleons. The proba-  
 2471 bility of interaction between the gluino itself and a nucleon is low because the  
 2472 cross section drops off with the inverse square of its mass, so the interactions are  
 2473 primarily governed by the light constituents [63]. Each of these interactions can  
 2474 potentially change that quark content and thus change the sign of the R-Hadron,  
 2475 so that the charge at exit is typically uncorrelated with the charge at entry [62].  
 2476 The total energy deposited in the calorimeters during the propagation is small  
 2477 compared to the kinetic energy of the R-Hadron, around 20-40 GeV, so that  
 2478  $E/p$  is typically less than 0.1 [62].

2479 Then, 30 ns after the collision, it reaches the muon system, where it again  
 2480 ionizes in the material if charged and can be reconstructed as a muon track. Be-  
 2481 cause of the charge-flipping interactions in the calorimeter, this track may have  
 2482 the opposite sign of the track reconstructed in the inner detector, or there may  
 2483 be a track present when there was none in the inner detector and vice-versa. The  
 2484 propagation time at the typically lower  $\beta$  results in a significant delay compared  
 2485 to muons, and that delay can be assessed in terms of a time-of-flight measure-  
 2486 ment. Because of the probability of charge-flip and late arrival, there is a signif-  
 2487 icant chance that an R-Hadron which was produced with a charge will not be  
 2488 identified as a muon. The long time-of-flight is another characteristic feature of  
 2489 R-Hadrons which are reconstructed as muons.

## 2490 10.1.2 LIFETIME DEPENDENCE

2491 The above description assumed a lifetime long enough for the R-Hadron to exit  
 2492 the detector, which through this search is referred to as “stable”, even though  
 2493 the particle may decay after exiting the detector. There are several unique sig-  
 2494 natures at shorter lifetimes where the R-Hadron decays in various parts of the  
 2495 inner detector; these lifetimes are referred to as “metastable”.

2496 The shortest case where the R-Hadron is considered metastable is for life-  
 2497 times around 0.01 ns, where the particle decays before reaching any of the de-  
 2498 tector elements. Although the R-Hadrons are produced opposite each other in  
 2499 the transverse plane, each R-Hadron decays to a jet and an [LSP](#). The [LSPs](#) are not  
 2500 measured, so the produced jets can be significantly imbalanced in the transverse  
 2501 plane which results in large missing energy. That missing energy can be used  
 2502 to trigger candidate events, and provides the most efficient trigger option for  
 2503 shorter lifetimes. Additionally, the precision of the tracking system allows the  
 2504 displaced vertex of the R-Hadron decay to be reconstructed from the charged  
 2505 particles in the jet. The distance of that vertex from the interaction point can  
 2506 be used to distinguish R-Hadron decays from other processes. Figure 61 shows  
 2507 a schematic diagram of an example R-Hadron event with such a lifetime. The  
 2508 diagram is not to scale, but instead illustrates the detector interactions in the  
 2509 pixel detector, calorimeters, and muon system. It includes a representation of  
 2510 the charged R-Hadron and the neutral R-Hadron, as well as the [LSPs](#) and jets  
 2511 (shown as charged hadrons) produced in the decay. Neutral hadrons may also  
 2512 be produced in the decay but are not depicted. Previous searches on [ATLAS](#) have  
 2513 used the displaced vertex to target [LLP](#) decays [64].

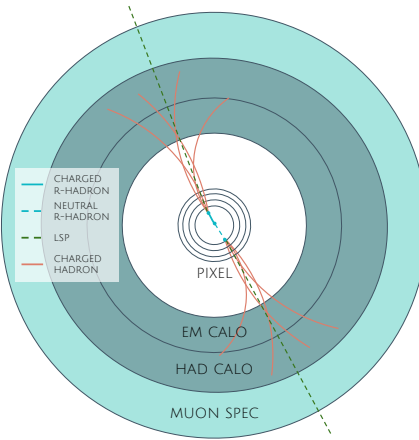


Figure 61: A schematic diagram of an R-Hadron event with a lifetime around 0.01 ns.  
 The diagram includes one charged R-Hadron (solid blue), one neutral R-Hadron (dashed blue), [LSPs](#) (dashed green) and charged hadrons (solid orange).  
 The pixel detector, calorimeters, and muon system are illustrated but not to scale.

2514 The next distinguishable case occurs at lifetimes greater than 0.1 ns, where  
 2515 the R-Hadron forms a partial track in the inner detector. If the decay products  
 2516 are sufficiently soft, they may not be reconstructed, and this forms a unique sig-

2517 nature of a disappearing track. An example of such an event is illustrated in  
 2518 Figure 62, which shows the short track in the inner detector and the undetected  
 2519 soft charged hadron and LSP that are produced. A dedicated search on ATLAS used  
 2520 the disappearing track signature to search for LLP in Run 1 [65]. **zNote: might**  
 2521 **not be worth mentioning the disappearing track here since it is actually a**  
 2522 **chargino search, the soft pion is pretty unique to charginos.**

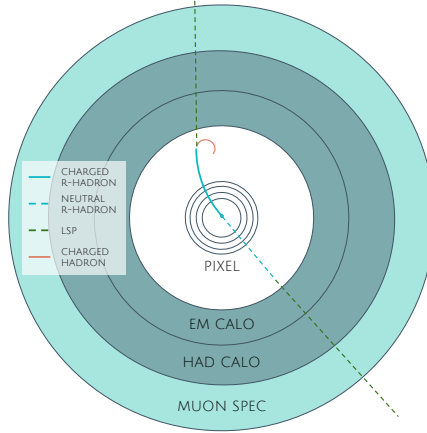


Figure 62: A schematic diagram of an R-Hadron event with a lifetime around 4 ns. The diagram includes one charged R-Hadron (solid blue), one neutral R-Hadron (dashed blue), LSPs (dashed green) and a charged hadron (solid orange). The pixel detector, calorimeters, and muon system are illustrated but not to scale.

2523 If the decay products are not soft, the R-Hadron daughters form jets, resulting  
 2524 in an event-level signature of up to two high-momentum tracks, jets, and signif-  
 2525 icant missing energy. The missing energy has the same origin as in the case of  
 2526 0.01 ns lifetimes, from the decay to unmeasured particles, and again can be large.  
 2527 The high-momentum tracks will also have the characteristically high-ionization  
 2528 of massive, long-lived particles in the inner detector. Figure 63 illustrates an ex-  
 2529 ample event with one charged R-Hadron which decays after approximately 10 ns,  
 2530 and shows how the jets from the decay can still be reconstructed in the calorime-  
 2531 ter. Several previous searches on ATLAS from Run 1 have used this signature to  
 2532 search for R-Hadrons [66, 67], including a dedicated search for metastable parti-  
 2533 cles [68].

2534 If the lifetime is longer than several nanoseconds, in the range of 15-30 ns,  
 2535 the R-Hadron decay can occur in or after the calorimeters, but prior to reaching  
 2536 the muon system. This case is similar to the above, although the jets may not be  
 2537 reconstructed, and is covered by many of the same search strategies. The events  
 2538 still often have large missing energy, although it is generated through different  
 2539 mechanisms. The R-Hadrons do not deposit much energy in the calorimeters, so  
 2540 a neutral R-Hadron will not enter into the missing energy calculation. A charged  
 2541 R-Hadron opposite a neutral R-Hadron will thus generate significant missing en-  
 2542 ergy, and close to 50% of pair-produced R-Hadron events fall into this category.  
 2543 If both R-Hadrons are neutral then the missing energy will be low because nei-  
 2544 ther is detected. Two charged R-Hadrons will also result in low missing energy  
 2545 because both are reconstructed as tracks and will balance each other in the trans-

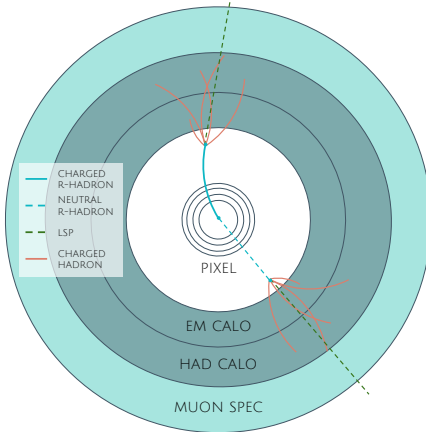


Figure 63: A schematic diagram of an R-Hadron event with a lifetime around 5 ns. The diagram includes one charged R-Hadron (solid blue), one neutral R-Hadron (dashed blue), LSPs (dashed green) and charged hadrons (solid orange). The pixel detector, calorimeters, and muon system are illustrated but not to scale.

2546      verse plane. A small fraction of the time, one of the charged R-Hadron tracks may  
 2547      fail quality requirements and thus be excluded from the missing energy calcula-  
 2548      tion and again result in significant missing energy. Figure 64 illustrates another  
 2549      example event with one charged R-Hadron which decays after approximately 20  
 2550      ns, and shows how the jets from the decay might not be reconstructed.

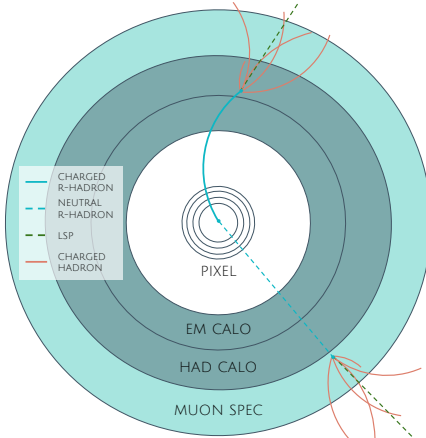


Figure 64: A schematic diagram of an R-Hadron event with a lifetime around 20 ns. The diagram includes one charged R-Hadron (solid blue), one neutral R-Hadron (dashed blue), LSPs (dashed green) and charged hadrons (solid orange). The pixel detector, calorimeters, and muon system are illustrated but not to scale.

2551      The longest lifetimes, the stable case, has all of the features of the 30-50 ns case  
 2552      but with the addition of muon tracks for any R-Hadrons that exit the calorimeter  
 2553      with a charge. That muon track can provide additional information from time-  
 2554      of-flight measurements to help identify LSPs. An example of the event topology  
 2555      for one charged and one neutral stable R-Hadron is shown in Figure 65. Some  
 2556      searches on ATLAS have included this information to improve the search reach  
 2557      for stable particles [67, 69].

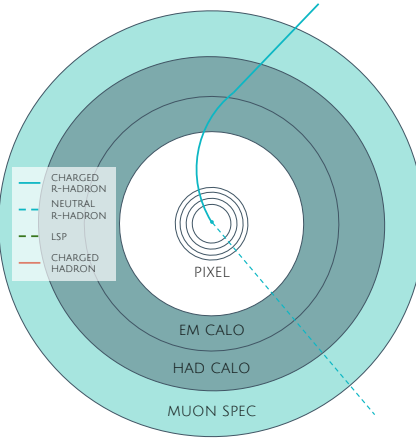


Figure 65: A schematic diagram of an R-Hadron event with a lifetime around 20 ns. The diagram includes one charged R-Hadron (solid blue) and one neutral R-Hadron (dashed blue). The pixel detector, calorimeters, and muon system are illustrated but not to scale.

## 2558 10.2 SIMULATION

2559 All of the event topologies discussed above are explored by simulations of R-  
 2560 Hadron events in the [ATLAS](#) detector. A large number of such samples are gen-  
 2561 erated to determine signal efficiencies, to measure expected yields, and to esti-  
 2562 mate uncertainties. The primary interaction, pair production of gluinos with  
 2563 masses between 400 and 3000 GeV, is simulated using [Pythia 6.4.27](#) [70]  
 2564 with the AUET2B [71] set of tuned parameters for the underlying event and  
 2565 the CTEQ6L1 [45] parton distribution function ([PDF](#)) set. The simulated inter-  
 2566 actions include a modeling of pileup by adding secondary, minimum bias in-  
 2567 teractions from both the same (in-time pileup) and nearby (out-of-time pileup)  
 2568 bunch crossings. This event generation is then augmented with a dedicated  
 2569 hadronization routine to hadronize the long-lived gluinos into final states with  
 2570 R-Hadrons [72], with the probability to form a gluon-gluino bound set at 10% [73].

2571 The cross sections used for these processes are calculated at next-to-leading  
 2572 order ([NLO](#)) in the strong coupling constant with a resummation of soft-gluon  
 2573 emmission at next-to-leading logarithmic ([NLL](#)) [74–78]. The nominal predic-  
 2574 tions and the uncertainties for each mass point are taken from an envelope of  
 2575 cross-section predictions using different [PDF](#) sets and factorization and renor-  
 2576 malization scales [79].

2577 The R-Hadrons then undergo a full detector simulation [], where the interac-  
 2578 tions of the R-Hadrons with the material of the detector are described by dedi-  
 2579 cated [Geant4](#) [15] routines. These routines model the interactions described in  
 2580 Section 10.1.1, including the ionizing interactions in the silicon modules of the  
 2581 inner detector and the R-Hadron-nucleon interactions in the calorimeters [80,  
 2582 81]. The specific routine chosen to describe the interactions of the R-Hadrons  
 2583 with nucleons, the “generic model”, uses a pragmatic approach where the scatter-  
 2584 ing cross section is taken to be a constant 12 mb per light quark. In this model

2585 the gluino itself does not interact at all except through its role as a reservoir of  
 2586 kinetic energy.

2587 The lifetimes of these R-Hadrons are then simulated at several working points,  
 2588  $\tau = 0.1, 1.0, 3.0, 10, 30, 50$  and detector stable, where the particle is required to  
 2589 decay after propagating for a time compatible with its lifetime. Only one decay  
 2590 mode is simulated for these samples,  $\tilde{g} \rightarrow q\bar{q}\tilde{\chi}_1^0$  with the neutralino mass set to  
 2591 100 GeV, which is chosen because it has the highest sensitivity among all of the  
 2592 modes studied in previous searches [68]. Heavier neutralinos have similar results  
 2593 but generate less missing energy which reduces the efficiency of triggering.

2594 All of the simulated events are then reconstructed using the same software  
 2595 used for collision data. The fully reconstructed events are then reweighted to  
 2596 match the distribution of initial state radiation in an alternative sample of events,  
 2597 generated with MG5\_aMC@NLO [82], which has a more accurate description of ra-  
 2598 diate effects than Pythia6. This reweighting provides a more accurate descrip-  
 2599 tion of the momentum of the gluino-gluino system and is important in modeling  
 2600 the efficiency of triggering and offline event selection.



2601

2602 EVENT SELECTION

---

2603 The [LLPs](#) targeted by this search differ in their interactions with the detector from  
 2604 [SM](#) particles primarily because of their large mass. When produced at the ener-  
 2605 gies available at the [LHC](#), that large mass results in a low  $\beta$  (typically  $0.2 < \beta <$   
 2606 0.9). Such slow-moving particles heavily ionize in detector material. Each layer  
 2607 of the pixel detector provides a measurement of that ionization, through [ToT](#), as  
 2608 discussed in Section 7.1.2. The ionization in the pixel detector, quantified in  
 2609 terms of  $dE/dx$ , provides the major focus for this search technique, along with  
 2610 the momentum measured in the entire inner detector. It is effective both for its  
 2611 discriminating power and its use in reconstructing a particle's mass, and it can  
 2612 be used for a wide range of masses and lifetimes as discussed in Section 10.1.2.  
 2613 However  $dE/dx$  needs to be augmented with a few additional selection require-  
 2614 ments to provide a mechanism for triggering and to further reduce backgrounds.

2615 Ionization itself is not currently accessible for triggering, so this search in-  
 2616 stead relies on  $E_T^{\text{miss}}$  to trigger signal events. Although triggering on  $E_T^{\text{miss}}$  can  
 2617 be inefficient,  $E_T^{\text{miss}}$  is often large for many production mechanisms of [LLPs](#), as  
 2618 discussed in Section 10.1.

2619 The use of ionization to reject [SM](#) backgrounds relies on well-measured, high-  
 2620 momentum tracks, so some basic requirements on quality and kinematics are  
 2621 placed on the tracks considered in this search. These quality requirements have  
 2622 been significantly enhanced in Run 2 by a newly introduced tracking variable  
 2623 that is very effective in removing highly-ionizing backgrounds caused by over-  
 2624 lapping tracks. A few additional requirements are placed on the tracks consid-  
 2625 ered for [LLP](#) candidates that increase background rejection by targeting specific  
 2626 types of [SM](#) particles. These techniques provide a significant analysis improve-  
 2627 ment over previous iterations of ionization-based searches on ATLAS by provid-  
 2628 ing additional background rejection with minimal loss in signal efficiency.

2629 The ionization measurement with the Pixel detector can be calibrated to pro-  
 2630 vide an estimator of  $\beta\gamma$ . That estimate, together with the momentum measure-  
 2631 ment provided by tracking, can be used to reconstruct a mass for each track  
 2632 which traverses the pixel detector. That mass variable will be peaked at the [LLP](#)  
 2633 mass for any signal, and provides an additional tool to search for an excess. In  
 2634 addition to an explicit requirement on ionization, this search constructs a mass-  
 2635 window for each targeted signal mass in order to evaluate any excess of events  
 2636 and to set limits.

2637 The strategy discussed here is optimized for lifetimes of  $O(1) - O(10)$  ns.  
 2638 Pixel ionization is especially useful in this regime as particles only need to prop-  
 2639 agate through the first seven layers of the inner detector, about 37 cm from the  
 2640 beam axis. The search is still competitive with other searches for [LLPs](#) at longer  
 2641 lifetimes, because the primary discriminating variables are still applicable even  
 2642 for particles that do not decay within the detector [69]. Although the majority of

2643 the requirements will be the same for all lifetimes, two signal regions are defined  
 2644 to optimize separately for intermediate and long lifetime particles.

## 2645 11.1 TRIGGER

2646 Triggering remains a significant difficulty in defining an event selection with  
 2647 high signal efficiency in a search for LLPs. There are no triggers available in  
 2648 the current ATLAS system that can fire directly from a high momentum track  
 2649 with large ionization (Section 6.6). Although in some configurations a charged  
 2650 LLP can fire muon triggers, this requirement introduces significant model depen-  
 2651 dence on both the allowed lifetimes and the interactions in the calorimeter [62],  
 2652 as discussed in Section 10.1.1.

2653 For a search targeting particles which may decay prior to reaching the muon  
 2654 system, the most efficient available trigger is based on missing energy [62]. As  
 2655 discussed in Section 10.1, signal events can produce significant  $E_T^{\text{miss}}$  by a few  
 2656 mechanisms. At the trigger level however, the missing energy is only calculated  
 2657 using the calorimeters (Section 6.6) where the R-Hadrons deposit little energy.  
 2658 So, at short lifetimes,  $E_T^{\text{miss}}$  measured in the calorimeter is generated by an im-  
 2659 balance between the jets and undetected LSPs produced in R-Hadron decays. At  
 2660 longer lifetimes, without the decay products, missing energy is only produced in  
 2661 the calorimeters when the R-Hadrons recoil against an initial state radiation (ISR)  
 2662 jet.

2663 These features are highlighted in Figure 66, which shows the  $E_T^{\text{miss}}$  distribu-  
 2664 tions for simulated short lifetime (3 ns) and stable R-Hadron events. The figure  
 2665 includes both the offline  $E_T^{\text{miss}}$ , the missing energy calculated with all available  
 2666 information, and Calorimeter  $E_T^{\text{miss}}$ , the missing energy calculated using only  
 2667 information available at the calorimeter which approximates the missing energy  
 2668 available at the trigger. The short lifetime sample has significantly greater  $E_T^{\text{miss}}$   
 2669 and Calorimeter  $E_T^{\text{miss}}$  than the stable sample as expected. For the stable sam-  
 2670 ple, a small fraction of events with very large  $E_T^{\text{miss}}$  (about 5%) migrate into the  
 2671 bin with very small Calorimeter  $E_T^{\text{miss}}$  because the  $E_T^{\text{miss}}$  produced by a charged  
 2672 R-Hadron track opposite a neutral R-Hadron track does not contribute any miss-  
 2673 ing energy in the calorimeters.

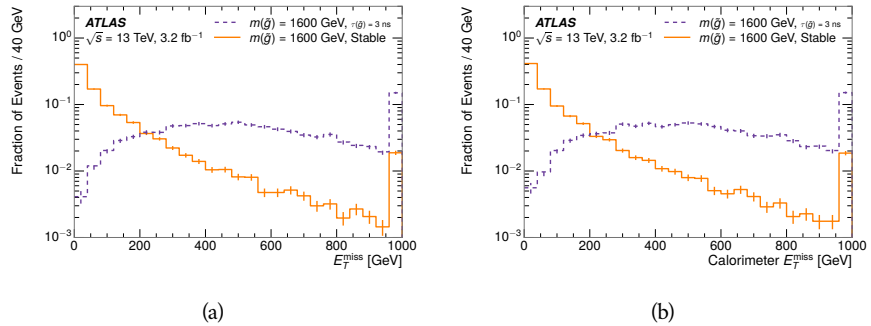


Figure 66: The distribution of (a)  $E_T^{\text{miss}}$  and (b) Calorimeter  $E_T^{\text{miss}}$  for simulated signal events before the trigger requirement.

2674 So, either case to some extent relies on kinematic degrees of freedom to pro-  
 2675 duce missing energy, as the pair-produced LLPs tend to balance each other in  
 2676 the transverse plain. That balance results in a relatively low efficiency for long-  
 2677 lifetime particles, roughly 40%, and efficiencies between 65% and 95% for shorter  
 2678 lifetimes depending on both the mass and the lifetime. For long lifetimes in par-  
 2679 ticular, the presence of ISR is important in providing an imbalance in the trans-  
 2680 verse plane, and is an important aspect of modeling the selection efficiency for  
 2681 R-Hadron events.

2682 The missing energy trigger with the lowest threshold available is chosen for  
 2683 this selection in order to maximize the trigger efficiency. During 2015 data col-  
 2684 lection this was the HLT\_xe70 trigger, which used a 50 GeV threshold on miss-  
 2685 ing energy at LVL1 and a 70 GeV threshold on missing energy at the HLT. These  
 2686 formation of the trigger decision for missing energy was discussed in more detail  
 2687 in Section 6.6.

## 2688 11.2 KINEMATICS AND ISOLATION

2689 After the trigger requirement, each event is required to have a primary vertex  
 2690 reconstructed from at least two well-measured tracks in the inner detector, each  
 2691 with  $p_T > 400$  MeV. If more than one such vertex exists, the primary vertex  
 2692 is taken to be the one with the largest summed track momentum for all tracks  
 2693 associated to that vertex. The offline reconstructed  $E_T^{\text{miss}}$  is required to be above  
 2694 130 GeV to additionally reject SM backgrounds. The transverse missing energy  
 2695 is calculated using fully reconstructed and calibrated offline objects, as described  
 2696 in Section 7.5. In particular the  $E_T^{\text{miss}}$  definition in this selection uses jets recon-  
 2697 structed with the anti- $k_t$  algorithm with radius  $R = 0.4$  from clusters of energy  
 2698 in the calorimeter (Section 7.4) and with  $p_T > 20$  GeV, as well as reconstructed  
 2699 muons, electrons, and tracks not identified as another object type.

2700 The  $E_T^{\text{miss}}$  distributions are shown for data and a few simulated signals in Fig-  
 2701 ure 67, after the trigger requirement. The cut placed at 130 GeV is 95% effi-  
 2702 cient for metastable and 90% efficient for stable particles, after the trigger re-  
 2703 quirement, because of the missing energy generating mechanisms discussed pre-  
 2704 viously. The distribution of data in this figure and subsequent figures in this sec-  
 2705 tion can be interpreted as the distribution of backgrounds, as any signal contam-  
 2706 ination would be negligible if present at these early stages of the selection (prior  
 2707 to the final requirement on ionization). The background falls rapidly with miss-  
 2708 ing energy, motivating the direct requirement on  $E_T^{\text{miss}}$  for the signal region. Al-  
 2709 though a tighter requirement than the specified value of 130 GeV would seem to  
 2710 increase the search potential from these early distributions, other requirements  
 2711 are more optimal when taken as a whole. The specific values for each require-  
 2712 ment in signal region were optimized considering the increase in discovery reach  
 2713 for tightening the requirement on each discriminating variable. **NOTE: If space**  
**2714 and time permit, I will add a whole section about signal region optimiza-**  
**2715 tion..**

2716 It is typically the practice for searches for new physics on ATLAS to place an  
 2717 offline requirement on the triggering variable that is sufficiently tight to guar-

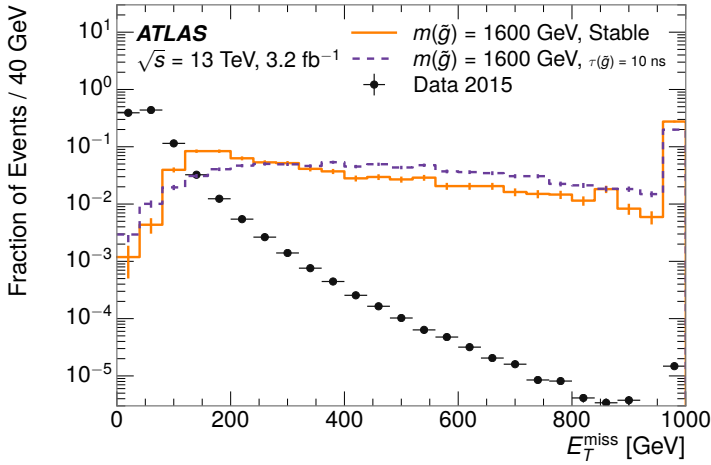


Figure 67: The distribution of  $E_T^{\text{miss}}$  for data and simulated signal events, after the trigger requirement.

2718 antee that the event would pass the trigger. Such a tight requirement makes the  
 2719 uncertainty on the trigger efficiency of the simulation negligible, as modeling the  
 2720 regime where the trigger is only partially efficient can be difficult. In this analy-  
 2721 sis, however, because of the atypical interactions of R-Hadrons with the tracker  
 2722 and the calorimeter, the offline requirement on  $E_T^{\text{miss}}$  is not sufficient to guar-  
 2723 antee a 100% trigger efficiency even at large values, as can be seen in Figure 68.  
 2724 This figure shows the efficiency for passing the HLT\_xe70 trigger as a function  
 2725 of the requirement on  $E_T^{\text{miss}}$ , which plateaus to roughly 85% even at large values.  
 2726 This plateau does not reach 100% because events which have large offline miss-  
 2727 ing energy from a neutral R-Hadron produced opposite of a charged R-Hadron  
 2728 can have low missing energy in the calorimeters. The Calorimeter  $E_T^{\text{miss}}$ , on the  
 2729 other hand, does not have this effect and reaches 100% efficiency at large values  
 2730 because it is the quantity that directly corresponds to the trigger threshold. In  
 2731 both cases the efficiency of triggering is greater for the short lifetime sample be-  
 2732 cause the late decays to hadrons and LSPs produce an imbalance in the calorime-  
 2733 ters even though they may not be reconstructed offline as tracks or jets. For this  
 2734 reason, the requirement on  $E_T^{\text{miss}}$  is determined by optimizing the background  
 2735 rejection even though it corresponds to a value of trigger efficiency significantly  
 2736 below 1.0.

2737 Potential signal events are then required to have at least one candidate LLP  
 2738 track. Although the LLPs are produced in pairs, many models do not consistently  
 2739 yield two charged particles. For example, in the R-Hadron model highlighted  
 2740 here, only 20% of events have two charged R-Hadrons while 47% of events have  
 2741 just one. A signal region requiring two charged candidates could be a powerful  
 2742 improvement in background rejection for a larger dataset, but it is not consid-  
 2743 ered in this version of the analysis as it was found to be unnecessary to reject the  
 2744 majority of backgrounds.

2745 For a track to be selected as a candidate, it must have  $p_T > 50 \text{ GeV}$  and pass  
 2746 basic quality requirements. The track must be associated to the primary vertex.

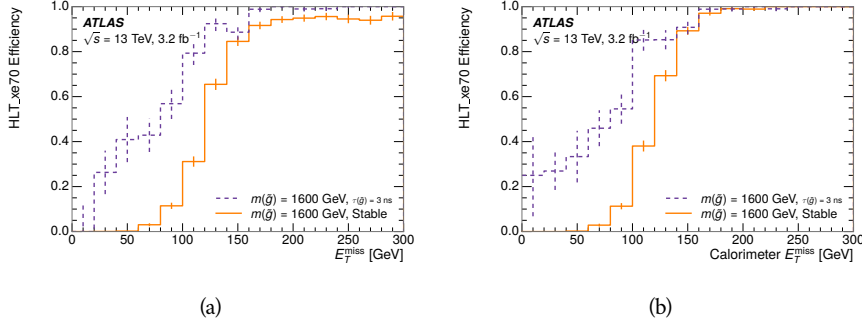


Figure 68: The trigger efficiency for the HLT\_xe70 trigger requirement as a function of (a)  $E_T^{\text{miss}}$  and (b) Calorimeter  $E_T^{\text{miss}}$  for simulated signal events.

It must also have at least seven clusters in the silicon layers in the inner detector to ensure an accurate measurement of momentum. Those clusters must include one in the innermost layer if the extrapolated track is expected to pass through that layer. And to ensure a reliable measurement of ionization, the track is required to have at least two clusters in the pixel detector that provide a measurement of  $dE/dx$ .

At this point in the selection, there is a significant high-ionization background from multiple tracks that significantly overlap in the inner detector. Previous version of this analysis have rejected these overlaps by an explicit overlap rejection between pairs of fully reconstructed tracks, typically by requiring no additional tracks within a cone around the candidate. This technique, however, fails to remove the background from tracks that overlap so precisely that the tracks cannot be separately resolved, which can be produced in very collimated photon conversions or decays of pions.

A new method, added in Run 2, identifies cluster shapes that are likely formed by multiple particles based on a neural network classification algorithm. The number of clusters that are classified this way in the pixel detector for a given track is called  $N_{\text{split}}$ . As the shape of clusters requires significantly less spatial separation to identify overlaps than it does to reconstruct two fully resolved tracks, this variable is more effective at rejecting backgrounds from overlaps. Figure 69 shows the dependence of ionization on  $N_{\text{split}}$ ; as  $N_{\text{split}}$  increases the most probable value of  $dE/dx$  grows significantly up to twice the expected value when  $N_{\text{split}} = 4$ .

This requirement is very successful in reducing the long positive tail of the  $dE/dx$  distributions, as can be seen in Figure 70. Comparing the distribution for “baseline tracks”, tracks with only the above requirements on clusters applied and before the requirement on  $N_{\text{split}}$ , to the distribution with  $N_{\text{split}} = 0$ , it is clear that the fraction of tracks with large  $dE/dx$  is reduced by several orders of magnitude. The tracks without split hits are very close to the  $dE/dx$  distribution of identified muons, which are extremely well isolated on average. Figure 70 also includes the distribution of  $dE/dx$  in an example signal simulation to demonstrate how effective  $dE/dx$  is as a discriminating variable with this isolation applied. The background falls rapidly for  $dE/dx > 1.8 \text{ MeVg}^{-1}\text{cm}^2$

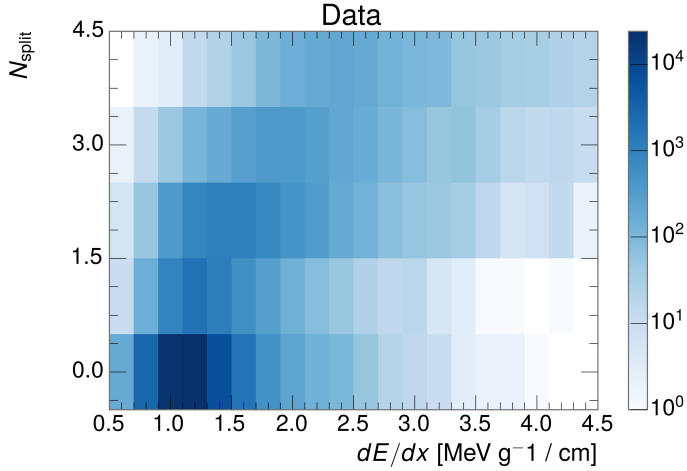


Figure 69: The dependence of  $dE/dx$  on  $N_{\text{split}}$  in data after basic track hit requirements have been applied.

2780 while the majority of the signal, approximately 90% depending on the mass, falls  
 2781 above that threshold. Over 90% of [LLP](#) tracks in simulated signal events pass the  
 2782  $N_{\text{split}}$ -based isolation requirement.

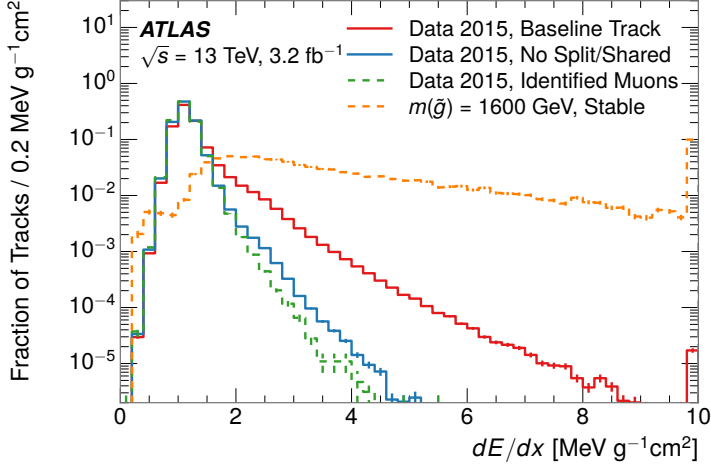


Figure 70: The distribution of  $dE/dx$  with various selections applied in data and simulated signal events.

2783 A few additional kinematic requirements are imposed to help reduce [SM](#) back-  
 2784 grounds. The momentum of the candidate track must be at least 150 GeV, and  
 2785 the uncertainty on that measurement must be less than 50%. The distribution of  
 2786 momentum is shown in Figure 71 for tracks in data and simulated signal events  
 2787 after the previously discussed requirements on clusters, transverse momentum,  
 2788 and isolation have been imposed. The signal particles are much harder on aver-

age than their backgrounds because of the high energy interactions required to produce them. The transverse mass,  $M_T$ , defined as

$$M_T = \sqrt{2p_T E_T^{\text{miss}}(1 - \cos(\Delta\phi(E_T^{\text{miss}}, \text{track})))} \quad (15)$$

estimates the mass of a decay of to a single charged particle and an undetected particle and is required to be greater than 130 GeV to reject contributions from the decay of W bosons. Figure 72 shows the distribution of  $M_T$  for data and simulated signal events. The signal is distributed over a wide range of  $M_T$ , with about 90% above the threshold value of 130 GeV. The data shows a dual-peaked structure, where the first peak comes from W boson decays and the second peak is a kinematic shaping from the requirements on  $E_T^{\text{miss}}$  and the track  $p_T$  in dijet events.

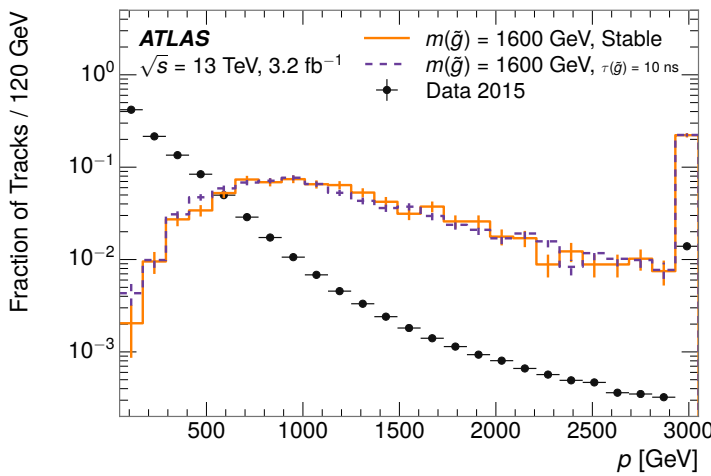


Figure 71: The distribution of track momentum for data and simulated signal events, after previous selection requirements have been applied.

### 11.3 PARTICLE SPECIES REJECTION

The amount of ionization deposited by particles with low mass and high momentum has a large positive tail [7], so backgrounds can be formed by a wide variety of SM processes when various charged particles have a few randomly large deposits of energy in the pixel detector. Those backgrounds can be additionally reduced by targeting other interactions with the detector where they are expected to have different behavior than R-Hadrons. The interactions with the detector depend on the types of particles produced rather than the processes which produce them, so this search forms a series of rejections to remove backgrounds from individual particle species. These rejections focus on using additional features of the event, other than the kinematics of the candidate track, as they can provide a powerful source of background rejection with very high signal efficiency. However, the lifetime of an R-Hadron can significantly change its

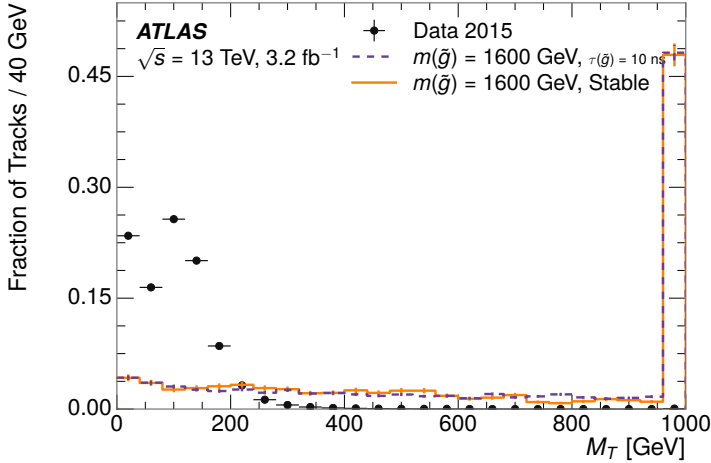


Figure 72: The distribution of  $M_T$  for data and simulated signal events, after previous selection requirements have been applied.

detector characteristics, as discussed in Section 10.1.2. To accommodate these differences, the SM rejections defined in this section are split to form two signal regions, one for long-lifetimes particles, the stable region ( $50 \leq \tau[\text{ns}] < \infty \text{ ns}$ ), and one for intermediate lifetime particles, the metastable region ( $0.4 < \tau[\text{ns}] < 50$ ).

Jets can be very effectively rejected by considering the larger-scale isolation of the candidate track. In this case the isolation focuses on the production of nearby particles as a jet-veto, rather than the isolation from overlapping tracks based on  $N_{\text{split}}$  that was used to reduce high-ionization backgrounds. As explained in Section 10.1, the fragmentation process which produces an R-Hadron is very hard and thus is not expected to produce additional particles with a summed momentum of more than 5 GeV. The jet-veto uses the summed momentum of tracks with a cone of  $\Delta R < 0.25$ , referred to as  $p_T^{\text{Cone}}$ , which is shown in Figure 73 for data and simulated signal events. In the data this value has a peak at zero from isolated tracks such as leptons, and a long tail from jets which contains as much as 80% of the background above 20 GeV at this stage of the selection. In signal events  $p_T^{\text{Cone}}$  is strongly peaked at zero and significantly less than 1% of signal events have  $p_T^{\text{Cone}}$  above 20 GeV. This makes a requirement of  $p_T^{\text{Cone}} < 20 \text{ GeV}$  a very effective method to reject background without losing signal efficiency. For the stable signal region, this cut is further tightened to  $p_T^{\text{Cone}} < 5 \text{ GeV}$  as it is the most effective variable remaining to extend the search reach for long lifetimes.

Even for fully isolated particles, there are additional methods to reject each type of particle using information in the muon system and calorimeters. Muons can be identified very reliably using the tracks in the muon system, as described in Section 7.3. For intermediate lifetimes the LLPs do not survive long enough to reach the muon system, and so muons are vetoed by rejecting tracks that associate to a muon with medium muon identification requirements (Section 7.3). For longer lifetimes, this rejection is not applied because LLPs which reach the

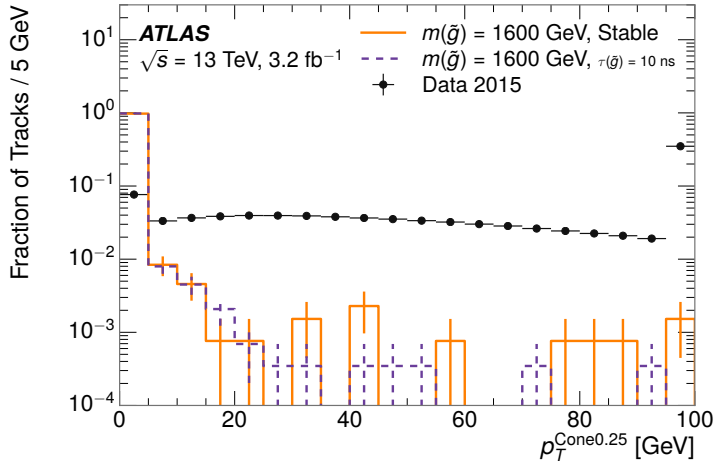


Figure 73: The distribution of summed tracked momentum within a cone of  $\Delta R < 0.25$  around the candidate track for data and simulated signal events, after previous selection requirements have been applied.

muon system can be identified as muons as often as 30% of the time in simulated samples.

Calorimeter-based particle rejection relies on the expected small deposits of energy from LLPs. When the lifetime is long enough to reach the calorimeter, a LLP deposits little of its energy as it traverses the material, as discussed in Section 10.1. Even when the particle does decay before the calorimeter, the majority of its energy is carried away by the LSP and not deposited in the calorimeter. In both cases the energy is expected to be distributed across the layers of the calorimeters and not peaked in just one layer. This can be quantified in terms of  $E/p$ , the ratio of calorimeter energy of a nearby jet to the track momentum, and  $f_{\text{EM}}$ , the fraction of energy in that jet within the electromagnetic calorimeter. When no jets fall within a cone of 0.05 of the particle,  $E/p$  and  $f_{\text{EM}}$  are both defined as zero.  $E/p$  is expected to be above 1.0 for typical SM particles because of calibration and the contributions from other nearby particles, as discussed in Chapter 8. At these momenta there is no significant zero fraction due to interactions with the detector or insufficient energy deposits (see Section 8.2.2).  $f_{\text{EM}}$  is peaked close to 1.0 for electrons, and distributed between 10% and 90% for hadrons.

These trends can be seen in the two dimensional distribution for signal in Figure 74 for stable and metastable (10 ns) events. The majority of R-Hadrons in both samples fall into the bin for  $E/p = 0$  and  $f_{\text{EM}} = 0$  because the majority of the time there is no associated jet. In the stable sample, when there often is an associated jet,  $E/p$  is typically still below 0.1, and the  $f_{\text{EM}}$  is predominantly under 0.8. In the metastable sample, on the other hand,  $E/p$  is larger but still typically below 0.1 because of actual jets produced during the decay. The  $f_{\text{EM}}$  is much lower on average in this case, below 0.1, because the 10 ns lifetime particles rarely decay before passing through the electromagnetic calorimeter. Figure 74 also includes simulated Z decays to electrons or tau leptons. From the decays

2869 to electrons it is clear that the majority of electrons have  $f_{\text{EM}}$  above 0.9. The  
 2870 tau decays include a variety of products. Muons can be seen in the bin where  
 2871  $E/p = 0$  and  $f_{\text{EM}} = 0$  because they do not have an associated jet. Electrons fall  
 2872 into the range where  $E/p > 1$  and  $f_{\text{EM}} > 0.9$ . Hadronic tau decays are the most  
 2873 common, and fall in the range of  $0.1 < f_{\text{EM}} < 0.9$  and  $E/p > 1.0$ .

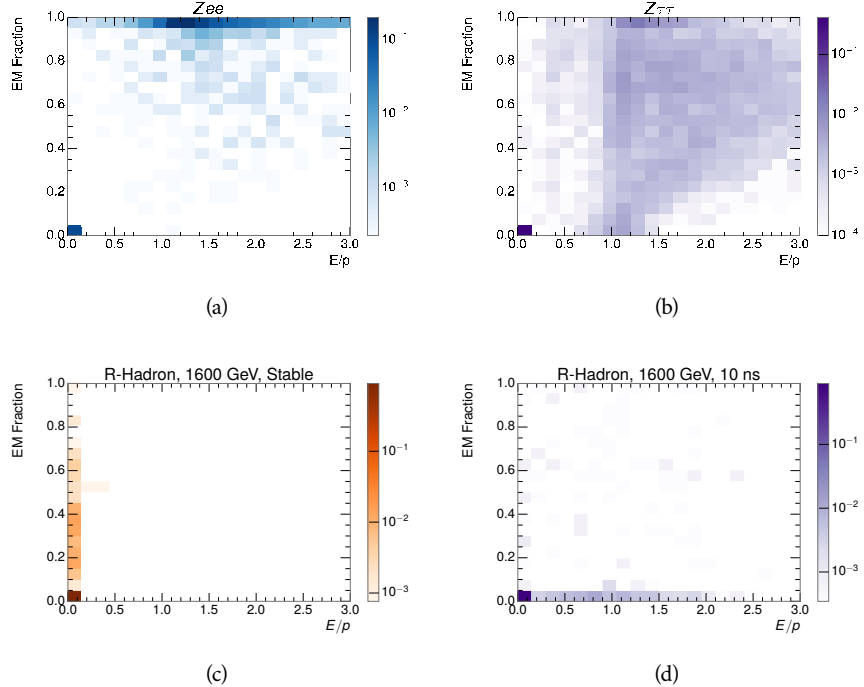


Figure 74: The normalized, two-dimensional distribution of  $E/p$  and  $f_{\text{EM}}$  for simulated  
 2874 (a)  $Z \rightarrow ee$ , (b)  $Z \rightarrow \tau\tau$ , (c) 1200 GeV Stable R-Hadron events, and (d) 1200  
 2875 GeV, 10 ns R-Hadron events.

2876 These differences motivate an electron rejection by requiring an  $f_{\text{EM}}$  below  
 2877 0.9. Similarly, isolated hadrons are rejected by requiring  $E/p < 1.0$ . These re-  
 2878 quirements combine to remove the majority of isolated electrons and hadrons  
 2879 but retain over 95% of the simulated signal across a range of masses and lifetimes.

## 2880 11.4 IONIZATION

2881 The final requirement on the candidate track is the primary discriminating vari-  
 2882 able, the ionization in the pixel detector. That ionization is measured in terms  
 2883 of  $dE/dx$ , which was shown for data and simulated signal events in Figure 70.  
 2884  $dE/dx$  is dramatically greater for the high mass signal particles than the back-  
 2885 grounds, which start to fall immediately after the minimally ionizing peak at 1.1  
 2886  $\text{MeV g}^{-1} \text{cm}^2$ . The  $dE/dx$  for candidate tracks must be greater than a pseudorapidity-  
 2887 dependent threshold, specifically  $1.80 - 0.11|\eta| + 0.17\eta^2 - 0.05\eta^3 \text{ MeV g}^{-1} \text{ cm}^{-2}$ ,  
 2888 in order to correct for an approximately 5% dependence of the MIP peak on  $\eta$ .  
 2889 The requirement was chosen as part of the signal region optimization, and man-

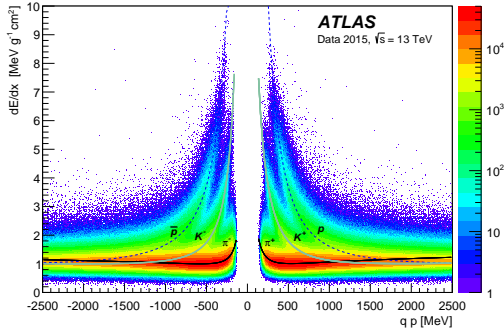


Figure 75: Two-dimensional distribution of  $dE/dx$  versus charge signed momentum ( $qp$ ) for minimum-bias tracks. The fitted distributions of the most probable values for pions, kaons and protons are superimposed.

ages to reduce the backgrounds by a factor of 100 while remaining 70-90% efficient for simulated signal events depending on the mass.

#### 11.4.1 MASS ESTIMATION

The mean value of ionization in silicon is governed by the Bethe equation and the most probable value follows a Landau-Vavilov distribution [7]. Those forms inspire a parametric description of  $dE/dx$  in terms of  $\beta\gamma$ ,

$$(dE/dx)_{MPV}(\beta\gamma) = \frac{p_1}{\beta^{p_3}} \ln(1 + [p_2 \beta\gamma]^{p_5}) - p_4 \quad (16)$$

which performs well in the range  $0.3 < \beta\gamma < 1.5$ . This range includes the expected range of  $\beta\gamma$  for the particles targeted for this search, with  $\beta\gamma \approx 2.0$  for lower mass particles ( $O(100 \text{ GeV})$ ) and up to  $\beta\gamma \approx 0.5$  for higher mass particles ( $O(1000 \text{ GeV})$ ). The parameters,  $p_i$ , are fit using a 2015 data sample of low-momentum pions, kaons, and protons as described in Ref. [83]. Figure 75 shows the two-dimensional distribution of  $dE/dx$  and momentum along with the above fitted values for  $(dE/dx)_{MPV}$ .

The above equation (16) is then numerically inverted to estimate  $\beta\gamma$  and the mass for each candidate track. In simulated signal events, the mean of this mass value reproduces the generated mass up to around 1800 GeV to within 3%, and 3% shift is applied to correct for this difference. The mass distributions prior to this correction are shown for a few stable mass points in Figure 76. The large widths of these distributions come from the high variability in energy deposits in the pixel detector as well as the uncertainty on momentum measurements at high momentum, but the means converge to the expected values.

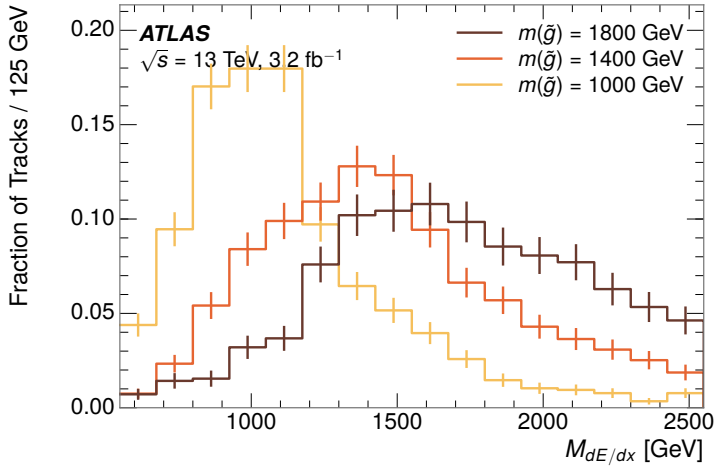


Figure 76: The distribution of mass estimated using  $dE/dx$  for simulated stable R-Hadrons with masses between 1000 and 1600 GeV.

2909 This analysis evaluates expected yields and the resulting cross sectional limits  
 2910 using windows in this mass variable. The windows are formed by fitting mass  
 2911 distributions in simulated signal events like those in Figure 76 to Gaussian distri-  
 2912 butions and taking all events that fall within  $\pm 1.4\sigma$  of the mean. As can be seen  
 2913 in Figure 76, typical values for this width are  $\sigma \approx 300 - 500$  GeV depending on  
 2914 the generated mass.

## 2915 11.5 EFFICIENCY

2916 The numbers of events passing each requirement through ionization are shown  
 2917 in Table 8 for the full 2015 dataset and a simulated 1600 GeV, 10 ns lifetime R-  
 2918 Hadron sample. The table highlights the overall acceptance  $\times$  efficiency for sig-  
 2919 nal events, which for this example is 19%. Between SM rejection and ionization,  
 2920 this signal region reduces the background of tracks which pass the kinematic  
 2921 requirements down by an additional factor of almost 2000.

2922 There is a strong dependence of this efficiency on lifetime and mass, with effi-  
 2923 ciencies dropping to under 1% at low lifetimes. Figure 77 shows the dependence  
 2924 on both mass and lifetime for all signal samples considered in this search. The  
 2925 dependence on mass is relatively slight and comes predominantly from the in-  
 2926 creasing fraction of R-Hadrons which pass the ionization cut with increasing  
 2927 mass. The trigger and  $E_T^{\text{miss}}$  requirements are most efficient for particles that  
 2928 decay before reaching the calorimeters. However, the chance of a particle to be  
 2929 reconstructed as a high-quality track decreases significantly at low lifetimes as  
 2930 the particle does not propagate sufficiently through the inner detector. These  
 2931 effects lead to a maximum in the selection efficiency for lifetimes around 10-30  
 2932 ns.

2933 The inefficiency of this signal region at short lifetimes comes almost exclu-  
 2934 sively from an acceptance effect, in that the particles do not reach the necessary

Selection	Exp. Signal Events	Observed Events in $3.2 \text{ fb}^{-1}$
Generated	$26.0 \pm 0.3$	
$E_T^{\text{miss}}$ Trigger	$24.8 \pm 0.3$ (95%)	
$E_T^{\text{miss}} > 130 \text{ GeV}$	$23.9 \pm 0.3$ (92%)	
Track Quality and $p_T > 50$	$10.7 \pm 0.2$ (41%)	368324
Isolation Requirement	$9.0 \pm 0.2$ (35%)	108079
Track $p > 150 \text{ GeV}$	$6.6 \pm 0.2$ (25%)	47463
$M_T > 130 \text{ GeV}$	$5.8 \pm 0.2$ (22%)	18746
Electron and Hadron Veto	$5.5 \pm 0.2$ (21%)	3612
Muon Veto	$5.5 \pm 0.2$ (21%)	1668
Ionization Requirement	$5.0 \pm 0.1$ (19%)	11

Table 8: The expected number of events at each level of the selection for metastable  $1600 \text{ GeV}, 10 \text{ ns}$  R-Hadrons, along with the number of events observed in data, for  $3.2 \text{ fb}^{-1}$ . The simulated yields are shown with statistical uncertainties only. The total efficiency  $\times$  acceptance is also shown for the signal.

2935 layers of the SCT. This can be seen more clearly by defining a fiducial region  
 2936 which includes events with at least one R-Hadron that is produced with non-  
 2937 zero charge,  $p_T > 50 \text{ GeV}$ ,  $p > 150 \text{ GeV}$ ,  $|\eta| < 2.5$ , and a decay distance greater  
 2938 than 37 cm in the transverse plane. At short (1 ns) lifetimes, the acceptance into  
 2939 this region is as low as 4%. Once this acceptance is accounted for, the selection  
 2940 efficiency ranges from 25% at lifetimes of 1 ns up to 45% at lifetimes of 10 ns.

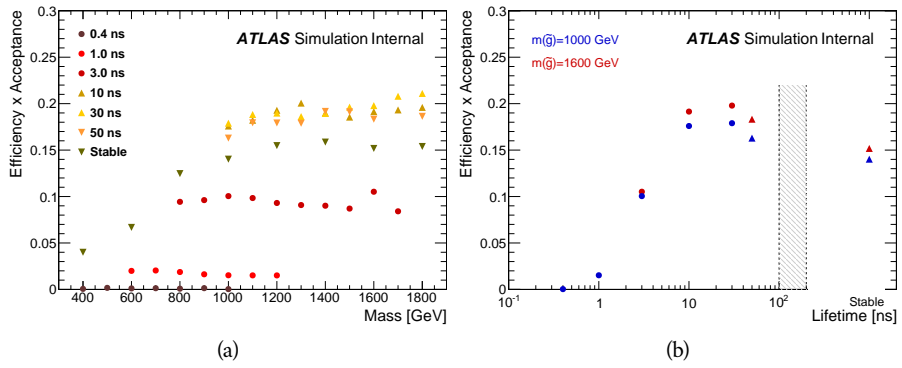


Figure 77: The acceptance  $\times$  efficiency as a function of R-Hadron (a) mass and (b) lifetime. (a) shows all of the combinations of mass and lifetime considered in this search, and (b) highlights the lifetime dependence for 1000 GeV and 1600 GeV R-Hadrons.

2941

2942 BACKGROUND ESTIMATION

---

2943 The event selection discussed in the previous section focuses on detector signa-  
 2944 tures, emphasizing a single high-momentum, highly-ionizing track. That track  
 2945 is then required to be in some way inconsistent with the expected properties  
 2946 of SM particles, with various requirements designed to reject jets, hadrons,  
 2947 electrons, and muons (Section 11.3). Therefore the background for this search comes  
 2948 entirely from reducible backgrounds that are outliers of various distributions in-  
 2949 cluding  $dE/dx$ ,  $f_{\text{EM}}$ , and  $p_T^{\text{Cone}}$ . The simulation can be tuned in various ways to  
 2950 do an excellent job of modeling the average properties of each particle type [84],  
 2951 but it is not necessarily expected to accurately reproduce outliers. For this rea-  
 2952 sons, the background estimation used for this search is estimated entirely using  
 2953 data.

## 2954 12.1 BACKGROUND SOURCES

2955 SM charged particles with lifetimes long enough to form tracks in the inner de-  
 2956 tector can be grouped into three major categories based on their detector inter-  
 2957 actions: hadrons, electrons, and muons. Every particle that enters into the back-  
 2958 ground for this search belongs to one of these types. Relatively pure samples of  
 2959 tracks from each of these types can be formed in data by inverting the various  
 2960 rejection techniques in Section 11.3. Specifically, muons are selected requiring  
 2961 medium muon identification, electrons requiring  $E/p > 1.0$  and  $f_{\text{EM}} > 0.95$ ,  
 2962 and hadrons requiring  $E/p > 1.0$  and  $f_{\text{EM}} < 0.95$ .

2963 Figure 78 shows the distributions of momentum and  $dE/dx$  for these cate-  
 2964 gories in data, after requiring the event level selection as well as the track re-  
 2965 quirements on  $p_T$ , hits, and  $N_{\text{split}}$ , as discussed in Section 11.2. Simulated signal  
 2966 events are included for reference. These distribution are only illustrative of the  
 2967 differences between types, as the rejection requirements could alter their shape.  
 2968 This is especially significant for momentum which enters directly into  $E/p$  and  
 2969 can indirectly affect muon identification. However the various types show clear  
 2970 differences in both distributions. The distributions of momentum are not nec-  
 2971 essarily expected to match between the various types because the production  
 2972 mechanisms for each type result in different kinematic distributions.  $dE/dx$  is  
 2973 also different between types because of incomplete isolation; although the re-  
 2974 quirement on  $N_{\text{split}}$  helps to reduce the contribution of nearby particles it does  
 2975 not completely remove the effect of overlaps. Muons are better isolated because  
 2976 they do not have the additional particle from hadronization present for hadrons  
 2977 and they are significantly less likely do interact with the detector and produce  
 2978 secondary particles compared to hadrons and electrons. Thus muons have the  
 2979 smallest fraction of  $dE/dx$  above the threshold of  $1.8 \text{ MeVg}^{-1}\text{cm}^2$ ; hadrons and  
 2980 electrons have a larger fraction above this threshold.

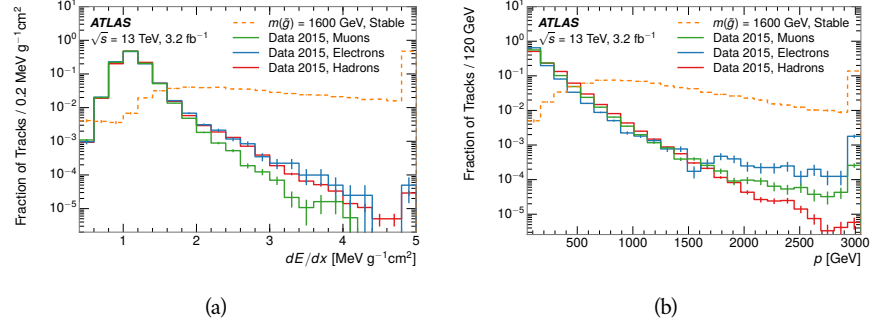


Figure 78: The distribution of (a)  $dE/dx$  and (b) momentum for tracks in data and simulated signal after requiring the event level selection and the track selection on  $p_T$ , hits, and  $N_{\text{split}}$ . Each sub-figure shows the normalized distributions for tracks classified as hadrons, electrons, and muons in data and R-Hadrons in the simulated signal.

2981 It is difficult to determine what fraction of each particle type enters into the fi-  
 2982 nal signal region. The background method will not have significant dependence  
 2983 on the relative contributions of each species, but it is useful to understand the  
 2984 differences between each when considering the various tests of the method.

## 2985 12.2 PREDICTION METHOD

2986 The data-driven background estimation relies on the independence between ion-  
 2987 ization and other kinematic variables in the event. For standard model particles  
 2988 with momenta above 50 GeV,  $dE/dx$  is not correlated with momentum; though  
 2989 there is a slight relativistic rise as momentum increases, the effect is small com-  
 2990 pared to the width of the distribution of ionization energy deposits.. So, the  
 2991 proposed method to estimate the mass distribution of the signal region is to use  
 2992 momentum from a track with low  $dE/dx$  (below the threshold value) and to com-  
 2993 bine it with a random  $dE/dx$  value from a  $dE/dx$  template. The resulting track is  
 2994 just as likely as the original, so a number of such random generations provide the  
 2995 expected distributions of momentum and ionization. These are then combined  
 2996 using the parametrization described in Section 11.4.1 to form a distribution of  
 2997 mass for the signal region.

2998 Algorithmically this method is implemented by forming two distinct Control  
 2999 Regions (**CRs**). The first **CR**, CR1, is formed by applying the entire event selec-  
 3000 tion from Chapter 11 up to the  $dE/dx$  and mass requirements. The  $dE/dx$  re-  
 3001 quirement is instead inverted for this region. Because of the independence of  
 3002  $dE/dx$ , the tracks in this control region have the same kinematic distribution  
 3003 as the tracks in the signal region, and are used to measure a two-dimensional  
 3004 template of  $p$  and  $\eta$ . The second **CR**, CR2, is formed from the event selection  
 3005 through the  $dE/dx$  requirement, but with an inverted  $E_T^{\text{miss}}$  requirement. The  
 3006 tracks in this control region are expected to have similar  $dE/dx$  distributions to  
 3007 the signal region before the ionization requirement, and so this region is used to  
 3008 measure a two-dimensional template of  $dE/dx$  and  $\eta$ .

3009     The contribution of any signal to the control regions is minimized by the in-  
 3010     verted selection requirements. Only less than 10% of simulated signal events  
 3011     have either  $dE/dx$  or  $E_T^{\text{miss}}$  below the threshold values in the original signal re-  
 3012     gion, while the backgrounds are significantly enhanced by inverting those re-  
 3013     quirements. The signal contamination is less than 1% in both control regions  
 3014     for all of the simulated masses and lifetimes considered in this analysis.

3015     With those measured templates, the shape of the mass estimation is generated  
 3016     by first selecting a random  $(p, \eta)$  combination from CR1. This momentum  
 3017     value is combined with a  $dE/dx$  value taken from the appropriate distribution  
 3018     of  $dE/dx$  for the selected  $\eta$  from CR2. The use of  $\eta$  in both random samplings  
 3019     controls for any correlation between  $p$ ,  $dE/dx$ , and  $\eta$ . Those values are then  
 3020     used to calculate a mass in the same way that is done for regular tracks in data,  
 3021     see Section 11.4.1. As this procedure includes all  $dE/dx$  values, the cut at 1.8  
 3022     MeVg $^{-1}$ cm $^2$  is then enforced to fully model the signal region. The generated  
 3023     mass distribution is then normalized by scaling the background estimate to the  
 3024     data in the region  $M < 160$  GeV, where signals of this type have already been  
 3025     excluded [68]. This normalization uses the distributions of mass generated with-  
 3026     out the ionization requirement.

3027     The statistical uncertainties on these background distributions are calculated  
 3028     by independently fluctuating each bin of the input templates according to their  
 3029     Poisson uncertainties. These fluctuations are repeated a large number of times,  
 3030     and the uncertainty on the resulting distribution is taken as the root mean square  
 3031     (RMS) deviation of the fluctuations from the average. As the procedure uses one  
 3032     million random combinations to generate the distributions, The statistical un-  
 3033     certainty from the actual random generations is negligible compared to the un-  
 3034     certainty from measuring the templates.

## 3035     12.3 VALIDATION

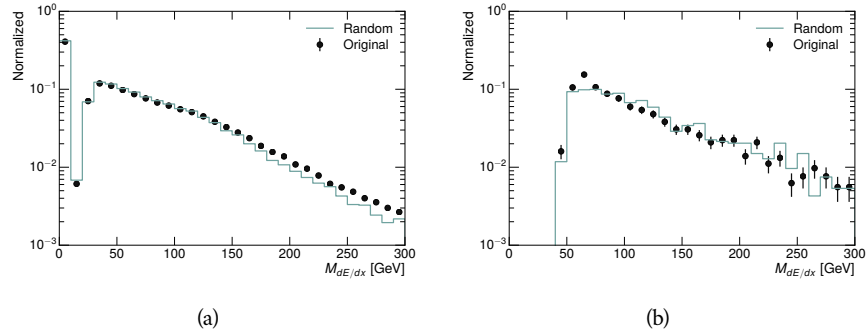
3036     The validity of the background estimation technique can be evaluated in both  
 3037     data and simulation. The underlying assumption that random combinations of  
 3038      $dE/dx$  and momentum can predict a mass distribution in an orthogonal region  
 3039     can be tested using simulated samples where concerns like multiple particle types  
 3040     can be controlled. Using the same technique in another set of signal-depleted  
 3041     regions in data then extends this confidence to the more complicated case where  
 3042     several particle species are inherently included.

### 3043     12.3.1 CLOSURE IN SIMULATION

3044     The first test of the procedure is done using a simulated sample of  $W \rightarrow \mu\nu$   
 3045     decays. These types of events provide the ingredients required to test the back-  
 3046     ground estimate,  $E_T^{\text{miss}}$  and isolated tracks, with high statistics. In this example  
 3047     there is no signal, so simulated events in the orthogonal CRs are used to estimate  
 3048     the shape of the mass distribution of the simulated events in the signal region. To  
 3049     reflect the different topology for W boson decays, the CRs use slightly modified  
 3050     definitions. In all CRs, the requirement of  $p > 150$  GeV and the SM rejection

3051 requirements are removed. Additionally, for the signal region the requirement  
 3052 on  $E_T^{\text{miss}}$  is relaxed to 30 GeV and the corresponding inverted requirement on  
 3053 CR2 is also set at 30 GeV.

3054 With these modified selections, the simulated and randomly generated distri-  
 3055 butions of  $M_{dE/dx}$  are shown in Figure 79. This figure includes the mass distri-  
 3056 butions before and after the requirement on  $dE/dx$ , which significantly shapes  
 3057 the distributions. In both cases the background estimation technique repro-  
 3058 duces the shape of  $M_{dE/dx}$  in the signal region. There is a small difference in the pos-  
 3059 itive tail of the mass distribution prior to the ionization cut, where the random  
 3060 events underestimate the fraction of tracks with mass above 150 GeV by about  
 3061 20%. After the ionization requirement, however, this discrepancy is not present  
 3062 and the two distributions agree to within statistical uncertainties.



3063 Figure 79: The distribution of  $M_{dE/dx}$  (a) before and (b) after the ionization requirement  
 3064 for tracks in simulated W boson decays and for the randomly generated back-  
 3065 ground estimate.

3066 This ability to reproduce the shape of the mass distribution in simulated events  
 3067 shows that the technique works as expected. No significant biases are acquired  
 3068 in using low  $dE/dx$  events to select kinematic templates or in using low  $E_T^{\text{miss}}$   
 3069 events to select ionization templates, as either would result in a mismodeling of  
 the shape of the mass distribution. The simulated events contain only one par-  
 ticle type, however, so this test only establishes that the technique works well  
 when the the CRs are populated by exactly the same species.

### 3070 12.3.2 VALIDATION REGION IN DATA

3071 The second test of the background estimate is performed using data in an or-  
 3072 thogonal validation region. The validation region, and the corresponding CRs,  
 3073 are formed using the same selection requirements as in the nominal method but  
 3074 with a modified requirement on momentum,  $50 < p[\text{GeV}] < 150$ . This allows  
 3075 the technique to be checked in a region with very similar properties but where  
 3076 the signal is depleted, as the majority of the signal has momentum above 150  
 3077 GeV while the backgrounds are enhanced below that threshold. Any biases on  
 3078 the particle composition of the CRs for the signal region will be reflected in the  
 3079 CRs used to estimate the mass distribution in the validation region.

3080     Figure 80 shows the measured and randomly generated mass distributions for  
 3081 data before and after the ionization requirement. The background estimate does  
 3082 an excellent job of modeling the actual background before the ionization require-  
 3083 ment, with good agreement to within the statistical uncertainties out to the limit  
 3084 of the mass distribution. There are very few events in the validation region after  
 3085 the ionization requirement, but the few observed events are consistent with the  
 3086 background prediction. The good agreement in this validation region provides  
 3087 a confirmation that the technique works even in the full-complexity case with  
 3088 multiple particle types entering the distributions. Any bias from changes in par-  
 3089 ticle composition between regions is small compared to statistical uncertainties.

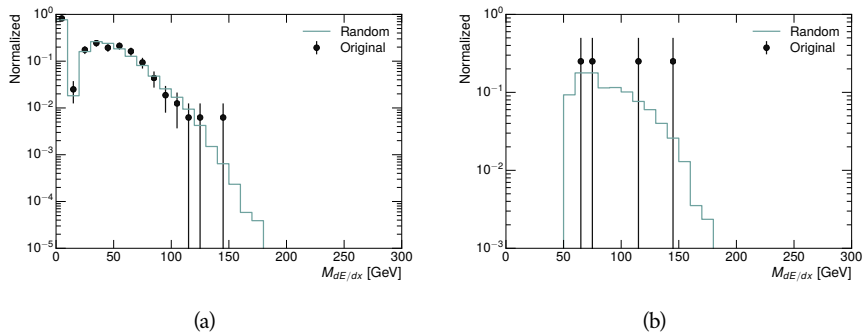


Figure 80: The distribution of  $M_{dE/dx}$  (a) before and (b) after the ionization require-  
 ment for tracks in the validation region and for the randomly generated back-  
 ground estimate.



3090

3091 SYSTEMATIC UNCERTAINTIES AND RESULTS

---

## 3092 13.1 SYSTEMATIC UNCERTAINTIES

3093 A number of systematic uncertainties affect the interpretation of the results of  
 3094 the search. These uncertainties can broken down into two major categories,  
 3095 those which affect the estimate of the background using data and those which  
 3096 affect the measurement of the signal yield estimated with simulated events. The  
 3097 total measured systematic uncertainties are 7% for the background estimation  
 3098 and approximately 32% for the signal yield depending on lifetime. These system-  
 3099atic uncertainties are expected to be small compared to the statistical fluctuations  
 3100 of the measured yields so that measured cross-sectional limits will be dominated  
 3101 by statistical uncertainties. The following sections describe each source of sys-  
 3102 tematic uncertainty for each of the two types.

## 3103 13.1.1 BACKGROUND ESTIMATE

3104 The systematic uncertainties on the background estimate come primarily from  
 3105 considering alternative methods for generating the background distributions.  
 3106 These uncertainties are small compared to the statistical uncertainties on the  
 3107 background estimate which come from the limited statistics in measuring the  
 3108 template distributions, as described in Section 12.2. They are summarized in  
 3109 Table 9.

Source of Uncertainty:	Value [%]
Analytic Description of $dE/dx$	4.0
Muon Fraction (Stable Region only)	3.0
IBL Ionization Correction	3.8
Normalization	3.0
Total (Metastable Region):	6.3
Total (Stable Region):	7.0

Table 9: A summary of the sources of systematic uncertainty for the data-driven background in the signal region. If the uncertainty depends on the mass, the maximum values are reported.

3110 13.1.1.1 ANALYTIC DESCRIPTION OF  $DE/DX$ 

3111 The background estimate uses a binned template distribution to estimate the  
 3112  $dE/dx$  of tracks in the signal region, as described in Section 12.2. It is also possi-

ble to fit that measured distribution to a functional form to help smooth the distribution in the tails of  $dE/dx$  where the template is driven by a small number of tracks. Both Landau convolved with a Gaussian and Crystal Ball functions are considered as the functional form and used to re-estimate the background distribution. The deviations compared to the nominal method are found to be 4%, and this is taken as a systematic uncertainty to cover the inability carefully predict the contribution from the long tail of  $dE/dx$  where there are few measurements available in data.

#### 3121 13.1.1.2 MUON FRACTION

3122 The stable region of the analysis explicitly includes tracks identified as muons,  
 3123 which have a known difference in their  $dE/dx$  distributions compared to non-  
 3124 muon tracks (Section 12.1). To account for a difference in muon fraction be-  
 3125 tween the background region and the signal region for this selection, the  $dE/dx$   
 3126 templates for muons and non-muons are measured separately and then the rel-  
 3127 ative fraction of each is varied in the random generation. The muon fraction  
 3128 is varied by its statistical uncertainty and the resulting difference of 3% in back-  
 3129 ground yield is taken as the systematic uncertainty.

#### 3130 13.1.1.3 IBL CORRECTIONS

3131 The IBL, described in Section 6.3.1, received a significant dose of radiation during  
 3132 the data collection in 2015. The irradiation can cause a drift in the frontend  
 3133 electronics and thus alter the  $dE/dx$  measurement which includes the ToT output  
 3134 by the IBL. These effects are corrected for in the nominal analysis by scaling the  
 3135  $dE/dx$  measurements by a constant factor derived for each run to match the  
 3136 average  $dE/dx$  value to a reference run where the IBL was known to be stable  
 3137 to this effect. However, this corrective factor does not account for inter-run  
 3138 variations. To account for this potential drift of  $dE/dx$ , the correction procedure  
 3139 is repeated by varying the corrections up and down by the maximal run-to-run  
 3140 variation from the full data-taking period, which results in an uncertainty of  
 3141 3.8%.

#### 3142 13.1.1.4 NORMALIZATION

3143 As described in Section 12.2, the generated distribution of masses is normalized  
 3144 in a shoulder region ( $M < 160$  GeV) where signals have been excluded by pre-  
 3145 vious analyses. That normalization factor is varied by its statistical uncertainty  
 3146 and the resulting fluctuation in the mass distribution of 3% is taken as a system-  
 3147 atic uncertainty on the background estimate.

#### 3148 13.1.2 SIGNAL YIELD

3149 The systematic uncertainties on the signal yield can be divided into three cate-  
 3150 gories; those on the simulation process, those on the modeling of the detector  
 3151 efficiency or calibration, and those affecting the overall signal yield. They are  
 3152 summarized in Table 9. The largest uncertainty comes from the uncertainty on

3153 the production cross section for gluinos, which is the dominant systematic un-  
 3154 certainty in this analysis.

Source of Uncertainty	-[%]	+[%]
ISR Modeling (Metastable Region)	1.5	1.5
ISR Modeling (Stable Region)	14	14
Pile-up Reweighting	1.1	1.1
Trigger Efficiency Reweighting	0.9	0.9
$E_T^{\text{miss}}$ Scale	1.1	2.2
Ionization Parametrization	7.1	0
Momentum Parametrization	0.3	0.0
Electron Rejection	0.0	0.0
Hadron Rejection	0.0	0.0
$\mu$ Identification	4.3	4.3
Luminosity	5	5
Signal size uncertainty	28	28
Total (Metastable Region)	30	29
Total (Stable Region)	33	32

Table 10: A summary of the sources of systematic uncertainty for the simulated signal yield. The uncertainty depends on the mass and lifetime, and the maximum negative and positive values are reported in the table.

### 3155 13.1.2.1 ISR MODELING

3156 As discussed in Section 10.2, MadGraph is expected to reproduce the distribution  
 3157 of ISR in signal events more accurately than the nominal Pythia samples. The  
 3158 analysis reweights the distribution of ISR in the simulated signal events to match  
 3159 the distribution found in generated MadGraph samples. This has an effect on the  
 3160 selection efficiency in the signal samples, where ISR contributes to the generation  
 3161 of  $E_T^{\text{miss}}$ . To account for the potential inaccuracy on the simulation of ISR at high  
 3162 energies, half of the difference between the signal efficiency with the reweighted  
 3163 distribution and the original distribution is taken as a systematic uncertainty.

### 3164 13.1.2.2 PILEUP REWEIGHTING

3165 The simulated events were generated prior to data collection with an estimate of  
 3166 the average number of interactions per bunch crossing. This estimate does not  
 3167 match the value of pileup during actual data collection, but a large fraction of the  
 3168 simulated events would be discarded in order to match the distribution in data.  
 3169 Therefore the simulated signal events are not reweighted for pileup by default  
 3170 in the analysis. The effect of the pileup on signal efficiency is not expected to  
 3171 depend on the mass or lifetime of the generated signal events, which allows all

3172 of the generated signal events to be used together to assess the pileup dependence.  
 3173 To account for the potential effect of the difference in the number of interactions  
 3174 per bunch crossing between data and simulation, the difference in yield between  
 3175 the nominal signal events and the reweighted events averaged over all masses  
 3176 and lifetimes is taken as a systematic uncertainty on the yield for each mass and  
 3177 lifetime (1.1%).

### 3178 13.1.2.3 TRIGGER EFFICIENCY REWEIGHTING

3179 As described in Section 11.2, the selection for this analysis does not require a suf-  
 3180 ficiently large value of  $E_T^{\text{miss}}$  to be above the plateau of trigger efficiency. There-  
 3181 fore, some signal events which would otherwise pass the event selection can be  
 3182 excluded because of the trigger requirement. These effects can be difficult to es-  
 3183 timate in simulation, and thus are constrained by comparing data and simulated  
 3184 events in an alternative W boson region which uses decays to muons to find a rel-  
 3185 atively pure sample of events with missing energy. The trigger efficiency for data  
 3186 and simulated W events are shown in Figure 81. The comparison between data  
 3187 and MC in this region constrains the simulation of the trigger efficiency. The  
 3188 simulated signal events are reweighted by the ratio of data to simulation in the  
 3189 W boson decays, while the difference between the data and simulation in those  
 3190 decays is taken as a systematic uncertainty. This results in an uncertainty of only  
 3191 0.9% as the majority of events are well above the plateau and the disagreement  
 3192 between data and simulation is small even below that plateau.

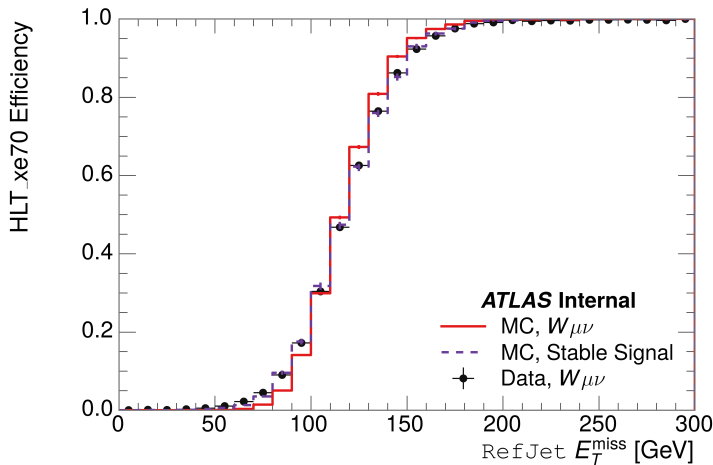


Figure 81: The trigger efficiency for the HLT\_xe70 trigger requirement as a function of Calorimeter  $E_T^{\text{miss}}$  for simulated data events with a W boson selection. Simulated signal events and simulated W boson events are also included.

### 3193 13.1.2.4 MISSING TRANSVERSE MOMENTUM SCALE

3194 The ATLAS Combined Performance (CP) group provides a default recommenda-  
 3195 tion for systematic variations of jets and missing energy (**note: I'm not quite**  
 3196 **sure what to cite for this - I don't see any papers from the jet/met group**

Systematic Variation	-[%]	+[%]
JET_GroupedNP_1	-0.7	1.3
JET_GroupedNP_2	-0.7	1.2
JET_GroupedNP_3	-0.5	1.3

Table 11: Example of the contributing systematic variations to the total systematic for the  $E_T^{\text{miss}}$  Scale, as measured in a 1200 GeV, Stable R-Hadron signal sample.

3197 **after this was implemented).** These variations enter into this analysis only in  
 3198 the requirement on  $E_T^{\text{miss}}$ . The effect of the measured scale of  $E_T^{\text{miss}}$  is evaluated  
 3199 by varying the  $E_T^{\text{miss}}$  scale according to the one sigma variations provided by all  
 3200 **CP** recommendations on objects affecting event kinematics in simulated signal  
 3201 events. Missing energy is reconstructed from fully reconstructed objects so any  
 3202 systematic uncertainties affecting jets, muons, electrons, or the  $E_T^{\text{miss}}$  soft terms  
 3203 are included. The only non-negligible contributions found using this method are  
 3204 itemized in Table 11 for an example signal sample (1200 GeV, Stable R-Hadron),  
 3205 where the systematic is measured as the relative difference in the final signal ef-  
 3206 ficiency after applying the associated variation through the CP tools. The only  
 3207 variations that are significant are the grouped jet systematic variations, which  
 3208 combine recommended jet systematic uncertainties into linearly independent  
 3209 variations.

3210 As the peak of the reconstructed  $E_T^{\text{miss}}$  distribution in the signal is significantly  
 3211 above the current threshold for events which pass the trigger requirement, the  
 3212 effect of scale variation is expected to be small, which is consistent with the mea-  
 3213 sured systematic of approximately 2%. Events which do not pass the trigger re-  
 3214 quirement usually fail because there are no ISR jets in the event to balance the  
 3215  $R$ -hadrons' transverse momentum, so the reconstructed  $E_T^{\text{miss}}$  is low and there-  
 3216 fore also expected to be not very sensitive to scale changes.

### 3217 13.1.2.5 MOMENTUM PARAMETRIZATION

3218 The uncertainty on the signal efficiency from track momentum is calculated us-  
 3219 ing the **CP** group recommendations for tracks. In particular, only one recom-  
 3220 mended systematic variation affects track momentum, the sagitta bias for  $q/P$ .  
 3221 This uncertainty is propagated to the final selection efficiency by varying the  
 3222 track momentum by the recommended one sigma variation, and the associated  
 3223 uncertainty is found to be negligible (0.3%).

### 3224 13.1.2.6 IONIZATION REQUIREMENT

3225 The  $dE/dx$  distributions in data and simulated events have different most prob-  
 3226 able values, which is due in part to radiation effects in the detector that are not  
 3227 fully accounted for in the simulation. The difference does not affect the mass  
 3228 measurement used in this analysis, as independent calibrations are done in sim-  
 3229 ulation and in data. However, it does affect the efficiency of the high  $dE/dx$   
 3230 selection requirement. To calculate the size of the effect on the signal efficiency,

3231 the  $dE/dx$  distribution in signal simulation is scaled by a scale factor obtained  
 3232 from comparing the  $dE/dx$  distribution of inclusive tracks in data and in sim-  
 3233 ulation. The difference in efficiency for this sample with a scaled  $dE/dx$  dis-  
 3234 tribution, relative to the nominal case, is taken as a systematic uncertainty on  
 3235 signal efficiency. The uncertainty is as large as 7% for low masses and falls to a  
 3236 negligible effect for large masses.

3237 13.1.2.7 ELECTRON AND JET REJECTION

3238 The systematic uncertainty on the electron rejection is measured by varying the  
 3239 EM fraction requirement significantly, from 0.95 to 0.9. This is found to have  
 3240 a less than 0.04% effect on signal acceptance, on average, and so is completely  
 3241 negligible. Similarly, the uncertainty on jet rejection is measured by tightening  
 3242 the  $E/p$  requirement from 0.5 to 0.4. This is found to have no effect on signal  
 3243 acceptance, so again the systematic is again negligible.

3244 13.1.2.8 MUON VETO

3245 The metastable signal region requires that the candidate tracks are not identi-  
 3246 fied as medium muons because the majority of R-Hadrons in the lifetime range  
 3247 included in that region do not reach the muon spectrometers before they de-  
 3248 cay. However, the exponential tail of the R-Hadron lifetime distribution results  
 3249 in some R-Hadrons traversing the muon spectrometer. These can still fail the  
 3250 muon medium identification because they can fail on the requirement on the  
 3251 number of precision hits required to pass the loose selection because they ar-  
 3252 rive late to the muon spectrometer. This can be seen in Figure 82, which shows  
 3253 the efficiency of the muon veto as a function of  $1/\beta$ , for two simulated stable  
 3254 R-Hadron samples.

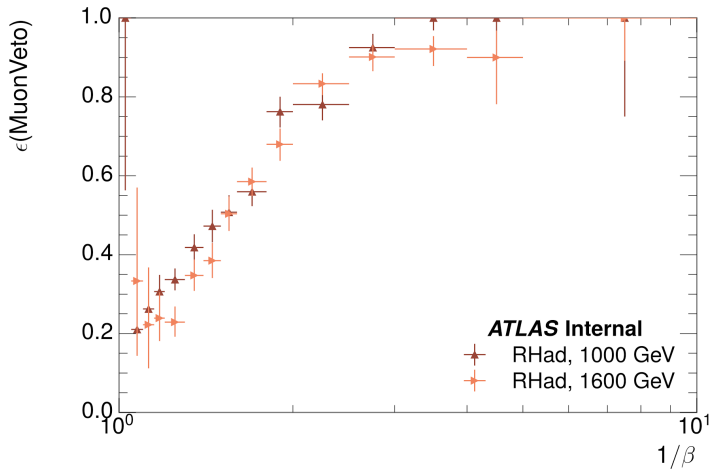


Figure 82: The efficiency of the muon veto for  $R$ -hadrons of two different masses, as a function of  $1/\beta$  for simulated R-Hadron tracks.

3255 Thus, the efficiency of the muon veto depends on the timing resolution of  
 3256 the spectrometer, so an uncertainty is applied to the signal efficiency to cover

3257 differences in timing resolution between data and simulation. First, a sample of  
 3258  $Z \rightarrow \mu\mu$  events is selected in data in which one of the muons has a late arrival  
 3259 time measured in the MDT. Then the reconstructed  $\beta$  distribution is compared  
 3260 to the distribution in simulated  $Z \rightarrow \mu\mu$  events; the difference between these  
 3261 two distributions reflects the difference in timing resolution between data and  
 3262 simulation. To emulate this difference in simulated signal events, the magnitude  
 3263 of the difference is used to scale and shift the true  $\beta$  distribution of R-Hadrons in  
 3264 simulation. Signal events are then reweighted based on this varied  $\beta$  distribution,  
 3265 and the difference in the efficiency of the muon veto selection is compared with  
 3266 the nominal and reweighted true  $\beta$  distributions. The difference in muon veto  
 3267 efficiency is taken as a systematic uncertainty of the muon veto.

3268 The comparison of reconstructed  $\beta$  between data and simulation is performed  
 3269 separately in the barrel, transition, and endcap regions of the spectrometer, and  
 3270 the reweighting of the true  $\beta$  distribution in signal is done per region. The com-  
 3271 parison of average reconstructed MDT  $\beta$  between data and simulation for the  
 3272 barrel region is shown in Figure 83 for  $Z \rightarrow \mu\mu$  events. As expected, The uncer-  
 3273 tainty is found to be negligible for R-hadrons with short lifetimes, and is only  
 3274 significant for lifetimes above 30 ns.

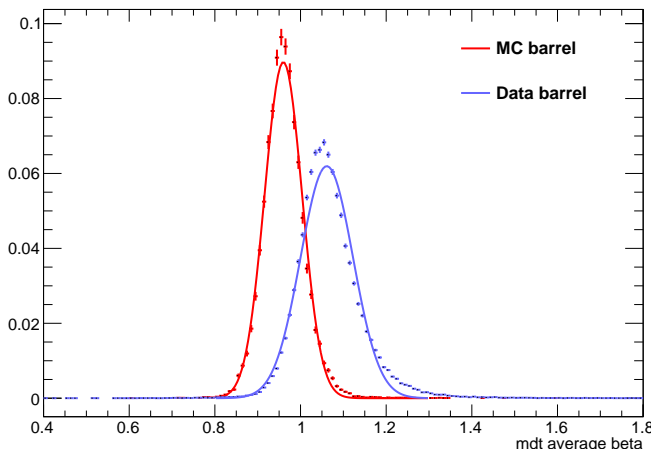


Figure 83: The average reconstructed MDT  $\beta$  distribution for  $Z \rightarrow \mu\mu$  events in which  
 one of the muons is reconstructed as a slow muon, for both data and simula-  
 tion. A gaussian fit is superimposed.

### 3275 13.1.2.9 LUMINOSITY

3276 The luminosity uncertainty is provided by a luminosity measurement on ATLAS  
 3277 and was measured to be 5% at the time of the publication of this analysis.

### 3278 13.1.2.10 SIGNAL SIZE

3279 As discussed in Section 10.2, the signal cross sections are calculated at NLO in the  
 3280 strong coupling constant with a resummation of soft-gluon emission at NLL. The  
 3281 uncertainties on those cross sections are between 14% to 28% for the R-Hadrons

Selection Region	Expected Background	Data
Stable	$17.2 \pm 2.6 \pm 1.2$	16
Metastable	$11.1 \pm 1.7 \pm 0.7$	11

Table 12: The estimated number of background events and the number of observed events in data for the specified selection regions prior to the requirement on mass. The background estimates show statistical and systematic uncertainties.

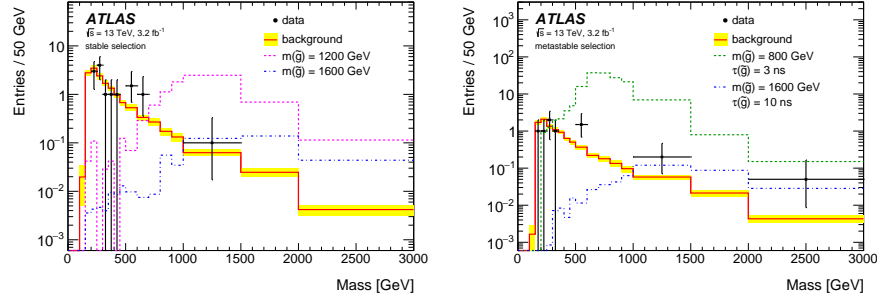


Figure 84: The observed mass distribution of events in data and the generated background distribution in (a) the stable and (b) the metastable signal region. A few example simulated signal distributions are superimposed.

3282 in the range of 400 to 1800 GeV [80, 81], where the uncertainty increases with  
3283 the mass.

### 3284 13.2 FINAL YIELDS

3285 This full analysis was performed using the  $3.2 \text{ fb}^{-1}$  from the 2015 data-taking.  
3286 Using the selections discussed in Chapter 11, sixteen events were observed in  
3287 the stable signal region and eleven events were observed in the metastable signal  
3288 region, prior to requirements on the candidate track mass. The background esti-  
3289 mate discussed in Chapter 12 predicts  $17 \pm 2.6(\text{stat}) \pm 1.2(\text{syst})$  events for the  
3290 stable region and  $11.1 \pm 1.7(\text{stat}) \pm 0.7(\text{syst})$  events for the metastable region.  
3291 These counts are summarized in Table 12.

3292 The mass estimated using  $dE/dx$  (Section 11.4.1) provides the final discrimi-  
3293 nating variable, where the signal would be expected as an excess in the falling ex-  
3294 ponential tail of the expected background. The observed distribution of masses  
3295 is shown in Figure 84, along with the predicted distribution from the background  
3296 estimate for each signal region. Both include a few example simulated signal dis-  
3297 tributions, which show the scale of an excess were the R-Hadron signals present.  
3298 There is no statistically significant evidence of an excess in the data over the back-  
3299 ground estimation. From this distribution it is clearly possible to rule out signals  
3300 with lower masses, around 1200 GeV, which have larger cross sections.

### 3301 13.3 CROSS SECTIONAL LIMITS

3302 Because there is no observed significant excess of events in the signal region, this  
 3303 analysis sets upper limits on the allowed cross section for R-Hadron production.  
 3304 These limits are set for each mass point by counting the observed events in data,  
 3305 along with the expected background and simulated signal events, in windows of  
 3306 mass. The mass windows are formed by fitting the distribution of signal events to  
 3307 a Gaussian distribution, and the window is then  $\pm 1.4\sigma$  around the center of that  
 3308 Gaussian. Two examples of the windows formed by this procedure are shown  
 3309 in Tables 13-14, for the stable and 10 ns working points. The corresponding  
 3310 counts of observed data, expected background, and simulated signal for those  
 3311 same working points are shown in Tables 15-16. Appendix B includes the mass  
 3312 windows and counts for all of the considered signal points.

$m(\tilde{g})$ [GeV]	Left Extremum [GeV]	Right Extremum [GeV]
1000	655	1349
1100	734	1455
1200	712	1631
1300	792	1737
1400	717	1926
1500	815	2117
1600	824	2122
1700	900	2274
1800	919	2344

Table 13: The left and right extremum of the mass window for each generated mass point with a 10 ns lifetime.

$m(\tilde{g})$ [GeV]	Left Extremum [GeV]	Right Extremum [GeV]
800	627	1053
1000	726	1277
1200	857	1584
1400	924	1937
1600	993	2308
1800	1004	2554

Table 14: The left and right extremum of the mass window used for each generated stable mass point.

3313 The 95% confidence level upper limits on the cross sections for a large grid of  
 3314 masses (between 800 and 1800 GeV) and lifetimes (between 0.4 and stable) are  
 3315 extracted from these counts with the  $CL_S$  method using the profile likelihood

$m(\tilde{g})$ [GeV]	Expected Signal	Expected Background	Observed Data
800	$462.83 \pm 14.86$	$1.764 \pm 0.080$	2.0
1000	$108.73 \pm 3.38$	$1.458 \pm 0.070$	1.0
1200	$31.74 \pm 0.95$	$1.137 \pm 0.060$	1.0
1400	$10.22 \pm 0.29$	$1.058 \pm 0.058$	1.0
1600	$3.07 \pm 0.09$	$0.947 \pm 0.054$	1.0
1800	$1.08 \pm 0.05$	$0.940 \pm 0.054$	1.0

Table 15: The expected number of signal events, the expected number of background events, and the observed number of events in data with their respective statistical errors within the respective mass window for each generated stable mass point

$m(\tilde{g})$ [GeV]	Expected Signal	Expected Background	Observed Data
1000	$144.48 \pm 5.14$	$1.499 \pm 0.069$	2.0
1100	$73.19 \pm 2.61$	$1.260 \pm 0.060$	2.0
1200	$41.54 \pm 1.41$	$1.456 \pm 0.067$	2.0
1300	$22.58 \pm 0.77$	$1.201 \pm 0.058$	2.0
1400	$12.70 \pm 0.42$	$1.558 \pm 0.071$	2.0
1500	$6.73 \pm 0.24$	$1.237 \pm 0.060$	2.0
1600	$3.90 \pm 0.13$	$1.201 \pm 0.058$	2.0
1700	$2.27 \pm 0.07$	$1.027 \pm 0.052$	2.0
1800	$1.34 \pm 0.04$	$1.019 \pm 0.052$	2.0

Table 16: The expected number of signal events, the expected number of background events, and the observed number of events in data with their respective statistical errors within the respective mass window for each generated mass point with a lifetime of 10 ns.

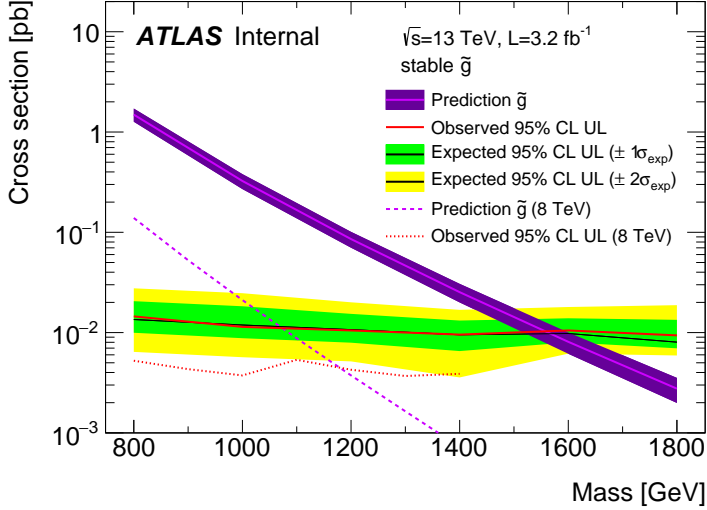


Figure 85: The observed and expected cross section limits as a function of mass for the stable simulated signal. The predicted cross section values for the corresponding signals are included.

ratio as a test statistic [85]. For this procedure, the systematic uncertainties estimated for the signal and background yields are treated as Gaussian-distributed nuisance parameters. The uncertainty on the normalization of the expected background distribution is included in the expected background events. At this point the expected cross section limit is calculated for both the metastable and stable signal region for each lifetime point, and the region with the best expected limit is selected for each lifetime. Using that procedure, the metastable region is used for lifetimes up to and including 30 ns, and the stable region for lifetimes above it.

The resulting cross-sectional upper limits are shown as a function of mass in Figure 85 and Figure 86 for each lifetime considered. The limits are interpolated linearly between each mass point, and the dependence of the limit on the mass is small as the efficiency is relatively constant for large R-Hadron masses. There is however a strong dependence on lifetime, as discussed in Section 11.5, where the probability to form a fully reconstructed track and the kinematic freedom to produce  $E_T^{\text{miss}}$  result in a local maximum in the limit at 10–30 ns. The figures also include the expected cross section for pair-produced gluino R-Hadrons for reference. For the 10 ns and stable cross section limits, both the observed limit and expected cross section for the Run 1, 8 TeV version of this analysis are included. There the cross sectional limits are lower because of the increased available luminosity, while the signal cross sections were also much lower because of the lower collision energy.

### 13.4 MASS LIMITS

The cross-sectional limits can then be used to derive a lower mass limit for gluino R-Hadrons by comparing them to the theoretically predicted production cross

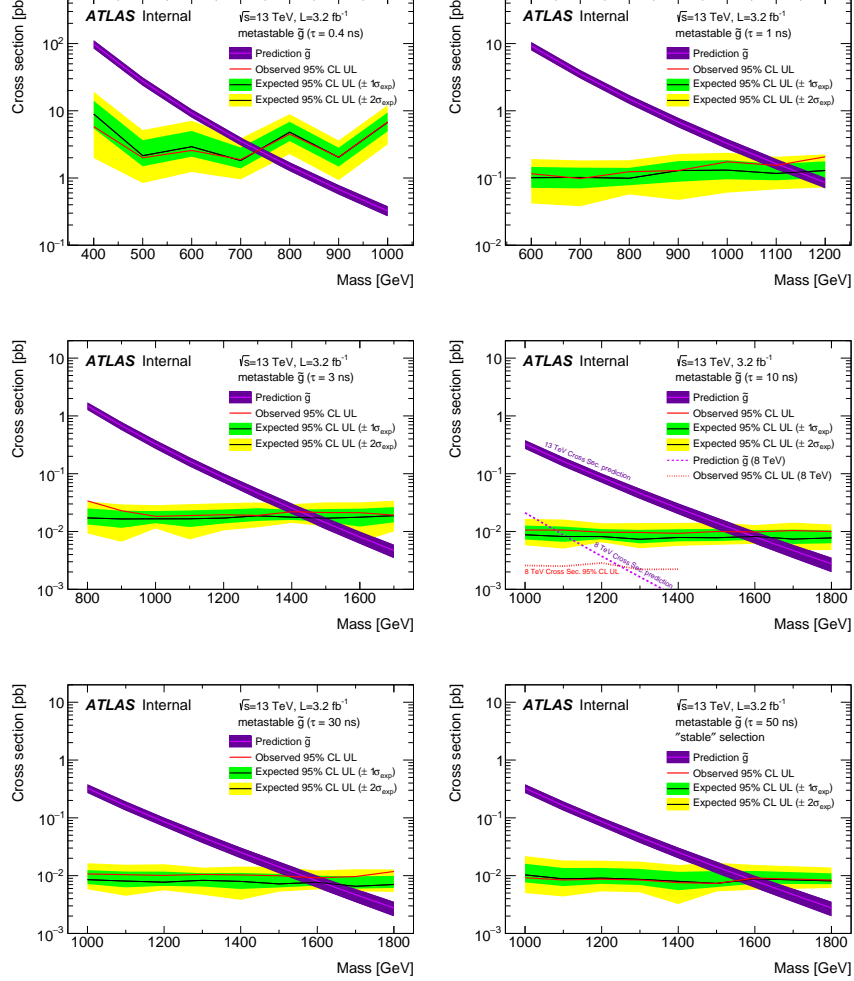


Figure 86: The observed and expected cross section limits as a function of mass for each generated lifetime. The predicted cross section values for the corresponding signals are included.

3341 sections. These mass limits range from only 740 GeV at the lowest lifetimes con-  
 3342 sidered, where the selection efficiency is very low, to up to 1580 GeV at 30 ns  
 3343 where the selection efficiency is maximized. The observed and expected mass  
 3344 limits for each lifetime point are detailed in Table 17, which also lists which se-  
 3345 lection region was used for each lifetime. These excluded range of masses as a  
 3346 function of lifetime is also shown in Figure 87. The Run 1 limits are included for  
 3347 comparison; the limits have increased by about 200 GeV on average. The search  
 3348 has also improved since the previous incarnation from Run 1 in optimizing the  
 3349 region between 30 GeV and detector-stable lifetimes by introducing the second  
 3350 signal region. The definition of the stable region prevents the significant drop  
 3351 in mass limit that occurred above 30 GeV in the Run 1 analysis.

Selection	$\tau$ [ns]	$M_{\text{obs}} > [\text{GeV}]$	$M_{\text{exp}} > [\text{GeV}]$
Metastable	0.4	740	730
"	1.0	1110	1150
"	3.0	1430	1470
"	10	1570	1600
"	30	1580	1620
Stable	50	1590	1590
"	stable	1570	1580

Table 17: The observed and expected 95% CL lower limit on mass for gluino R-Hadrons for each considered lifetime.

## 3352 13.5 CONTEXT FOR LONG-LIVED SEARCHES

3353 This search plays an important role in the current, combined [ATLAS](#) search for  
 3354 long lived particles. The mass limits provided by various [ATLAS](#) searches for  
 3355 long-lived gluino R-Hadrons can be seen in Figure 88. This search provides the  
 3356 most competitive limit for lifetimes between 3 ns up through very long lifetimes,  
 3357 where it is still competitive with dedicated searches for stable particles. The lim-  
 3358 its placed on gluino production are very similar to the limits on promptly decay-  
 3359 ing models.

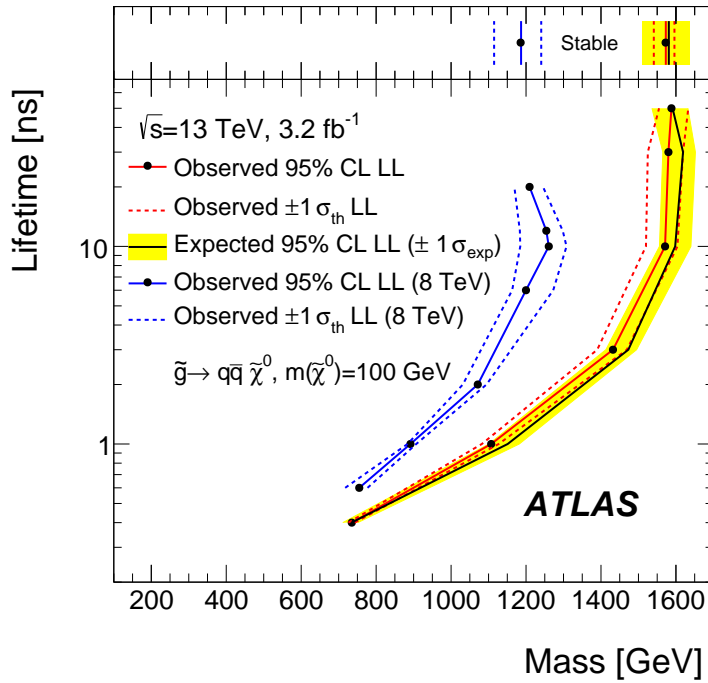


Figure 87: The excluded range of masses as a function of gluino lifetime. The expected lower limit (LL), with its experimental  $\pm 1\sigma$  band, is given with respect to the nominal theoretical cross-section. The observed 95% LL obtained at  $\sqrt{s} = 8 \text{ TeV}$  [68] is also shown for comparison.

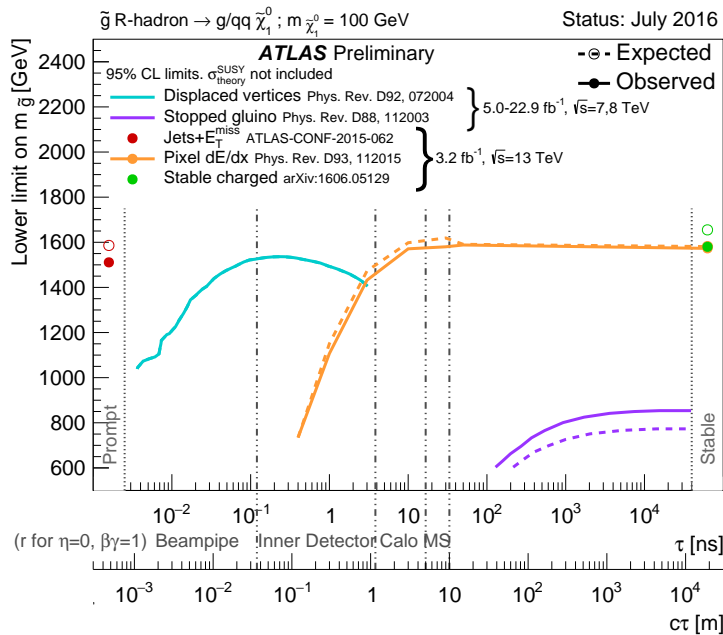


Figure 88: The constraints on the gluino mass as a function of lifetime for a split-supersymmetry model with the gluino R-Hadrons decaying into a gluon or light quarks and a neutralino with mass of 100 GeV. The solid lines indicate the observed limits, while the dashed lines indicate the expected limits. The area below the curves is excluded. The dots represent results for which the particle is assumed to be prompt or stable.



3360

## PART VI

3361

### CONCLUSIONS

3362

You can put some informational part preamble text here.



# 14

3363

## 3364 SUMMARY AND OUTLOOK

---

### 3365 14.1 SUMMARY

### 3366 14.2 OUTLOOK



3367

## PART VII

3368

## APPENDIX

3369



# A

3370

3371 INELASTIC CROSS SECTION

---



# B

3372

## 3373 EXPANDED R-HADRON YIELDS AND LIMITS

---

$m(\tilde{g})$ [GeV]	Left Extremum [GeV]	Right Extremum [GeV]
1000	682	1387
1100	763	1478
1200	801	1606
1300	809	1841
1400	861	2011
1500	920	2032
1600	952	2173
1800	1017	2422

Table 18: The left and right extremum of the mass window for each generated mass point with a 50 ns lifetime.

$m(\tilde{g})$ [GeV]	Left Extremum [GeV]	Right Extremum [GeV]
1000	689	1321
1100	746	1513
1200	788	1670
1300	860	1734
1400	833	1925
1500	852	2048
1600	833	2283
1700	946	2379
1800	869	2505

Table 19: The left and right extremum of the mass window for each generated mass point with a 30 ns lifetime.

$m(\tilde{g})$ [GeV]	Left Extremum [GeV]	Right Extremum [GeV]
1000	655	1349
1100	734	1455
1200	712	1631
1300	792	1737
1400	717	1926
1500	815	2117
1600	824	2122
1700	900	2274
1800	919	2344

Table 20: The left and right extremum of the mass window for each generated mass point with a 10 ns lifetime.

$m(\tilde{g})$ [GeV]	Left Extremum [GeV]	Right Extremum [GeV]
800	531	1065
900	576	1165
1000	610	1345
1100	635	1432
1200	663	1563
1300	620	1667
1400	742	1727
1500	761	1937
1600	573	2000
1700	621	2182

Table 21: The left and right extremum of the mass window used for each generated mass point with a lifetime of 3 ns.

$m(\tilde{g})$ [GeV]	Left Extremum [GeV]	Right Extremum [GeV]
600	411	758
700	385	876
800	486	970
900	406	987
1000	408	1136
1100	555	1196
1200	516	1378

Table 22: The left and right extremum of the mass window used for each mass point with a lifetime of 1 ns.

$m(\tilde{g})$ [GeV]	Left Extremum [GeV]	Right Extremum [GeV]
400	204	510
500	295	639
600	288	702
700	323	701
800	190	771
900	277	677
1000	249	688

Table 23: The left and right extremum of the mass window for each generated mass point with a lifetime of 0.4 ns.

$m(\tilde{g})$ [GeV]	Left Extremum [GeV]	Right Extremum [GeV]
800	627	1053
1000	726	1277
1200	857	1584
1400	924	1937
1600	993	2308
1800	1004	2554

Table 24: The left and right extremum of the mass window used for each generated stable mass point.

$m(\tilde{g})$ [GeV]	Expected Signal	Expected Background	Observed Data
1000	$131.18 \pm 6.35$	$1.803 \pm 0.081$	$1.0 \pm 1.0$
1100	$71.11 \pm 3.35$	$1.409 \pm 0.069$	$1.0 \pm 1.0$
1200	$37.18 \pm 1.75$	$1.310 \pm 0.066$	$1.0 \pm 1.0$
1300	$20.76 \pm 0.95$	$1.431 \pm 0.069$	$1.0 \pm 1.0$
1400	$12.63 \pm 0.57$	$1.273 \pm 0.065$	$1.0 \pm 1.0$
1500	$6.57 \pm 0.29$	$1.115 \pm 0.059$	$1.0 \pm 1.0$
1600	$3.56 \pm 0.16$	$1.041 \pm 0.057$	$1.0 \pm 1.0$
1800	$1.27 \pm 0.05$	$0.918 \pm 0.053$	$1.0 \pm 1.0$

Table 25: The expected number of signal events, the expected number of background events, and the observed number of events in data with their respective statistical errors within the respective mass window for each generated mass point with a lifetime of 50 ns.

$m(\tilde{g})$ [GeV]	Expected Signal	Expected Background	Observed Data
1000	$144.65 \pm 6.34$	$1.328 \pm 0.063$	$2.0 \pm 1.4$
1100	$75.28 \pm 3.27$	$1.255 \pm 0.060$	$2.0 \pm 1.4$
1200	$40.51 \pm 1.75$	$1.193 \pm 0.058$	$2.0 \pm 1.4$
1300	$20.91 \pm 0.93$	$0.997 \pm 0.051$	$2.0 \pm 1.4$
1400	$11.97 \pm 0.51$	$1.131 \pm 0.056$	$2.0 \pm 1.4$
1500	$6.81 \pm 0.28$	$1.111 \pm 0.055$	$2.0 \pm 1.4$
1600	$4.19 \pm 0.16$	$1.193 \pm 0.058$	$2.0 \pm 1.4$
1700	$2.42 \pm 0.09$	$0.963 \pm 0.050$	$2.0 \pm 1.4$
1800	$1.46 \pm 0.05$	$1.138 \pm 0.056$	$3.0 \pm 1.7$

Table 26: The expected number of signal events, the expected number of background events, and the observed number of events in data with their respective statistical errors within the respective mass window for each generated mass point with a lifetime of 30 ns.

$m(\tilde{g})$ [GeV]	Expected Signal	Expected Background	Observed Data
1000	$144.48 \pm 5.14$	$1.499 \pm 0.069$	$2.0 \pm 1.4$
1100	$73.19 \pm 2.61$	$1.260 \pm 0.060$	$2.0 \pm 1.4$
1200	$41.54 \pm 1.41$	$1.456 \pm 0.067$	$2.0 \pm 1.4$
1300	$22.58 \pm 0.77$	$1.201 \pm 0.058$	$2.0 \pm 1.4$
1400	$12.70 \pm 0.42$	$1.558 \pm 0.071$	$2.0 \pm 1.4$
1500	$6.73 \pm 0.24$	$1.237 \pm 0.060$	$2.0 \pm 1.4$
1600	$3.90 \pm 0.13$	$1.201 \pm 0.058$	$2.0 \pm 1.4$
1700	$2.27 \pm 0.07$	$1.027 \pm 0.052$	$2.0 \pm 1.4$
1800	$1.34 \pm 0.04$	$1.019 \pm 0.052$	$2.0 \pm 1.4$

Table 27: The expected number of signal events, the expected number of background events, and the observed number of events in data with their respective statistical errors within the respective mass window for each generated mass point with a lifetime of 10 ns.

$m(\tilde{g})$ [GeV]	Expected Signal	Expected Background	Observed Data
800	$362.97 \pm 14.68$	$1.841 \pm 0.080$	$5.0 \pm 2.2$
900	$169.20 \pm 6.69$	$1.710 \pm 0.076$	$3.0 \pm 1.7$
1000	$84.78 \pm 3.23$	$1.727 \pm 0.076$	$2.0 \pm 1.4$
1100	$40.06 \pm 1.60$	$1.679 \pm 0.075$	$2.0 \pm 1.4$
1200	$20.06 \pm 0.81$	$1.598 \pm 0.072$	$2.0 \pm 1.4$
1300	$10.76 \pm 0.43$	$1.851 \pm 0.080$	$2.0 \pm 1.4$
1400	$5.52 \pm 0.22$	$1.374 \pm 0.064$	$2.0 \pm 1.4$
1500	$3.16 \pm 0.13$	$1.355 \pm 0.064$	$2.0 \pm 1.4$
1600	$2.13 \pm 0.11$	$2.235 \pm 0.093$	$3.0 \pm 1.7$
1700	$1.10 \pm 0.06$	$1.995 \pm 0.085$	$2.0 \pm 1.4$

Table 28: The expected number of signal events, the expected number of background events, and the observed number of events in data with their respective statistical errors within the respective mass window for each generated mass point with a lifetime of 3 ns.

$m(\tilde{g})$ [GeV]	Expected Signal	Expected Background	Observed Data
600	$431.80 \pm 36.60$	$2.418 \pm 0.099$	$3.0 \pm 1.7$
700	$192.77 \pm 15.28$	$3.267 \pm 0.126$	$3.0 \pm 1.7$
800	$69.63 \pm 5.90$	$2.125 \pm 0.089$	$3.0 \pm 1.7$
900	$28.91 \pm 2.59$	$3.114 \pm 0.121$	$3.0 \pm 1.7$
1000	$13.64 \pm 1.22$	$3.359 \pm 0.129$	$5.0 \pm 2.2$
1100	$6.13 \pm 0.57$	$1.879 \pm 0.081$	$3.0 \pm 1.7$
1200	$3.24 \pm 0.30$	$2.387 \pm 0.098$	$5.0 \pm 2.2$

Table 29: The expected number of signal events, the expected number of background events, and the observed number of events in data with their respective statistical errors within the respective mass window for each generated mass point with a lifetime of 1 ns.

$m(\tilde{g})$ [GeV]	Expected Signal	Expected Background	Observed Data
400	$181.71 \pm 75.59$	$6.780 \pm 0.238$	$4.0 \pm 2.0$
500	$103.88 \pm 30.05$	$4.310 \pm 0.160$	$4.0 \pm 2.0$
600	$28.34 \pm 9.34$	$4.868 \pm 0.177$	$4.0 \pm 2.0$
700	$13.62 \pm 4.00$	$3.908 \pm 0.147$	$4.0 \pm 2.0$
800	$2.75 \pm 1.15$	$9.001 \pm 0.308$	$8.0 \pm 2.8$
900	$2.25 \pm 0.71$	$5.045 \pm 0.183$	$5.0 \pm 2.2$
1000	$0.34 \pm 0.19$	$6.026 \pm 0.214$	$6.0 \pm 2.4$

Table 30: The expected number of signal events, the expected number of background events, and the observed number of events in data with their respective statistical errors within the respective mass window for each generated mass point with a lifetime of p4 ns.

$m(\tilde{g})$ [GeV]	Expected Signal	Expected Background	Observed Data
800	$462.83 \pm 14.86$	$1.764 \pm 0.080$	$2.0 \pm 1.4$
1000	$108.73 \pm 3.38$	$1.458 \pm 0.070$	$1.0 \pm 1.0$
1200	$31.74 \pm 0.95$	$1.137 \pm 0.060$	$1.0 \pm 1.0$
1400	$10.22 \pm 0.29$	$1.058 \pm 0.058$	$1.0 \pm 1.0$
1600	$3.07 \pm 0.09$	$0.947 \pm 0.054$	$1.0 \pm 1.0$
1800	$1.08 \pm 0.05$	$0.940 \pm 0.054$	$1.0 \pm 1.0$

Table 31: The expected number of signal events, the expected number of background events, and the observed number of events in data with their respective statistical errors within the respective mass window for each generated stable mass point

- 3375 [1] Lyndon Evans and Philip Bryant. "LHC Machine". In: *JINST* 3 (2008), S08001.  
3376 doi: [10.1088/1748-0221/3/08/S08001](https://doi.org/10.1088/1748-0221/3/08/S08001).
- 3377 [2] C Lefevre. "LHC: the guide (English version). Guide du LHC (version anglaise)".  
3378 2009. URL: <https://cds.cern.ch/record/1165534>.
- 3379 [3] ATLAS Collaboration. "The ATLAS Experiment at the CERN Large Hadron  
3380 Collider". In: *JINST* 3 (2008), S08003. doi: [10.1088/1748-0221/3/08/S08003](https://doi.org/10.1088/1748-0221/3/08/S08003).
- 3382 [4] S. Chatrchyan et al. "The CMS experiment at the CERN LHC". In: *JINST*  
3383 3 (2008), S08004. doi: [10.1088/1748-0221/3/08/S08004](https://doi.org/10.1088/1748-0221/3/08/S08004).
- 3384 [5] A. Augusto Alves Jr. et al. "The LHCb Detector at the LHC". In: *JINST* 3  
3385 (2008), S08005. doi: [10.1088/1748-0221/3/08/S08005](https://doi.org/10.1088/1748-0221/3/08/S08005).
- 3386 [6] K. Aamodt et al. "The ALICE experiment at the CERN LHC". In: *JINST* 3  
3387 (2008), S08002. doi: [10.1088/1748-0221/3/08/S08002](https://doi.org/10.1088/1748-0221/3/08/S08002).
- 3388 [7] K. A. Olive et al. "Review of Particle Physics". In: *Chin. Phys. C* 38 (2014),  
3389 p. 090001. doi: [10.1088/1674-1137/38/9/090001](https://doi.org/10.1088/1674-1137/38/9/090001).
- 3390 [8] Daniel Froidevaux and Paris Sphicas. "General-Purpose Detectors for the  
3391 Large Hadron Collider". In: *Annual Review of Nuclear and Particle Science*  
3392 56.1 (2006), pp. 375–440. doi: [10.1146/annurev.nucl.54.070103.181209](https://doi.org/10.1146/annurev.nucl.54.070103.181209). URL: <http://dx.doi.org/10.1146/annurev.nucl.54.070103.181209>.
- 3395 [9] M Capeans, G Darbo, K Einsweiller, M Elsing, T Flick, M Garcia-Sciveres,  
3396 C Gemme, H Pernegger, O Rohne, and R Vuillermet. *ATLAS Insertable B-*  
3397 *Layer Technical Design Report*. Tech. rep. CERN-LHCC-2010-013. ATLAS-  
3398 TDR-19. 2010. URL: <https://cds.cern.ch/record/1291633>.
- 3399 [10] T. Cornelissen, M. Elsing, S. Fleischmann, W. Liebig, and E. Moyse. "Con-  
3400 cepts, Design and Implementation of the ATLAS New Tracking (NEWT)".  
3401 In: (2007). Ed. by A. Salzburger.
- 3402 [11] "Performance of the ATLAS Inner Detector Track and Vertex Reconstruc-  
3403 tion in the High Pile-Up LHC Environment". In: (2012).
- 3404 [12] ATLAS Collaboration. "A neural network clustering algorithm for the AT-  
3405 LAS silicon pixel detector". In: *JINST* 9 (2014), P09009. doi: [10.1088/1748-0221/9/09/P09009](https://doi.org/10.1088/1748-0221/9/09/P09009). arXiv: [1406.7690 \[hep-ex\]](https://arxiv.org/abs/1406.7690).
- 3407 [13] ATLAS Collaboration. "Electron reconstruction and identification efficiency  
3408 measurements with the ATLAS detector using the 2011 LHC proton–proton  
3409 collision data". In: *Eur. Phys. J. C* 74 (2014), p. 2941. doi: [10.1140/epjc/s10052-014-2941-0](https://doi.org/10.1140/epjc/s10052-014-2941-0). arXiv: [1404.2240 \[hep-ex\]](https://arxiv.org/abs/1404.2240). PERF-2013-03.

- 3411 [14] Matteo Cacciari, Gavin P. Salam, and Gregory Soyez. “The anti- $k_t$  jet clustering algorithm”. In: *JHEP* 04 (2008), p. 063. doi: [10.1088/1126-6708/2008/04/063](https://doi.org/10.1088/1126-6708/2008/04/063). arXiv: [0802.1189 \[hep-ph\]](https://arxiv.org/abs/0802.1189).
- 3412  
3413
- 3414 [15] S. Agostinelli et al. “GEANT4: A simulation toolkit”. In: *Nucl. Instrum. Meth. A* 506 (2003), pp. 250–303. doi: [10.1016/S0168-9002\(03\)01368-8](https://doi.org/10.1016/S0168-9002(03)01368-8).
- 3415  
3416  
3417  
3418  
3419
- 3420 [16] ATLAS Collaboration. “A study of the material in the ATLAS inner detector using secondary hadronic interactions”. In: *JINST* 7 (2012), P01013. doi: [10.1088/1748-0221/7/01/P01013](https://doi.org/10.1088/1748-0221/7/01/P01013). arXiv: [1110.6191 \[hep-ex\]](https://arxiv.org/abs/1110.6191). PERF-2011-08.
- 3421  
3422  
3423
- 3424 [17] ATLAS Collaboration. “Electron and photon energy calibration with the ATLAS detector using LHC Run 1 data”. In: *Eur. Phys. J. C* 74 (2014), p. 3071. doi: [10.1140/epjc/s10052-014-3071-4](https://doi.org/10.1140/epjc/s10052-014-3071-4). arXiv: [1407.5063 \[hep-ex\]](https://arxiv.org/abs/1407.5063). PERF-2013-05.
- 3425  
3426  
3427
- 3428 [18] ATLAS Collaboration. “A measurement of the calorimeter response to single hadrons and determination of the jet energy scale uncertainty using LHC Run-1  $pp$ -collision data with the ATLAS detector”. In: (2016). arXiv: [1607.08842 \[hep-ex\]](https://arxiv.org/abs/1607.08842). PERF-2015-05.
- 3429  
3430  
3431
- 3432 [19] ATLAS Collaboration. “Single hadron response measurement and calorimeter jet energy scale uncertainty with the ATLAS detector at the LHC”. In: *Eur. Phys. J. C* 73 (2013), p. 2305. doi: [10.1140/epjc/s10052-013-2305-1](https://doi.org/10.1140/epjc/s10052-013-2305-1). arXiv: [1203.1302 \[hep-ex\]](https://arxiv.org/abs/1203.1302). PERF-2011-05.
- 3433  
3434
- 3435 [20] ATLAS Collaboration. “The ATLAS Simulation Infrastructure”. In: *Eur. Phys. J. C* 70 (2010), p. 823. doi: [10.1140/epjc/s10052-010-1429-9](https://doi.org/10.1140/epjc/s10052-010-1429-9). arXiv: [1005.4568 \[hep-ex\]](https://arxiv.org/abs/1005.4568). SOFT-2010-01.
- 3436  
3437
- 3438 [21] T. Sjöstrand, S. Mrenna, and P. Skands. “A Brief Introduction to PYTHIA 8.1”. In: *Comput. Phys. Commun.* 178 (2008), pp. 852–867. doi: [10.1016/j.cpc.2008.01.036](https://doi.org/10.1016/j.cpc.2008.01.036). arXiv: [0710.3820](https://arxiv.org/abs/0710.3820).
- 3439
- 3440 [22] ATLAS Collaboration. *Summary of ATLAS Pythia 8 tunes*. ATL-PHYS-PUB-2012-003. 2012. URL: <http://cds.cern.ch/record/1474107>.
- 3441  
3442  
3443
- 3444 [23] A.D. Martin, W.J. Stirling, R.S. Thorne, and G. Watt. “Parton distributions for the LHC”. In: *Eur. Phys. J. C* 63 (2009). Figures from the [MSTW Website](#), pp. 189–285. doi: [10.1140/epjc/s10052-009-1072-5](https://doi.org/10.1140/epjc/s10052-009-1072-5). arXiv: [0901.0002](https://arxiv.org/abs/0901.0002).
- 3445  
3446
- 3447 [24] A. Sherstnev and R.S. Thorne. “Parton Distributions for LO Generators”. In: *Eur. Phys. J. C* 55 (2008), pp. 553–575. doi: [10.1140/epjc/s10052-008-0610-x](https://doi.org/10.1140/epjc/s10052-008-0610-x). arXiv: [0711.2473](https://arxiv.org/abs/0711.2473).
- 3448  
3449  
3450
- 3451 [25] A. Ribon et al. *Status of Geant4 hadronic physics for the simulation of LHC experiments at the start of LHC physics program*. CERN-LCGAPP-2010-02. 2010. URL: <http://lcgapp.cern.ch/project/docs/noteStatusHadronic2010.pdf>.

- 3451 [26] M. P. Guthrie, R. G. Alsmiller, and H. W. Bertini. "Calculation of the cap-  
 3452 ture of negative pions in light elements and comparison with experiments  
 3453 pertaining to cancer radiotherapy". In: *Nucl. Instrum. Meth.* 66 (1968), pp. 29–  
 3454 36. doi: [10.1016/0029-554X\(68\)90054-2](https://doi.org/10.1016/0029-554X(68)90054-2).
- 3455 [27] H. W. Bertini and P. Guthrie. "News item results from medium-energy  
 3456 intranuclear-cascade calculation". In: *Nucl. Instr. and Meth. A* 169 (1971),  
 3457 p. 670. doi: [10.1016/0375-9474\(71\)90710-X](https://doi.org/10.1016/0375-9474(71)90710-X).
- 3458 [28] V.A. Karmanov. "Light Front Wave Function of Relativistic Composite  
 3459 System in Explicitly Solvable Model". In: *Nucl. Phys. B* 166 (1980), p. 378.  
 3460 doi: [10.1016/0550-3213\(80\)90204-7](https://doi.org/10.1016/0550-3213(80)90204-7).
- 3461 [29] H. S. Fesefeldt. *GHEISHA program*. Pitha-85-02, Aachen. 1985.
- 3462 [30] G. Folger and J.P. Wellisch. "String parton models in Geant4". In: (2003).  
 3463 arXiv: [nucl-th/0306007](https://arxiv.org/abs/nucl-th/0306007).
- 3464 [31] N. S. Amelin et al. "Transverse flow and collectivity in ultrarelativistic  
 3465 heavy-ion collisions". In: *Phys. Rev. Lett.* 67 (1991), p. 1523. doi: [10.1103/PhysRevLett.67.1523](https://doi.org/10.1103/PhysRevLett.67.1523).
- 3467 [32] N. S. Amelin et al. "Collectivity in ultrarelativistic heavy ion collisions". In:  
 3468 *Nucl. Phys. A* 544 (1992), p. 463. doi: [10.1016/0375-9474\(92\)90598-E](https://doi.org/10.1016/0375-9474(92)90598-E).
- 3470 [33] L. V. Bravina et al. "Fluid dynamics and Quark Gluon string model - What  
 3471 we can expect for Au+Au collisions at 11.6 AGeV/c". In: *Nucl. Phys. A* 566  
 3472 (1994), p. 461. doi: [10.1016/0375-9474\(94\)90669-6](https://doi.org/10.1016/0375-9474(94)90669-6).
- 3473 [34] L. V. Bravin et al. "Scaling violation of transverse flow in heavy ion col-  
 3474 lisions at AGS energies". In: *Phys. Lett. B* 344 (1995), p. 49. doi: [10.1016/0370-2693\(94\)01560-Y](https://doi.org/10.1016/0370-2693(94)01560-Y).
- 3476 [35] B. Andersson et al. "A model for low-pT hadronic reactions with general-  
 3477 izations to hadron-nucleus and nucleus-nucleus collisions". In: *Nucl. Phys.*  
 3478 *B* 281 (1987), p. 289. doi: [10.1016/0550-3213\(87\)90257-4](https://doi.org/10.1016/0550-3213(87)90257-4).
- 3479 [36] B. Andersson, A. Tai, and B.-H. Sa. "Final state interactions in the (nuclear)  
 3480 FRITIOF string interaction scenario". In: *Z. Phys. C* 70 (1996), pp. 499–  
 3481 506. doi: [10.1007/s002880050127](https://doi.org/10.1007/s002880050127).
- 3482 [37] B. Nilsson-Almqvist and E. Stenlund. "Interactions Between Hadrons and  
 3483 Nuclei: The Lund Monte Carlo, Fritiof Version 1.6". In: *Comput. Phys. Com-*  
 3484 *mun.* 43 (1987), p. 387. doi: [10.1016/0010-4655\(87\)90056-7](https://doi.org/10.1016/0010-4655(87)90056-7).
- 3485 [38] B. Ganhuyag and V. Uzhinsky. "Modified FRITIOF code: Negative charged  
 3486 particle production in high energy nucleus nucleus interactions". In: *Czech.*  
 3487 *J. Phys.* 47 (1997), pp. 913–918. doi: [10.1023/A:1021296114786](https://doi.org/10.1023/A:1021296114786).
- 3488 [39] ATLAS Collaboration. "Topological cell clustering in the ATLAS calorime-  
 3489 ters and its performance in LHC Run 1". In: (2016). arXiv: [1603.02934](https://arxiv.org/abs/1603.02934)  
 3490 [[hep-ex](#)].
- 3491 [40] Peter Speckmayer. "Energy Measurement of Hadrons with the CERN AT-  
 3492 LAS Calorimeter". Presented on 18 Jun 2008. PhD thesis. Vienna: Vienna,  
 3493 Tech. U., 2008. URL: <http://cds.cern.ch/record/1112036>.

- 3494 [41] CMS Collaboration. “The CMS barrel calorimeter response to particle  
 3495 beams from 2 to 350 GeV/c”. In: *Eur. Phys. J. C* 60.3 (2009). doi: [10.1140/epjc/s10052-009-0959-5](https://doi.org/10.1140/epjc/s10052-009-0959-5).
- 3497 [42] J. Beringer et al. (Particle Data Group). “Review of Particle Physics”. In:  
 3498 *Chin. Phys. C* 38 (2014), p. 090001. URL: <http://pdg.lbl.gov>.
- 3499 [43] P. Adragna et al. “Measurement of Pion and Proton Response and Lon-  
 3500 gitudinal Shower Profiles up to 20 Nuclear Interaction Lengths with the  
 3501 ATLAS Tile Calorimeter”. In: *Nucl. Instrum. Meth. A* 615 (2010), pp. 158–  
 3502 181. doi: [10.1016/j.nima.2010.01.037](https://doi.org/10.1016/j.nima.2010.01.037).
- 3503 [44] ATLAS Collaboration. “Jet energy measurement and its systematic uncer-  
 3504 tainty in proton–proton collisions at  $\sqrt{s} = 7$  TeV with the ATLAS detec-  
 3505 tor”. In: *Eur. Phys. J. C* 75 (2015), p. 17. doi: [10.1140/epjc/s10052-014-3190-y](https://doi.org/10.1140/epjc/s10052-014-3190-y). arXiv: [1406.0076 \[hep-ex\]](https://arxiv.org/abs/1406.0076). PERF-2012-01.
- 3507 [45] Hung-Liang Lai, Marco Guzzi, Joey Huston, Zhao Li, Pavel M. Nadolsky,  
 3508 et al. “New parton distributions for collider physics”. In: *Phys. Rev. D* 82  
 3509 (2010), p. 074024. doi: [10.1103/PhysRevD.82.074024](https://doi.org/10.1103/PhysRevD.82.074024). arXiv: [1007.2241 \[hep-ph\]](https://arxiv.org/abs/1007.2241).
- 3511 [46] E. Abat et al. “Study of energy response and resolution of the ATLAS barrel  
 3512 calorimeter to hadrons of energies from 20 to 350 GeV”. In: *Nucl. Instrum.*  
 3513 *Meth. A* 621.1-3 (2010), pp. 134 – 150. doi: <http://dx.doi.org/10.1016/j.nima.2010.04.054>.
- 3515 [47] ATLAS Collaboration. “Jet energy measurement with the ATLAS detector  
 3516 in proton–proton collisions at  $\sqrt{s} = 7$  TeV”. In: *Eur. Phys. J. C* 73 (2013),  
 3517 p. 2304. doi: [10.1140/epjc/s10052-013-2304-2](https://doi.org/10.1140/epjc/s10052-013-2304-2). arXiv: [1112.6426 \[hep-ex\]](https://arxiv.org/abs/1112.6426). PERF-2011-03.
- 3519 [48] Nausheen R. Shah and Carlos E. M. Wagner. “Gravitons and dark matter in  
 3520 universal extra dimensions”. In: *Phys. Rev. D* 74 (2006), p. 104008. doi: [10.1103/PhysRevD.74.104008](https://doi.org/10.1103/PhysRevD.74.104008). arXiv: [hep-ph/0608140 \[hep-ph\]](https://arxiv.org/abs/hep-ph/0608140).
- 3522 [49] Jonathan L. Feng, Arvind Rajaraman, and Fumihiro Takayama. “Graviton  
 3523 cosmology in universal extra dimensions”. In: *Phys. Rev. D* 68 (2003), p. 085018.  
 3524 doi: [10.1103/PhysRevD.68.085018](https://doi.org/10.1103/PhysRevD.68.085018). arXiv: [hep-ph/0307375 \[hep-ph\]](https://arxiv.org/abs/hep-ph/0307375).
- 3526 [50] Paul H. Frampton and Pham Quang Hung. “Long-lived quarks?” In: *Phys.*  
 3527 *Rev. D* 58 (5 1998), p. 057704. doi: [10.1103/PhysRevD.58.057704](https://doi.org/10.1103/PhysRevD.58.057704).  
 3528 URL: <http://link.aps.org/doi/10.1103/PhysRevD.58.057704>.
- 3530 [51] C. Friberg, E. Norrbin, and T. Sjostrand. “QCD aspects of leptoquark pro-  
 3531 duction at HERA”. In: *Phys. Lett. B* 403 (1997), pp. 329–334. doi: [10.1016/S0370-2693\(97\)00543-1](https://doi.org/10.1016/S0370-2693(97)00543-1). arXiv: [hep-ph/9704214 \[hep-ph\]](https://arxiv.org/abs/hep-ph/9704214).
- 3533 [52] Herbert K. Dreiner. “An introduction to explicit R-parity violation”. In:  
 3534 (1997). arXiv: [hep-ph/9707435](https://arxiv.org/abs/hep-ph/9707435).

- 3535 [53] Edmond L. Berger and Zack Sullivan. "Lower limits on R-parity-violating  
 3536 couplings in supersymmetry". In: *Phys. Rev. Lett.* 92 (2004), p. 201801. doi:  
 3537 [10.1103/PhysRevLett.92.201801](https://doi.org/10.1103/PhysRevLett.92.201801). arXiv: [hep-ph/0310001](https://arxiv.org/abs/hep-ph/0310001).
- 3538 [54] R. Barbieri, C. Berat, M. Besancon, M. Chemtob, A. Deandrea, et al. "R-  
 3539 parity violating supersymmetry". In: *Phys. Rept.* 420 (2005), p. 1. doi: [10.1016/j.physrep.2005.08.006](https://doi.org/10.1016/j.physrep.2005.08.006). arXiv: [hep-ph/0406039](https://arxiv.org/abs/hep-ph/0406039).
- 3541 [55] M. Fairbairn et al. "Stable massive particles at colliders". In: *Phys. Rept.* 438  
 3542 (2007), p. 1. doi: [10.1016/j.physrep.2006.10.002](https://doi.org/10.1016/j.physrep.2006.10.002). arXiv: [hep-ph/0611040](https://arxiv.org/abs/hep-ph/0611040).
- 3544 [56] Christopher F. Kolda. "Gauge-mediated supersymmetry breaking: Intro-  
 3545 duction, review and update". In: *Nucl. Phys. Proc. Suppl.* 62 (1998), p. 266.  
 3546 doi: [10.1016/S0920-5632\(97\)00667-1](https://doi.org/10.1016/S0920-5632(97)00667-1). arXiv: [hep-ph/9707450](https://arxiv.org/abs/hep-ph/9707450).
- 3547 [57] Howard Baer, Kingman Cheung, and John F. Gunion. "A Heavy gluino as  
 3548 the lightest supersymmetric particle". In: *Phys. Rev. D* 59 (1999), p. 075002.  
 3549 doi: [10.1103/PhysRevD.59.075002](https://doi.org/10.1103/PhysRevD.59.075002). arXiv: [hep-ph/9806361](https://arxiv.org/abs/hep-ph/9806361).
- 3550 [58] S. James Gates Jr. and Oleg Lebedev. "Searching for supersymmetry in  
 3551 hadrons". In: *Phys. Lett. B* 477 (2000), p. 216. doi: [10.1016/S0370-2693\(00\)00172-6](https://doi.org/10.1016/S0370-2693(00)00172-6). arXiv: [hep-ph/9912362](https://arxiv.org/abs/hep-ph/9912362).
- 3553 [59] G. F. Giudice and A. Romanino. "Split supersymmetry". In: *Nucl. Phys. B*  
 3554 699 (2004), p. 65. doi: [10.1016/j.nuclphysb.2004.11.048](https://doi.org/10.1016/j.nuclphysb.2004.11.048). arXiv:  
 3555 [hep-ph/0406088](https://arxiv.org/abs/hep-ph/0406088).
- 3556 [60] N. Arkani-Hamed, S. Dimopoulos, G. F. Giudice, and A. Romanino. "As-  
 3557 pects of split supersymmetry". In: *Nucl. Phys. B* 709 (2005), p. 3. doi: [10.1016/j.nuclphysb.2004.12.026](https://doi.org/10.1016/j.nuclphysb.2004.12.026). arXiv: [hep-ph/0409232](https://arxiv.org/abs/hep-ph/0409232).
- 3559 [61] Glennys R. Farrar and Pierre Fayet. "Phenomenology of the Production,  
 3560 Decay, and Detection of New Hadronic States Associated with Supersym-  
 3561 metry". In: *Phys. Lett.* B76 (1978), pp. 575–579. doi: [10.1016/0370-2693\(78\)90858-4](https://doi.org/10.1016/0370-2693(78)90858-4).
- 3563 [62] A. C. Kraan, J. B. Hansen, and P. Nevski. "Discovery potential of R-hadrons  
 3564 with the ATLAS detector". In: *Eur. Phys. J.* C49 (2007), pp. 623–640. doi:  
 3565 [10.1140/epjc/s10052-006-0162-x](https://doi.org/10.1140/epjc/s10052-006-0162-x). arXiv: [hep-ex/0511014](https://arxiv.org/abs/hep-ex/0511014)  
 3566 [[hep-ex](#)].
- 3567 [63] Rasmus Mckeprang and David Milstead. "An Updated Description of  
 3568 Heavy-Hadron Interactions in GEANT-4". In: *Eur. Phys. J.* C66 (2010), pp. 493–  
 3569 501. doi: [10.1140/epjc/s10052-010-1262-1](https://doi.org/10.1140/epjc/s10052-010-1262-1). arXiv: [0908.1868](https://arxiv.org/abs/0908.1868)  
 3570 [[hep-ph](#)].
- 3571 [64] ATLAS Collaboration. "Search for massive, long-lived particles using mul-  
 3572 titrack displaced vertices or displaced lepton pairs in  $pp$  collisions at  $\sqrt{s} =$   
 3573 8 TeV with the ATLAS detector". In: *Phys. Rev. D* 92 (2015), p. 072004.  
 3574 doi: [10.1103/PhysRevD.92.072004](https://doi.org/10.1103/PhysRevD.92.072004). arXiv: [1504.05162 \[hep-ex\]](https://arxiv.org/abs/1504.05162).  
 3575 SUSY-2014-02.

- 3576 [65] ATLAS Collaboration. “Search for charginos nearly mass degenerate with  
 3577 the lightest neutralino based on a disappearing-track signature in  $pp$  col-  
 3578 lisions at  $\sqrt{s} = 8$  TeV with the ATLAS detector”. In: *Phys. Rev. D* 88 (2013),  
 3579 p. 112006. doi: [10.1103/PhysRevD.88.112006](https://doi.org/10.1103/PhysRevD.88.112006). arXiv: [1310.3675](https://arxiv.org/abs/1310.3675)  
 3580 [[hep-ex](#)]. SUSY-2013-01.
- 3581 [66] ATLAS Collaboration. “Searches for heavy long-lived sleptons and R-Hadrons  
 3582 with the ATLAS detector in  $pp$  collisions at  $\sqrt{s} = 7$  TeV”. In: *Phys. Lett. B*  
 3583 720 (2013), p. 277. doi: [10.1016/j.physletb.2013.02.015](https://doi.org/10.1016/j.physletb.2013.02.015). arXiv:  
 3584 [1211.1597](https://arxiv.org/abs/1211.1597) [[hep-ex](#)]. SUSY-2012-01.
- 3585 [67] ATLAS Collaboration. “Searches for heavy long-lived charged particles  
 3586 with the ATLAS detector in proton–proton collisions at  $\sqrt{s} = 8$  TeV”. In:  
 3587 *JHEP* 01 (2015), p. 068. doi: [10.1007/JHEP01\(2015\)068](https://doi.org/10.1007/JHEP01(2015)068). arXiv:  
 3588 [1411.6795](https://arxiv.org/abs/1411.6795) [[hep-ex](#)]. SUSY-2013-22.
- 3589 [68] ATLAS Collaboration. “Search for metastable heavy charged particles with  
 3590 large ionisation energy loss in  $pp$  collisions at  $\sqrt{s} = 8$  TeV using the AT-  
 3591 LAS experiment”. In: *Eur. Phys. J. C* 75 (2015), p. 407. doi: [10.1140/epjc/s10052-015-3609-0](https://doi.org/10.1140/epjc/s10052-015-3609-0). arXiv: [1506.05332](https://arxiv.org/abs/1506.05332) [[hep-ex](#)]. SUSY-  
 3593 2014-09.
- 3594 [69] ATLAS Collaboration. “Search for heavy long-lived charged  $R$ -hadrons  
 3595 with the ATLAS detector in  $3.2 \text{ fb}^{-1}$  of proton–proton collision data at  
 3596  $\sqrt{s} = 13$  TeV”. In: *Phys. Lett. B* 760 (2016), pp. 647–665. doi: [10.1016/j.physletb.2016.07.042](https://doi.org/10.1016/j.physletb.2016.07.042). arXiv: [1606.05129](https://arxiv.org/abs/1606.05129) [[hep-ex](#)].
- 3598 [70] Torbjorn Sjöstrand, Stephen Mrenna, and Peter Skands. “PYTHIA 6.4 Physics  
 3599 and Manual”. In: *JHEP* 0605 (2006), p. 026. doi: [10.1088/1126-6708/2006/05/026](https://doi.org/10.1088/1126-6708/2006/05/026). arXiv: [hep-ph/0603175](https://arxiv.org/abs/hep-ph/0603175).
- 3601 [71] *Further ATLAS tunes of PYTHIA6 and Pythia 8*. Tech. rep. ATL-PHYS-PUB-  
 3602 2011-014. Geneva: CERN, 2011. url: <https://cds.cern.ch/record/1400677>.
- 3604 [72] Aafke Christine Kraan. “Interactions of heavy stable hadronizing parti-  
 3605 cles”. In: *Eur. Phys. J. C* 37 (2004), pp. 91–104. doi: [10.1140/epjc/s2004-01946-6](https://doi.org/10.1140/epjc/s2004-01946-6). arXiv: [hep-ex/0404001](https://arxiv.org/abs/hep-ex/0404001) [[hep-ex](#)].
- 3607 [73] M. Fairbairn et al. “Stable massive particles at colliders”. In: *Phys. Rept.* 438  
 3608 (2007), p. 1. doi: [10.1016/j.physrep.2006.10.002](https://doi.org/10.1016/j.physrep.2006.10.002). arXiv: [hep-ph/0611040](https://arxiv.org/abs/hep-ph/0611040).
- 3610 [74] W. Beenakker, R. Hopker, M. Spira, and P. M. Zerwas. “Squark and gluino  
 3611 production at hadron colliders”. In: *Nucl. Phys. B* 492 (1997), p. 51. doi:  
 3612 [10.1016/S0550-3213\(97\)00084-9](https://doi.org/10.1016/S0550-3213(97)00084-9). arXiv: [hep-ph/9610490](https://arxiv.org/abs/hep-ph/9610490).
- 3613 [75] A. Kulesza and L. Motyka. “Threshold resummation for squark-antisquark  
 3614 and gluino-pair production at the LHC”. In: *Phys. Rev. Lett.* 102 (2009),  
 3615 p. 111802. doi: [10.1103/PhysRevLett.102.111802](https://doi.org/10.1103/PhysRevLett.102.111802). arXiv: [0807.2405](https://arxiv.org/abs/0807.2405) [[hep-ph](#)].

- 3617 [76] A. Kulesza and L. Motyka. “Soft gluon resummation for the production  
 3618 of gluino-gluino and squark-antisquark pairs at the LHC”. In: *Phys. Rev.*  
 3619 *D* 80 (2009), p. 095004. doi: [10.1103/PhysRevD.80.095004](https://doi.org/10.1103/PhysRevD.80.095004). arXiv:  
 3620 [0905.4749 \[hep-ph\]](https://arxiv.org/abs/0905.4749).
- 3621 [77] Wim Beenakker, Silja Brensing, Michael Kramer, Anna Kulesza, Eric Lae-  
 3622 nen, et al. “Soft-gluon resummation for squark and gluino hadroproduc-  
 3623 tion”. In: *JHEP* 0912 (2009), p. 041. doi: [10.1088/1126-6708/2009/12/041](https://doi.org/10.1088/1126-6708/2009/12/041). arXiv: [0909.4418 \[hep-ph\]](https://arxiv.org/abs/0909.4418).
- 3625 [78] W. Beenakker, S. Brensing, M.n Kramer, A. Kulesza, E. Laenen, et al. “Squark  
 3626 and Gluino Hadroproduction”. In: *Int. J. Mod. Phys. A* 26 (2011), p. 2637.  
 3627 doi: [10.1142/S0217751X11053560](https://doi.org/10.1142/S0217751X11053560). arXiv: [1105.1110 \[hep-ph\]](https://arxiv.org/abs/1105.1110).
- 3628 [79] Michael Krämer et al. *Supersymmetry production cross sections in pp collisions*  
 3629 at  $\sqrt{s} = 7 \text{ TeV}$ . 2012. arXiv: [1206.2892 \[hep-ph\]](https://arxiv.org/abs/1206.2892).
- 3630 [80] Rasmus Mackeprang and Andrea Rizzi. “Interactions of Coloured Heavy  
 3631 Stable Particles in Matter”. In: *Eur. Phys. J.* C50 (2007), pp. 353–362. doi:  
 3632 [10.1140/epjc/s10052-007-0252-4](https://doi.org/10.1140/epjc/s10052-007-0252-4). arXiv: [hep-ph/0612161](https://arxiv.org/abs/hep-ph/0612161)  
 3633 [hep-ph].
- 3634 [81] Rasmus Mackeprang and David Milstead. “An Updated Description of  
 3635 Heavy-Hadron Interactions in GEANT-4”. In: *Eur. Phys. J.* C66 (2010), pp. 493–  
 3636 501. doi: [10.1140/epjc/s10052-010-1262-1](https://doi.org/10.1140/epjc/s10052-010-1262-1). arXiv: [0908.1868](https://arxiv.org/abs/0908.1868)  
 3637 [hep-ph].
- 3638 [82] J. Alwall, R. Frederix, S. Frixione, V. Hirschi, F. Maltoni, O. Mattelaer, H. S.  
 3639 Shao, T. Stelzer, P. Torrielli, and M. Zaro. “The automated computation of  
 3640 tree-level and next-to-leading order differential cross sections, and their  
 3641 matching to parton shower simulations”. In: *JHEP* 07 (2014), p. 079. doi:  
 3642 [10.1007/JHEP07\(2014\)079](https://doi.org/10.1007/JHEP07(2014)079). arXiv: [1405.0301 \[hep-ph\]](https://arxiv.org/abs/1405.0301).
- 3643 [83] “dE/dx measurement in the ATLAS Pixel Detector and its use for particle  
 3644 identification”. In: (2011).
- 3645 [84] ATLAS Collaboration. “The ATLAS Simulation Infrastructure”. In: *Eur.*  
 3646 *Phys. J.* C70 (2010), pp. 823–874. doi: [10.1140/epjc/s10052-010-1429-9](https://doi.org/10.1140/epjc/s10052-010-1429-9). arXiv: [1005.4568 \[physics.ins-det\]](https://arxiv.org/abs/1005.4568).
- 3648 [85] Alexander L. Read. “Presentation of search results: The CL(s) technique”.  
 3649 In: *J. Phys. G* 28 (2002). [,11(2002)], pp. 2693–2704. doi: [10.1088/0954-3899/28/10/313](https://doi.org/10.1088/0954-3899/28/10/313).



3651 DECLARATION

---

3652 Put your declaration here.

3653 *Berkeley, CA, September 2016*

3654

---

Bradley Axen



3655

3656 COLOPHON

3657

Not sure that this is necessary.